TOWARDS SIMULTANEOUS SINGLE EMISSION MICROSCOPY AND MAGNETIC RESONANCE IMAGING

BY

LIANG CAI

DISSERTATION

Submitted in partial fulfillment of the requirements
for the degree of Doctor of Philosophy in Nuclear, Plasma and Radiological Engineering
in the Graduate College of the
University of Illinois at Urbana-Champaign, 2013

Urbana, Illinois

Doctoral Committee:

Associate Professor Ling-Jian Meng, Chair
Professor James F. Stubbins
Assistant Professor Clair J. Sullivan
Associate Professor Brad Sutton

ABSTRACT

In recent years, the combined nuclear imaging and magnetic resonance imaging (MRI) has drawn extensive research effort. They can provide simultaneously acquired anatomical and functional information inside the human/small animal body in vivo. In this dissertation, the development of an ultrahigh resolution MR-compatible SPECT (Single Photon Emission Computed Tomography) system that can be operated inside a pre-existing clinical MR scanner for simultaneous dual-modality imaging of small animals will be discussed. This system is constructed with 40 small-pixel CdTe detector modules assembled in a fully stationary ring SPECT geometry. Series of experiments have demonstrated that this system is capable of providing an imaging resolution of <500μm, when operated inside MR scanners.

The ultrahigh resolution MR-compatible SPECT system is built around a small-pixel CdTe detector module that we recently developed. Each module consists of CdTe detectors having an overall size of 2.2 cm × 1.1 cm, divided into 64 × 32 pixels of 350 μm in size. A novel hybrid pixel-waveform (HPWF) readout system is also designed to alleviate several challenges for using small-pixel CdTe detectors in ultrahigh-resolution SPECT imaging applications. The HPWF system utilizes a modified version of a 2048-channel 2-D CMOS ASIC to readout the anode pixel, and a digitizing circuitry to sample the signal waveform induced on the cathode. The cathode waveform acquired with the HPWF circuitry offers excellent spatial resolution, energy resolution and depth of interaction (DOI) information, even with the presence of excessive charge-sharing/charge-loss between the small anode pixels. The HPWF CdTe detector is designed and constructed with a minimum amount of ferromagnetic materials, to ensure the MR-compatibility. To achieve sub-500μm imaging resolution, two special designed SPECT apertures have been constructed with different pinhole sizes of 300μm and 500μm respectively. It has 40 pinhole inserts that are made of cast platinum (90%)-iridium (10%) alloy, which provides the maximum stopping power and are compatible with MR scanners.

The SPECT system is installed on a non-metal gantry constructed with 3-D printing using nylon powder material. This compact system can work as a “low-cost” desktop ultrahigh resolution SPECT system. It can also be directly operated inside an MR scanner. Accurate system

geometrical calibration and corresponding image reconstruction methods for the MRC-SPECT system is developed. In order to account for the magnetic field induced distortion in the SPECT image, a comprehensive charge collection model inside strong magnetic field is adopted to produce high resolution SPECT image inside MR scanner.

Keywords: *MR-SPECT, semiconductor detector, CdTe, System development*

To my family

ACKNOWLEDGEMENTS

This dissertation would not be finished without the continuous love, support and encouragement from my beautiful wife, Wenjiao Zhao. I would like to express my sincere appreciation and deepest love to her.

I would like to thank my advisor, Prof. Ling-Jian Meng, for his generous support and extensive advices of this research project. Besides the theoretical and experimental skills, I also learned that scientific thinking and positive attitude on the research projects were of more importance than simply task implementation. I would also like to thank Prof. James F. Stubbins, Prof. Clair J. Sullivan and Prof. Brad Sutton to serve as my committee member.

Thanks also to my previous and current colleagues, Dr. Geng Fu, Dr. Nan Li, Dr. Jiawei Tan, Xiaochun Lai, Zengming Shen, Jianchuan Zhang, Jinghong Wang, Chen Duan, Andrew Groll, and Jon George, for their contributions and help on this project. I also appreciate the support and guidance from the collaborators at the University of Chicago, especially Prof. Chin-Tu Chen and Prof. Fukun Tang. Buxin Chen and Hsiu-min Tsai contribute a lot on the experiments in Chicago.

Last but not the least, the staff in our department helped me a lot during my PhD study in Illinois. I would sincerely express my appreciation to Gail Krueger, Becky Meline, and Idell Dollison.

Table of Contents

CHAPTER 1
Introduction

1.1 Basics of Emission Tomography

Emission tomography is a branch of medical imaging that includes two main techniques - single photon emission computed tomography (SPECT) and positron emission tomography (PET). Emission tomography uses radioactive materials to image properties inside the body or small animal's physiology. For example, emission tomography could provide the information of radioactivity concentration inside the tissue and to image the molecules quantifying the kinetic process when the drugs interact with molecules inside the body [1, 2]. Many different radiotracers are developed for specific functions and targets to label the molecules, and the imaging technologies are used to detect the signal originated from those molecules with their interaction observed *in vivo*.

PET and SPECT are distinguished mainly by the type of radioisotope incorporated in the tracer. SPECT imaging uses radiopharmaceuticals labeled with single emission emitter, a radioisotope that emits a single gamma-ray photon in each radioactive decay. In PET, radionuclide decays by positron emission resulting in two simultaneous annihilation photons emitted back-to-back. The distinction between the numbers of emitted photons dictates the type of hardware used to detect and localize the event. Generally, a collimator is used in SPECT imaging in order to form an image by selecting the rays traveling in specific direction. Gamma-rays not coming into the collimator are blocked. Compared to SPECT, PET systems detect two back-to-back annihilation photons to confine the original positron decay event onto a so-called line of response (LOR) across the object. Therefore, PET systems require no physical collimator and generally offers a higher sensitivity than SPECT.

Despite the sensitivity limitation, SPECT can potentially provide better spatial resolution than PET. In PET, the spatial resolution is limited by the positron range, which represents the travel range before positron annihilates with an electron. In addition to positron range,

the variation in the positron momentum results in an angular uncertainty in the direction of the back-to-back 511keV photons. In comparison, SPECT does not have these intrinsic spatial resolution limiting factors, and is theoretically capable of delivering higher spatial resolution than PET. The tradeoff is the high spatial resolution versus relatively low sensitivity. A more detailed comparison between PET and SPECT is discussed in section 1.2.

1.2 The Comparison of PET and SPECT

As we mentioned in section 1.1, Positron Emission Tomography (PET) and Single Photon Emission Computed Tomography (SPECT) are two of the most popular modalities used for molecular imaging in current days. There are several key differences between these PET and SPECT. The comparison between these two modalities in terms of sensitivity, spatial resolution and temporal resolution will be addressed in this section [3].

Sensitivity comparison

One of the key difference between SPECT and PET lies in the sensitivity. PET imaging exhibits a much higher sensitivity (by approximately two or three orders of magnitude) than SPECT, which means PET has much higher ability to detect and record the photons emitted from specific radioactive isotopes. It is because, in Single Photon Emission Computed Tomography (SPECT), physical collimators are used to confine the incoming photons with a small angular range (otherwise the angle of incidence information will be lost). Typically the collimator will exhibit low geometry efficiency, say, at the level of 0.01%. But on the other hand, SPECT provides the possibility to widen the observation time window due the longer half-life time of the single photon emitter. This allows researchers to track the biological processes *in vivo* hours or days after the tracer injection.

On the contrary, PET imaging owns much higher sensitivity due to the nature of positron annihilation in which two annihilation photons are emitted from the same event back-to-back. The photon pairs can be collected in coincidence and this scheme works like electronic collimator instead of physical collimator, which helps to provide much higher geometrical sensitivity in the order of ~1%. The tremendously increased sensitivity in PET

has several important advantages listed below.

- *Improved image quality*

Because of the nature of the radioactive decay (Poisson random), noise is an inherent component in nuclear medicine. The percentage of noise along with a projection with *m* detected events is:

$$\%noise \sim \frac{\sigma}{m} = \frac{1}{\sqrt{m}}$$

Where σ is the standard derivation. Therefore, the increased sensitivity (increased *m*) will lead to improved signal-to-noise ratio (SNR).

- *Capability of shorter scan time*

This is also beneficial from the improved SNR. Within higher sensitivity, the shorted data acquisition time can have the same signal to noise level as longer data acquisition time with lower sensitivity. Especially in PET applications, the half-life of radioactive isotopes is relatively short. The table 1.1 below lists the half-life of four isotopes popularly used for PET imaging.

Isotope	^{18}F	^{11}C	^{13}N	^{15}O
Half-life	109.7 min	20.4 min	9.96 min	2.07 min

Table 1.1 PET isotopes half-life examples

- *Multiple field-of-view scanning*

Due to the capability of short time scan, it is possible to do multiple field-of-view scanning of a patient (or other object) in an imaging study. This is particularly useful for system with a smaller field-of-view than targeted objects. It is also a very useful and important consideration in clinical oncology. Actually, in the MRC-SPECT (MR Compatible SPECT) system which will be discussed in this dissertation, the multiple scanning scheme is used to scan object with the size larger than the system field of view. The stationary SPECT system with relatively high sensitivity makes the multiple scanning scheme possible.

- *Improved temporal resolution*

The improved temporal resolution mainly comes from the dynamic imaging study. With higher sensitivity, shorter scan with fewer number of frames might be able to deliver the same information as that in longer scan with lower sensitivity. This will help to get biological process information with higher temporal resolution.

Spatial resolution comparison

The spatial resolution of SPECT and PET are related to a number of different factors. In SPECT, the spatial resolution is limited to the technology of collimator design and the detector's intrinsic resolution. In PET, besides the detector's intrinsic spatial resolution limitation, there are two physics related factors which affect the resolution, namely positron range and the photon non-collinearity.

- *Pinhole SPECT*

Pinhole SPECT introduces dramatically increased image resolution to sub-millimeter scale. This kind of spatial resolution is very attractive in small animal or molecular imaging. However, the drawback of the pinhole SPECT system is the low geometry sensitivity. To overcome this, the concept of multiple pinhole SPECT is proposed and implemented. Among different multiple pinhole SPECT system, the innovative stationary SPECT scheme has several advantages of others. U-SPECT [4-5] is one of stationary SPECT systems which demonstrates extraordinary spatial resolution in various small animal applications. This type of system generally has a large number of pinholes, which helps to increase the sensitivity. In addition, the geometrical calibration of stationary SPECT can be more accurate than system with rotations. Some rotational SPECT systems have systematic error with the rotation process and this error is not easy to be compensated [6]. Although the error might be very small, it will set a noticeable limitation on high resolution system. In summary, the stationary multi-pinhole SPECT system provides a combination of ultrahigh spatial resolution and relatively high geometry sensitivity.

- *Effects degrade PET spatial resolution*

In PET imaging, besides the affect from detector itself (the scintillator width, for example), there are two other factors which degrade the spatial resolution: the positron

range and the photon non-collinearity.

The positron range represents the average distance the emitter positrons travels in the surrounding materials before they reach the thermal energies to be annihilated. Different positron emitter isotopes have different positron ranges, mainly due to distinct energy distribution of different isotopes. Generally, the positron range is treated as purely resolution limiting factor. But there do have two methods which can be applied to reduce the positron range.

One is a hardware method, which implies the effects of magnetic field. Researchers have verified the possibility of improving PET resolution by applying strong magnetic field [7-10]. This phenomenon is most significant in the case of strong magnetic field (typically >5T) and high energy positron emitter isotopes (eg, ^{68}Ga, ^{82}Rb). This is one of the advantages of designing PET/MR system, although there are more reasons of the extensive development of simultaneous PET/MR system. However, when using low energy positron emitters such as ^{18}F and ^{11}C, the magnetic field effect on the positron range is small, based on which the imaging resolution improvement on the human PET will be very limited. It is only helpful in the small animal PET application since the ring diameter is much smaller than that of human PET.

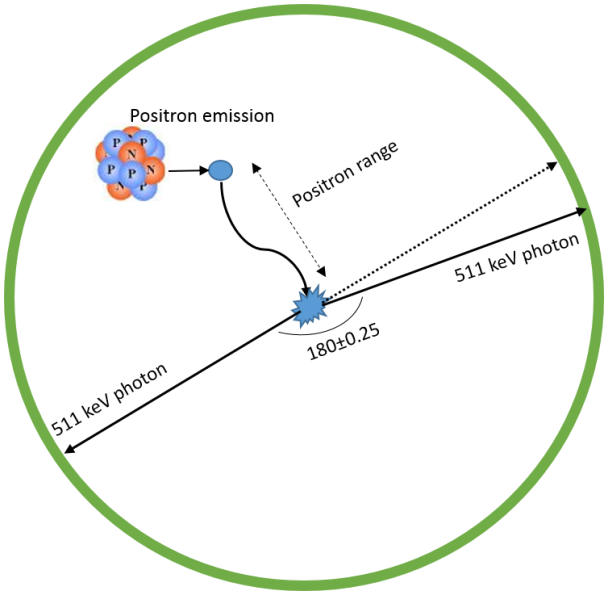

Fig. 1.1. Description about the positron range and the back to back photon non-collineartity

The other one is a software method-modelling the positron range into the reconstruction step. While with the statistical reconstruction algorithm, although it is not possible to tell the exact positron range for every individual event, it is possible to incorporate the distribution of the positron range into the system matrix, which helps to improve the reconstructed image quality. [11-14]

Besides positron range, the photon non-collinearity is another intrinsic physics factor degrading the PET spatial resolution shown as Fig. 1.1 [15-20]. The angle between the trajectories of the two annihilated photons may have a variation from 180^0 because of the non-zero net momentum of the positron and annihilated electron (due to the conservation of the momentum). Typically, the derivation is around 0.25^o FWHM, which leads to an image blurring depends on the PET scanner ring diameter *D* or the distance between the coincidence detection detectors. The image resolution degrade can be calculated as:

$$FWHM = \frac{0.25}{180} * \pi * \frac{D}{2} = 0.0022D$$

For a human PET, the diameter of the ring is typically designed to be about 70-80cm, which is a comfortable size to fit human body. The degraded spatial resolution will be around 1.5mm due to the non-collinearity. This blurring will be reduced a lot in small animal scanners because of smaller ring diameter.

Temporal resolution comparison

Dynamic imaging in nuclear medicine is becoming a very attractive topic because of its capability to track the changes of the bio-distribution of the radiopharmaceuticals inside the body. This can potentially provide important information about the underlying physiological processes within the human body or small animal. This dynamic imaging process comes with the concept of the so called temporal resolution, which means how frequently of a period of time the imaging equipment can capture and record the useful images of the target object. It is more complicated to precisely define the temporal resolution than spatial resolution, since the definition of 'captured useful image' depends on quantitative calculation which is not very straightforward. In general, the temporal resolution is related to the system sensitivity. So typically PET performs better than SPECT in the sense of dynamic imaging. After acquiring data associated with temporal

information, a 4-D reconstruction method is typically used to reconstruct the image with temporal information.

1.3 The Uniqueness of SPECT and Its Current State-of-the-art

Although there is tremendous research effort spent on the development of PET currently, SPECT does have several unique qualities, especially in terms of ultrahigh resolution imaging capability.

First, SPECT is among the most sensitive imaging technologies which are capable to measure small concentration of bimolecular with sub-millimeter level spatial resolution. With the rapid development of high performance gamma-ray photon detectors, tremendous effort has been made to push it to hundred-micron level while tiny concentration of radio-labeled molecule can offer sufficient signal-to-noise ratio (SNR).

Second, based on relatively straightforward labeling, a variety of single photon emitters with long half-lives, such as Tc-99 (6.02 hours), I-123(13.2 hours), In-111(2.8 days), and I-125(59 days), make SPECT suitable for imaging a wide range of endogenous molecules, such as peptides, antibodies, hormones and so on. The endogenous molecules have relatively large size, so a relatively long time is required for slow diffusion into tissue and clearance from blood. Thus long half-life isotopes are preferred in these applications. In addition, it is relatively easy to use simple electrophilic iodination without the need of highly specialized radiochemistry infrastructure and expertise [21]. On the contrary, the specific activity of positron emitters, such as C-11 and F-18, are fundamentally limited by their complex synthetic chemistry and relatively short half-life, and an expensive on-site cyclotron/radiochemistry production facility is also a great burden while using PET tracers.

Third, long-lived single photon emitters also provide the capabilities of measuring relatively slow kinetic processes. Many biological processes, such as cell division and neutrophils accumulation, need a long observational window after radiopharmaceutical administration to achieve acceptable contrast. For example, due to low dissociation rates some receptor ligands require a long time delay from the administration to the equilibrium state for imaging studies [22]. Based on the availability of longer-lived radionuclides the

observational time window of SPECT imaging can be extended to hours or even days while maintaining reasonable detection sensitivity.

Last but not the least, SPECT imaging has the capability to probe two or more molecular pathways simultaneously [23-28]. A variety of radiotracers has been extensively developed for probing various molecular pathways, such as blood flow, metabolism, and protein binding. Although it is common to measure one of these parameters at a time, some complex biological processes, which are related to several molecular pathways in the body, are under active investigations. Thus it is crucial to resolve the temporal relationship among these molecular pathways. Multiple molecules probes labeled by single-photon emitters at different energies can be used in this application.

Most of the recent efforts on SPECT instrumentations could fall into the following three categories. First, a tremendous amount of effort has been devoted to improving the spatial resolution of SPECT systems, especially for imaging small lab animals. This improvement is mainly coming from the use of gamma-ray sensors with an excellent intrinsic spatial resolution and the use of focusing geometries that have relatively large magnification ratios. Second, many research teams have been exploring various aperture designs that improve raw sensitivity by introducing a controlled amount of multiplexing in projection data. Third, several recent efforts started to target at the so-called adaptive SPECT imaging [29]. In this approach, the SPECT hardware can be modified adaptively in real time, to offer an optimal efficiency for collecting useful imaging information regarding the particular object being studied.

Although SPECT originally is developed for human imaging, it is getting popularity in small animal imaging, where pinhole collimation is the most common method used to achieve high spatial resolution. For small animal SPECT system design, one of the major challenges is the size of the small animal. For example, the average weight of lab mice is between 20-30g, and the size is several orders of magnitude smaller than a human. Also the mouse brain is around 1cm in diameter, which is an order of magnitude smaller than human brain. Therefore, it is difficult to use current clinical SPECT instruments developed for human body in small animal imaging. The gamma-ray photon detection systems for

small animal SPECT imaging need to be specifically designed for improving image quality with high spatial resolution [30].

1.4 Advantages of Semiconductor CdTe/CZT Detectors for Medical Imaging

In nuclear medical imaging application, the spatial (and temporal) information of gamma-ray interactions with the detecting medium need to properly recorded to generate proper projections. Generally, the desired characteristics of the detecting medium should have high stopping power for the incoming gamma rays, high intrinsic spatial resolution, high energy resolution and high detection efficiency. Materials with high atomic number and high density typically are needed to get good stopping power and reasonable photopeak efficiency. Based on different detecting materials, the gamma ray detectors can be divided to two main categories: scintillator detectors and semiconductor detectors.

1.4.1 Conventional Scintillator Detectors for Gamma Ray Detection

A scintillator is a material that converts X-rays, gamma-rays and energetic particles into visible photons. In scintillators, the incoming gamma ray (or X-ray, etc.) does not create direct ionization or excitation. The photon interaction with the material transfers whole or a part of the energy to an electron. The incoming photon energy is typically higher than that of the electron binding energy, and the scintillator material is ionized by three main types of interaction mechanism: photoelectric absorption, Compton scattering, and pair production. For the energy range up to several hundred keV, the photoelectric absorption is the predominant interaction mechanism. The cross section is strongly depend on the atomic number of the material. The resultant secondary electron is ejected and will cause ionization along its path. The number of scintillation photons generated is typically proportional to the energy deposited in the crystal.

After the generation of scintillation photons, another step is needed to convert the visible photons to electrical signals. The scintillation photon detector, such as photomultiplier (PMT) or photodiode is coupled to the scintillator to do the conversion. A photocathode is used to convert the photons to photoelectrons. The quantum efficiency (QE) is typically used to identify the ratio that how much photons can be converted to photoelectrons.

$$QE = \frac{number\ of\ photoelectrons}{number\ of\ incident\ photons}$$

Scintillator detectors have been widely used for gamma ray detection in the past decades and are still very popular now. One of the advantages of inorganic scintillators is the size of the crystals can be grown. It provides sufficient detection efficiency for the gamma ray detection applications. With the development of the technology, pixelated and micro-columnar scintillators are also under extensive investigation for high resolution imaging, especially in SPECT application.

One of the drawbacks of the scintillators is the low energy resolution. It is limited by the statistics of the scintillation photons and resulting photoelectrons. Relatively high energy is required to generate an information carrier. For example, approximately 100eV or more is required to create each scintillation photon and photoelectron in conventional Anger cameras. This puts a fundamental limitation on the energy resolution can be achieved on scintillation detectors. Due to the indirect detection scheme and inefficient conversion from scintillation photon to corresponding photoelectrons, the number of generated photoelectrons are assumed to follow Poisson statistics. However, the Fano factor, which is defined as the ratio of the variance to the mean for the photoelectrons, is always found to be larger than one [31]. This means the energy resolution is not only determined by the Poisson statistics but also some other factors.

1.4.2 Advantage of CdTe/CZT Detectors

Physics Characteristics

Comparing to the conventional scintillation detectors, semiconductor detectors have several attractive features for detecting X-ray and low energy gamma-rays. The history of semiconductor detectors involves extensive use of silicon and germanium based detectors in numerous spectroscopy application. The drawback of using these detectors is that they must be cooled to liquid-nitrogen temperature (Si does not necessarily need such stringent cooling condition) to avoid thermal electronic noise. Besides this, the atomic number of Si (14) and Ge (32) is relatively low, which make them inefficient in detecting nuclear medicine X-ray and gamma-ray photons.

Unlike Si and Ge, the Cadmium Telluride (CdTe) and Cadmium Zinc Telluride (CZT) detectors have several more attractive features in addition to high energy resolution. They potentially have high spatial resolution, high energy resolution, relatively high detection efficiency at low energy X-ray and gamma rays, and room temperature operation capability. Detectors made by this type of material have been investigated for many uses in medical imaging, especially in SPECT applications. The band gap of CdTe and CZT detectors is around 1.4-1.6eV, and the energy required to generate an electron-hole pair is approximately three time of this, or about 4.5eV. The relatively large band gaps lead to small leakage current and make the room temperature operation feasible. And the atomic number of Cd and Te are 48 and 52, respectively. The density of CdTe is approximately 6.0g/cc. So the crystal has a definite advantage over Si and Ge on detection efficiency. The direct x-ray or gamma-ray conversion into electron-hole pairs helps to achieve high energy resolution. With the increase of the number of information carriers, the statistical limit on energy resolution is reduced in the semiconductor detector. And greater amount of signal charge carriers also leads to a better signal-to-noise ratio (SNR) for a given electric readout noise. Take the 140keV gamma-ray coming from Tc-99m for example, approximately 31000 electron-hole pairs can be generated. The Poisson statistics variance of this number would be about 176, which leads to a theoretical energy resolution down to below 0.5% at 140kev. The Fano factor is about 1/6, so the statistical variation on 31000 is actually about $1/6\times176=29$, and the theoretical energy resolution is only around 0.09%. In reality, there are several factors that prevent us from achieving this resolution at the current technology level. The main reason is the electron trapping in the crystals during the drift. The finite resistivity and electric noise caused leakage current will also contributed to the energy resolution degradation. The typical energy resolution reported is about 2-5% in small pixel CdTe/CZT detectors.

The high energy resolution can be used for scatter rejection and multi-isotope imaging. With the crystal growth techniques improvement, CdTe/CZT detectors also allow for high spatial resolution. Detectors of different pixel sizes have been investigated by several research groups [32-33]. When the pixel size gets too small (smaller than the size of the electron cloud), severe charge sharing and charge lost will happen which will degrade the energy resolution. So there is a tradeoff between the small pixel size and high energy

resolution. In this dissertation, 350μm pixel size detectors are used with high energy and spatial resolution. Besides the advantages mentioned above, the CdTe/CZT detectors can be made sufficiently compact and MR compatible, which leads to the effort of developing simultaneous multi-modality imaging instruments. In pinhole SPECT imaging, high resolution and compact detectors have the potential of allowing more detectors and pinholes placed around the animal using larger magnification. The MRC-SPECT system investigated in this dissertation is based on novel energy resolved photon counting CdTe detectors and the advantage of CdTe/CZT detector used for this system will be discussed throughout this dissertation.

A brief review of Schokley-Ramo theorem

In this section, we will briefly review the induced charge signal collection process. When a gamma-ray interacts with the semiconductor detectors through one of the three major interactions, an electron (in photoelectric or Compton effect) or an electron-positron pair (pair production) are generated. The electron or positron will lose their energy by ionizing the material. In semiconductor detectors, the ionization will kick out electron-hole pairs, and the number of the electron-hole pair is proportional to the gamma-ray energy deposited in the crystal. So the energy loss by the gamma ray can be calculated by the reading out the number of electron-hole pairs.

In order to get the number of the generated electron-hole pairs, a bias voltage is applied to the cathode and anode of the detector, which generates corresponding electric field across the semiconductor detector. The electrons move towards the anode and the holes move towards the cathode under the electric field. The movement of the charge carriers (electrons and holes) will induce signals on the electrodes. The Schokley-Ramo theorem provides a way to calculate the signal induced on the electrodes during the charge carrier movement. A detailed review of this theorem can be found at [34].

The Schokley-Ramo theorem states that the signal (charge) ΔQ induced on electrode L by the movement of charge q from initial position X_i to final position X_f can be written as:

$$\Delta Q = \int_{Xi}^{Xf} qE_0 \cdot dx = -q\,(\varphi(X_f) - \varphi(X_i)) \qquad (1.1)$$

E_0 and φ are *weighting field* and *weighting potential* respectively, which are defined under the condition that the electrode *L* is set to be unit potential, all the other electrodes are at zero potential and all the space charges are removed.

From equation 1.1 we know that the induced charge signal in specific electrodes can be calculated as long as we get the weighting potential. The change of the induced charge on electrode L is only determined by the start and stop position of the charge carriers, and is independent of actual electric field and the space charges inside and detector materials. The actual electric field will only determine the charge carrier movement trajectory and speed. So the equation above generally provides an easy way to calculate the induced signal on electrodes in complex detector configurations.

The weighting potential φ can be determined by solving Possion's equation:

$$\varphi = -\frac{\rho}{\varepsilon_0} \tag{1.2}$$

Here ρ is the space charge and ε_0 is the permittivity. As discussed above, the weighting potential is calculated at the condition that all the space charges are removed, the ρ should be set to zero. Equation 1.2 becomes Laplace's equation:

$$\nabla^2\varphi = 0 \tag{1.3}$$

For detectors with complicated configuration, for example the pixelated detectors, the weighting potential is typically calculated by numerical software such as Maxwell 3D.

Small pixel effect and pixelated detector

The pixelated detectors can provide two dimensional information of the incoming gamma ray interaction positions, which is important in imaging applications. The small pixel effect comes back to 1930s when Schokley and Ramo describe the phenomenon. Barrett *et al.* (1995) describe the small pixel effect in semiconductor detectors and conclude that large anode will have holes contributions and small anodes tend to only see the signals due to the movement of electrons. This is known as the single charge carrier detector operation. Below is a sample anode weighting potential picture of a pixelated detector. It can be seen that the weighting potential in most area is close to zero and sharply increase to one near the anode, which demonstrates the induced signal on anode is mainly contributed by the

electron movement. This is to say, as the electron drifts toward the anode, the induced charge on the collected electrodes remains small when the electrons are far away from the anode, and increases quickly when electrons arrives at the vicinity of the collecting anodes.

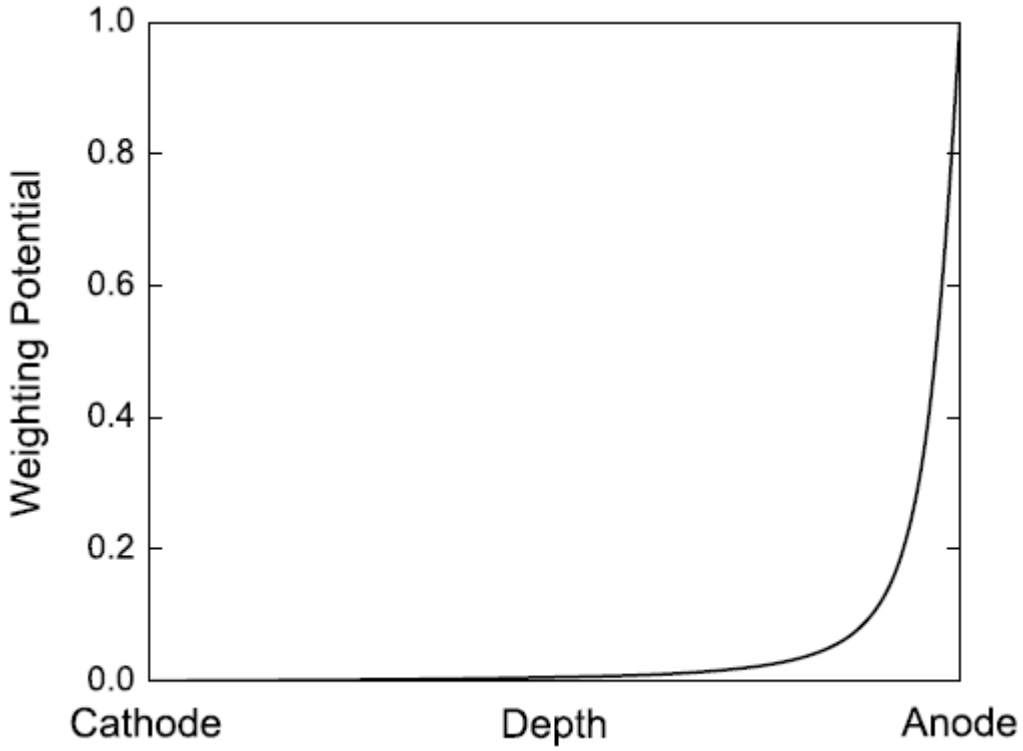

Fig. 1.2. A sample weighting potential curve (anode) of a pixelated detector

1.5 Introduction of MR-compatible SPECT (MRC-SPECT) System

Multi-modality imaging system is playing an important role in recent clinical and research applications. Combined MRI and nuclear imaging systems such as MR/PET and MR/SPECT have shown great potential and drawn substantial research effort in the past few years. The MRI could provide the anatomical structures of particular organs, tissues or cells with much better soft tissue contrast than that of conventional X-ray CT, and the nuclear imaging techniques are capable of following functional metabolism of them over time in normal or diseased condition. Extensive efforts have been devoted to the development of MR/PET system [35-42]. Comparing to the MR/PET, the development of

MR/SPECT is lacking to some extent, mainly due to the stringent requirements on MR compatible SPECT detectors and the interference between these two imaging modalities. To implement the simultaneous imaging of two systems, the key effort is to minimize the interference between the SPECT and MRI. On one hand, all the SPECT inserts have to be made of low magnetic susceptibility materials, including the detectors, mechanical supporting gantry, shielding, collimation materials and other system necessary components, to avoid the degradation of MR images. On the other hand, the SPECT image distortion due to the strong magnetic field needs to be carefully investigated. Wagenaar et al. has reported the design considerations of an MRI compatible SPECT system based on CZT detectors [43]. A prototype of MRI compatible SPECT system developed by the same group has been reported in [44-45]. Breton et al. [46] and Goetz et al. [47] have reported the use of a conventional PMT based SPECT system placed outside a low field (0.1 T) MRI system for dual-modality small animal imaging.

The motivation of this dissertation work is not only build a working MR compatible SPECT (MRC-SPECT), but also a system being able to deliver the state-of-the-art imaging performance. The target performance of the MRC-SPECT is of sub 500μm spatial resolution inside MR scanners. In this dissertation, the design and performance of an ultrahigh resolution stationary MR compatible SPECT (MRC-SPECT) system will be discussed. Comparing to all the other existing system available, the MRC-SPECT is designed to be a super compact, dual-modality, and reliable imaging system with ultrahigh spatial resolution. It combines the state-of-the-art semiconductor detector technology, the modern system design, and a application-base-tailored image reconstruction method.

The MRC-SPECT system can be generally described as follows. First, It is based on the energy-resolved photon-counting (ERPC) CdTe detectors. Up to a total of twenty ERPC detectors are assembled as a very compact ring, which provides an adequate angular sampling capability and relatively high detection efficiency. The detectors are supported on a gantry made of high strength polyamide structure constructed using 3-D printing. This compact system can be directly operated inside an MR scanner. The detector module used in this system offers an intrinsic resolution of 350μm and an excellent energy resolution of around 3-4keV. Each ERPC detector module consists of four pixelated CdTe detectors with a total dimension of 4.5cm×2.25cm. Second, a die-cast platinum pinhole inserts and cast

lead apertures are developed for this stationary SPECT system. The multiple pinhole design ensures relatively high system detection sensitivity as well as proper angular sampling. Third, a well-defined system model and an accurate geometry calibration method is developed to derive accurate system response function. Corresponding image reconstruction package was also developed. At last, a comprehensive charge collection model inside strong magnetic field developed previously was adopted to account for the magnetic field induced distortion in the SPECT image. This model can accurately predict the detector's energy and spatial response to gamma ray incident events and then help to compensate for the event position recording error due to the strong magnetic field.

CHAPTER 2

A Prototype of the MR-Compatible SPECT

To demonstrate the performance of a CdTe detector based MR compatible SPECT system, we first built a prototype SPECT system using first generation energy resolved photon-counting (ERPC) detectors. This first generation system can be operated in a pre-existing MR scanner. In this chapter, the design and performance of this prototype system will be discussed, which leads to a further development of a stationary ultra-high resolution MRC-SPECT that is demonstrated in next chapter.

2.1 Energy-resolved Photon-counting (ERPC) CdTe Detector

This prototype SPECT system is based on the Energy-resolved Photon-counting (ERPC) detectors [48] developed in our group. The ERPC detector (Fig. 2.1) consists of multiple CdTe detectors that are flip-chip bonded onto readout ASICs. The overall dimensions of

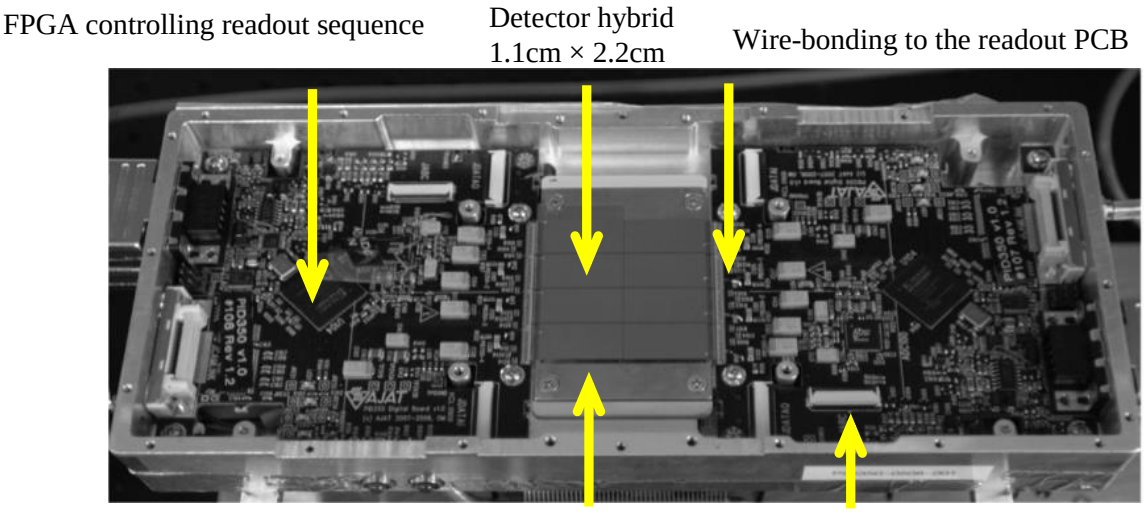

Fig.2.1 The prototype ERPC CdTe detector

each ASIC are approximately 22 mm×11 mm, accommodating a total of 2048 readout channels arranged in an array of 32×64 pixels (Fig. 2.2). The pixel pitch size is 0.35 mm × 0.35 mm, which matches the pixel configuration of the CdZnTe or CdTe detectors in use. Each CMOS pixel has a bump-bonding pad of 25μm in diameter. The pixel readout circuitry includes an AC-coupled charge-sensitive amplifier, a peak-hold (P/H) circuit, a comparator and a multi-function counter used for both photon counting and A-to-D conversion. The pixel circuitry also contains various logic units for controlling, address

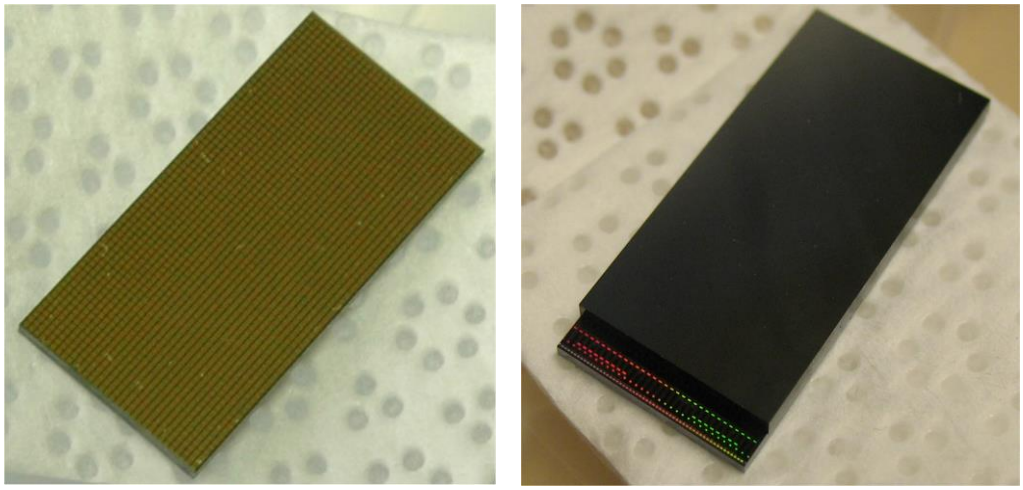

Fig.2.2 (Left) Image of a CdTe detector with 350μm pixels.
(Right) A CdTe/ASIC hybrid.

decoding, and selection between readout modes. The amplifier has a shaping time of ~1 μs. The comparator in each pixel has a typical differential topology that uses an external analog control voltage to adjust the threshold level. All the wire-bonding pads, including the control signals, power feeds, and output signals, are located on one side of the ASIC. In order to compensate for the pixel-to-pixel variations in the channel offset and gain, each channel is also equipped with two 8-bit digital-to-analog converters (DACs). These allow accurate alignment of the readout channels on the detector.

One of the key features of the ERPC ASIC is the capability to perform on-pixel A-to-D conversion with variable precision (6 bit or 8 bit). Following an interaction in the detector, the trigger signal from an anode pixel is used to initiate a time-to-digital converter (TDC) located on the same pixel. At the same time, the triggering signal is also used to start a

ramp generator. The ramp generator is implemented using an 8-bit digital-to-analog converter (DAC) that is driven by a clock signal operating at 10 MHz. The ramp generator outputs a steadily increasing ramp signal that is compared with the signal amplitude held by the on-pixel P/H circuitry (Fig 2.3, right). When these two amplitudes are sufficiently close to each other, a trigger signal is generated to stop the TDC. Therefore, the output of the TDC is proportional to the signal amplitude induced on the corresponding anode pixel. Depending on the desired count rate capability, the analog signal can in principle be digitized with different precision by changing the step size of the ramp generator. For each event, it takes a maximum of <10μs to perform a 6-bit A-to-D conversion and around 25.6μs for an 8-bit conversion. After the A-to-D conversion, the pixel address and the digital amplitude are sent out, and the ASIC is reset to receive future incoming events. Using this readout mode, each ASIC is in principle capable of handling 0.1 M counts per second (cps) with 6-bit ADC precision and 25 kcps with 8-bit precision. If necessary,

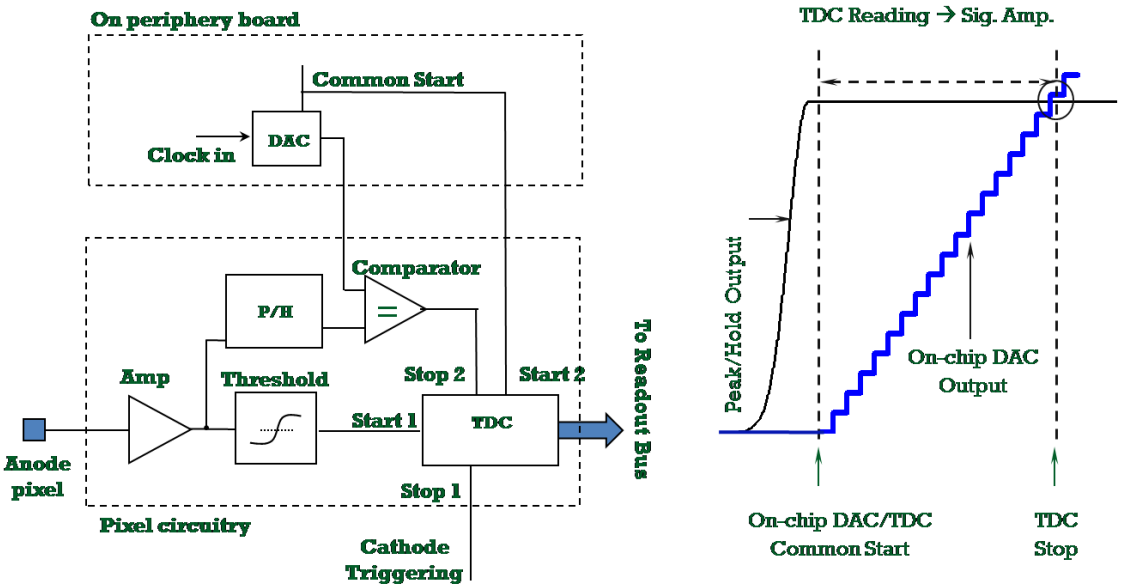

Fig. 2.3. The ERPC ASIC pixel circuitry

the eight ASICs on each ERPC detector can be designed to operate independently. Therefore, the entire ERPC detector is capable of a count rate of 0.2 Mcps with 6 bit ADC precision. For high resolution SPECT imaging, the event rate exposed to gamma ray detectors is generally limited by the use of high-resolution collimation apertures.

Therefore, the count rate of the ERPC detector should be more than adequate for most high-resolution SPECT applications.

The hybrids are wire-bonded to readout printed circuit boards (PCBs) as shown in Fig. 2.1. These PCBs provide the power feed, logic and timing signals, and data pathway for the ASICs. Each readout board also has a 32 MB data buffer for temporary storage of pixel addresses and digital signal amplitudes. The readout operation of the camera is controlled by FPGAs mounted on the digital boards, which act as a bridge between the ERPC ASICs and the control software. The eight ASICs are mounted onto a copper back-plate that is attached to a peltier cooler for heat dissipation.

The energy resolution is around 3-4keV at 140 keV for the 1mm CdTe detector single pixel as shown on Fig. 2.4. The 2mm CdTe detector is of a little lower energy resolution than that of 1mm detector, possibly due to more charge carrier trapping. Energy spectrum with events acquired on all 16384 pixels after correcting the channel-by-channel variation of gain and offset is shown in Fig. 2.5. At each channel, the so-called gain and offset follows the linear equation:

$$detected\ energy\ bin = gain * E + offset$$

Where the E is the deposited energy.

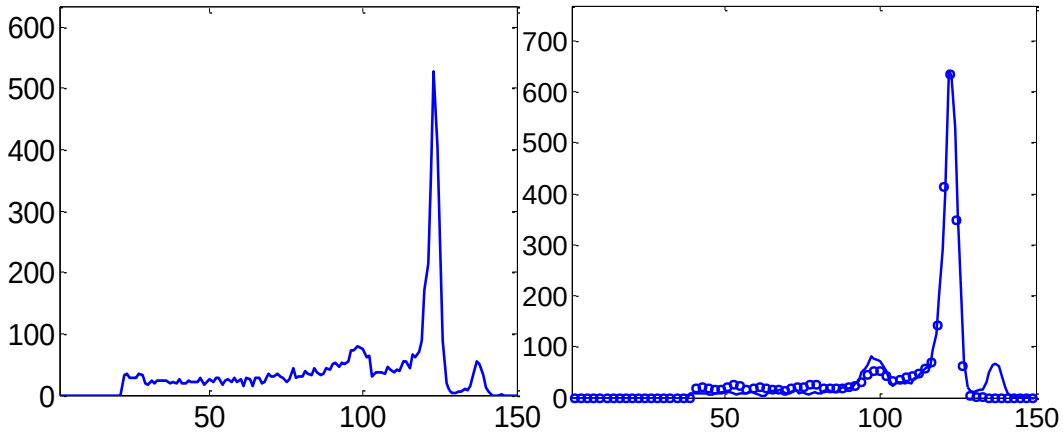

Fig. 2.4. Energy speatra measured on single pixel of 1mm/2mm CdTe ERPC detectors (Left: 1mm CdTe, E.R=3.51keV; Right: 2mm CdTe, E.R=4.62keV).

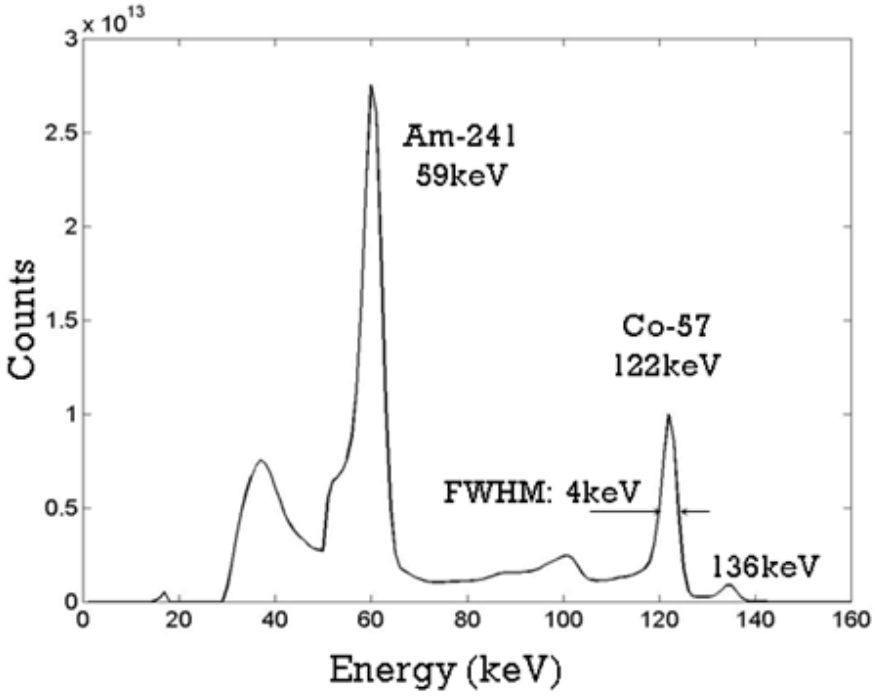

Fig. 2.5. Energy spectrum with events acquired on all 16384 pixels after correcting the channel-by-channel variation of gain and offset

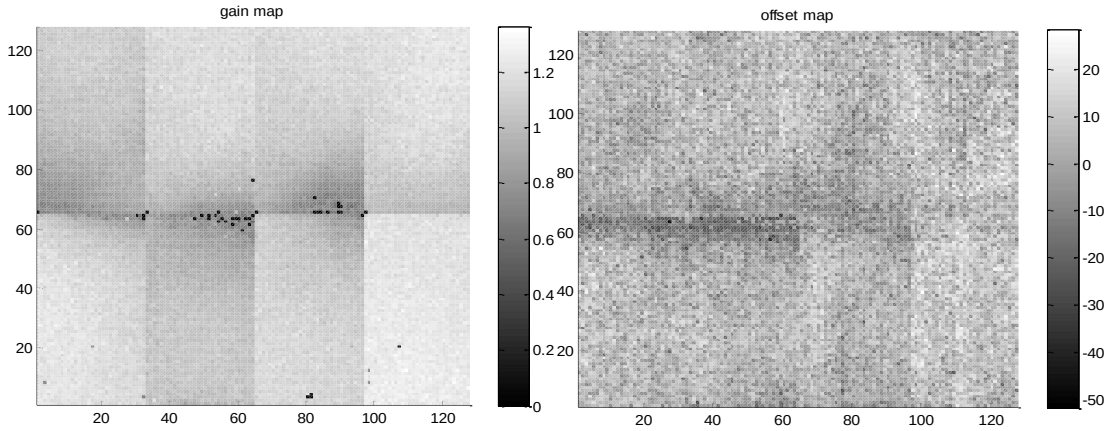

Fig. 2.6. The distribution of channel gain & offset values across 16384 detector pixels. Dead pixels are <0.2% on the CdTe detectors.

The uniformity of the ERPC detectors with the flood source irradiation is also evaluated. The full-energy peak positions for Co-57 (122keV) and Am-24(59.9keV) gamma-rays

were used to determine the gain and offset values for each of the 16384 pixels (Fig. 2.5). The distribution of pixel-wise gain and offset values are shown in Fig. 2.6, which demonstrated a relative uniform response of the detector over the 128×128 pixels. There are less than 0.2% of pixels on the current detector that exhibited very low gain and therefore marked as the dead pixels. The table below list the performance of the ERPC detectors.

Detector Parameters	Parameter values
Entire imaging area	4.4 cm × 4.4 cm
Each detector hybrid size	1.1cm × 2.2 cm
Pixel pitch size	350μm × 350μm
Total pixel number	128 × 128
Preamplifier gain	10 μV/electron
Shaping time	1 μs
Readout mode	a): Photon counting b): Energy-resolved readout with on-pixel ADC
Energy resolution	3-6keV @140keV
Dynamic range	20-250keV
Dead pixels	<0.2%

Table 2.1. First generation ERPC detector parameters

2.2 Hybrid Pixel-Waveform Readout System for ERPC Detector

This section will discuss a modified small pixel CdTe/CZT detector designed for sub-500μm resolution SPECT imaging application inside MR scanner based on a recently developed hybrid pixel-waveform (HPWF) readout circuitry [49]. The HPWF readout system consists of a 2-D multi-pixel circuitry attached to the anode pixels to provide the X-Y positions of interactions, and a high-speed digitizer to read out the pulse-waveform induced on the cathode. The digitized cathode waveform could provide energy deposition information, precise timing and depth-of-interaction information for gamma-ray interactions. There are several unique attractive features with this HPWF detector system. To demonstrate the performance, we constructed several prototype HPWF detectors with pixelated CZT and CdTe detectors of 2-5 mm thicknesses, connected to a prototype readout

system consisting of energy-resolved photon-counting ASIC for readout anode pixels and an Agilent high-speed digitizer for digitizing the cathode signals. The performances of these detectors based on HPWF will be discussed in this section.

We have gone through the basic design of the novel energy-resolved photon-counting (ERPC) sensor that offers a very-high spatial resolution, an excellent energy resolution for future SPECT applications in section 2.1. Although the current detector has great performance in terms of spatial and energy resolution, the readout methods still have several limitations for further improving the performance of CdTe/CZT-based imaging detectors.

The first major challenge is how to obtain a good energy resolution with CdTe/CZT detectors having very small pixels (sub-250 μm pixels). Although the (lateral) spatial resolution could be improved by using smaller and smaller pixels, both charge sharing and charge loss (in the gaps between pixels) could severely degrade the charge collection efficiency (CCE) and therefore the energy resolution, especially when the physical dimensions of anode pixels is approaching the average size of the electron cloud created by gamma ray interactions. This issue has been extensively studied with both Monte Carlo simulation and experimental work based on several CZT detector systems [50-55]. Several groups have used steering electrodes between collecting contacts [56-58] to improve CCE, which helped to improve the energy resolution for multiple-pixel events. However, this approach is difficult to implement with detectors having very small pixel pitch sizes, due to the limitations in current detector fabrication techniques. Another apparent approach is to develop multiple pixel readout circuitries that allow one to obtain energy information on individual pixels and then sum these signals, as with the Medipix3 readout chip [59-61]. This approach allows one to compensate for the charge sharing between pixels, but it does not provide precise information on charge lost between the small pixels. This results in an inevitable loss in energy resolution.

As a side effect, the lack of precise energy-information from the small pixels and the frequent occurrence of multiple pixel events will also lead to unreliable estimation of the depth-of-interaction (DOI) using the ratio between cathode and anode signals [58]. Although the DOI could still be estimated by direct measurement of electron drifting time,

as in the 3-D CZT detectors [62-63], it would be challenging to develop a readout system that can handle a large number of sub-250um pixels, while allowing one to derive the electron drifting time on each event. For medical applications, CdTe/CZT detectors would typically need to be operated at a relatively high count-rate. This would further increase the complexity of the readout system, if such a system were to be developed.

The second major challenge for CdTe/CZT detectors is their limited timing resolution. For example, CZT material has a relatively low charge-mobility (at the order of 10^3 $cm^2/V•s$ [64]). For CZT detectors of above 5 mm in thickness, a relatively long time (a few hundred ns) is typically required to collect the electrons. Furthermore, the actual charge collection process for each interaction will also be affected by the material non-uniformity along the particular drifting trajectory and the local field configuration around the collecting anode. Therefore, it is difficult to obtain good time resolution with conventional analogue triggering on either the cathode or the anode signals [65-66]. The limited timing resolution is among one of the major concerns for using CZT detectors for PET applications.

The third major challenges for developing future small pixel CZT detectors is how to reduce the complexity of small pixel readout systems, whilst providing the critical information (3-D spatial coordinates, energy and timing information) in a high count-rate environment. As the number of channels per unit area will be inversely proportional to the square of the pixel dimension, one would be looking at an astronomical number of readout channels operated simultaneously inside a medical imaging system. We would acknowledge that simply scaling down existing pixel readout circuitries could be feasible in the near future, thanks to the rapid advance in CMOS fabrication technologies. However, it would be desirable to explore how to simplify the pixel readout circuitry from power consumption, heat generation, cost-effectiveness and system reliability viewpoints. This is particularly important, when we are pushing towards CZT detectors with small and smaller pixels for a broad range of medical imaging applications.

To alleviate these challenges above, we developed two versions of small pixel CdTe detectors with 350μm and 100μm pixels read out by hybrid pixel-waveform scheme. This readout system consists of a 2-D multi-pixel circuitry attached to the anode pixels to

provide the X-Y positions of interactions, and a high-speed digitizer to sample the waveform induced in the cathode. This configuration offers several attractive features for very small pixel detectors, and benefits the analysis of charge collection inside MR scanner. First, the cathode waveform could provide reasonably accurate energy information using digital processing techniques that takes into account the effect of charge trapping, different drifting velocities of charge carriers. Second, this method could provide reliable DOI by measuring the electron drifting time from sampled waveforms. The DOI information could substantially improve the charge collection analysis inside strong magnetic field since a large fraction of incident gamma-rays are not perpendicular to the crystal surface. Finally, the HPWF readout system requires a highly simplified circuit for handling the large number of anode pixels. It will potentially allow one to pack more readout channels per unit area with future generation CMOS ASICs.

The prototype HPWF-CdTe/CZT detector and a design module are shown in Fig. 2.6. The CdTe/CZT detector is bump-bonded onto ERPC readout ASIC with the same pixel patterns (350 μm × 350 μm). Each pixel channel has pre- and shaping amplifiers, a discriminator and peak/hold circuitry. The cathode signals will be read out with a dedicated digital waveform sampling circuitry. The Fig. 2.7 (top) is a prototype HPWF readout based detector system used for performance validation. The whole prototype system is installed in a brass box, which is used to help shield outside interference noise signals. It is of great importance to reduce the noise associated with the cathode waveform. Otherwise the waveform fitting would have extra error caused by the noise. Fig. 2.7 (bottom) demonstrates the design profile for the HPWF readout integrated ERPC detector.

By fitting and digital shaping the cathode waveforms, the energy deposition, electron and hole drifting time, and the interaction timing can be derived [65-66]. The depth of interaction can be derived by electron and hole drifting time. Figure 2.8 shows the cathode sample waveforms fitting results with a Na-22 source irradiating on a 2 mm thickness CdTe detector. The DOI resolution is estimated to be 0.3mm with the 2mm detector. The depth information will help to more precisely derive the detector charge collection process inside strong magnetic field, which will potentially improve the SPECT image taken inside the MR scanner. The Na-22 energy spectrum can also be derived by digital shaping the cathode

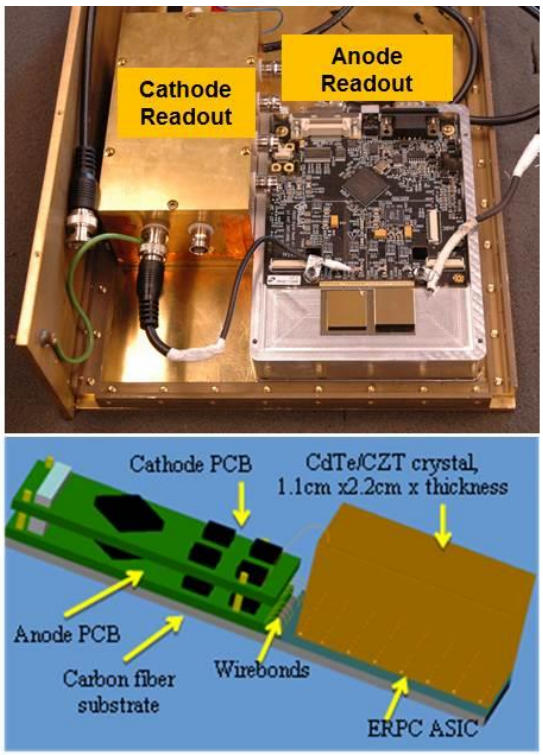

Figure 2.7. A prototype HPWF CZT/CdTe detector (top) and a design module of compact HPWF detector (bottom)

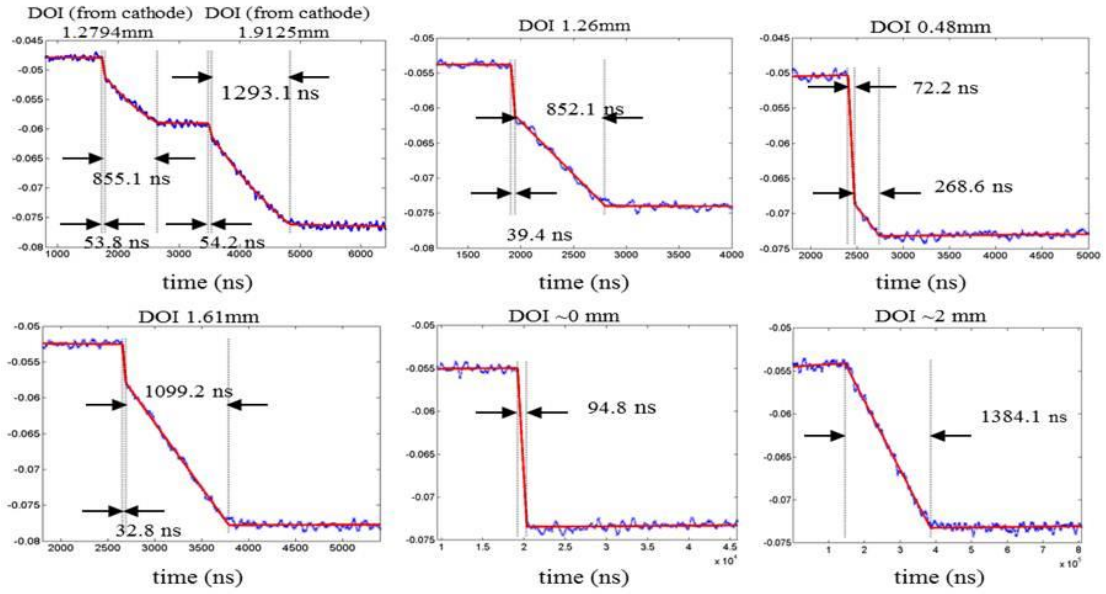

Figure 2.8. DOI derivation based on cathode waveform fitting. The DOI is from the cathode side. Six cases here represent interactions happened in different positions. (For example, top middle is a standard scenario, bottom middle interaction happens close to the cathode, top left is a multiple interaction scenario)

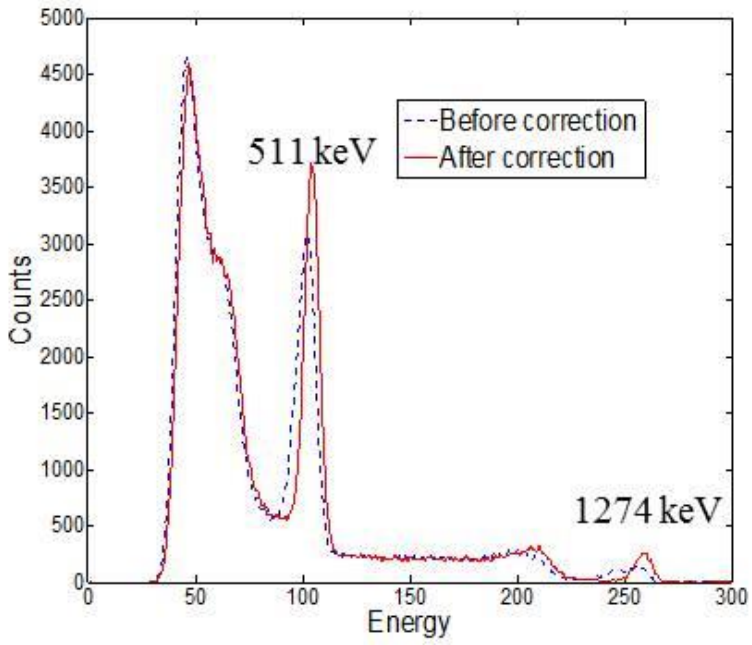

Figure 2.9. Na-22 energy spectra measured with sampled cathode waveforms, the correction represents the hole trapping compensation with different DOI.

waveforms and the result is shown in Figure 2.9. The study and results shown here is based on the experiment outside MR scanner.

2.3 Development of a Prototype MR-compatible SPECT System

In this section, a prototype SPECT/MR system development is discussed. As a dual-modality SPECT/MR system, it is important to minimize the interference between the two modalities. Previous work in our group has demonstrated the feasibility of applying ERPC detector to construct an MR compatible SPECT system. Besides the compatibility of the detector, a series of materials for use in supporting, shielding and collimating structures are also tested to build a prototype of the MRI-compatible SPECT system [66]. The Fig. 2.10 below demonstrate the MR compatibility test carried out previously. The effect of different system materials on the MR image was investigated. For this prototype system, we made a supporting gantry by using non-magnetic materials such as carbon-fiber, brass and aluminum (Fig. 2.12 & 2.13). This non-magnetic gantry allows the system to be moved in and out of the scanner. The system can rotate around the object to obtain a sufficient

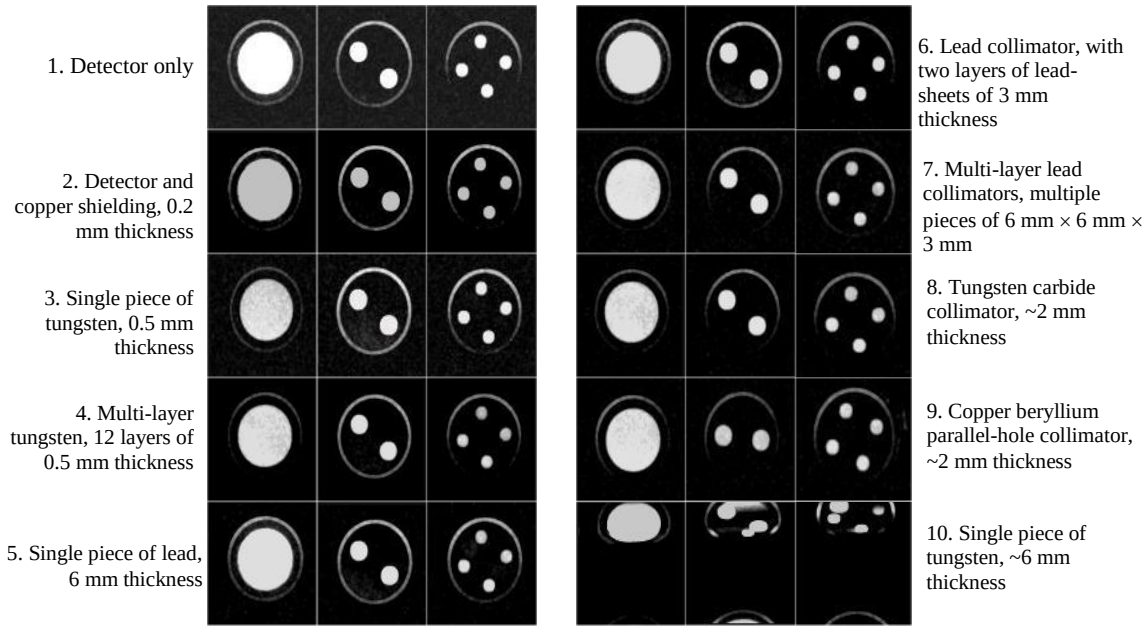

Fig. 2.10. MR images of the phantom in the presence of certain SPECT components. The images were acquired with the spin echo sequence that is routinely used for mouse brain studies.

angular sampling by a non-magnetic manual rotation stage. Two or four camera heads can be supported on a gantry rotating around the horizontal axis at arbitrarily chosen angular steps. For safety concern, the detector ASICs are cooled down by blowing compressed air onto copper heat sink attached. All the power supplies and other electric devices are outside the MR scanner room and connected to the detectors by long extension cables.

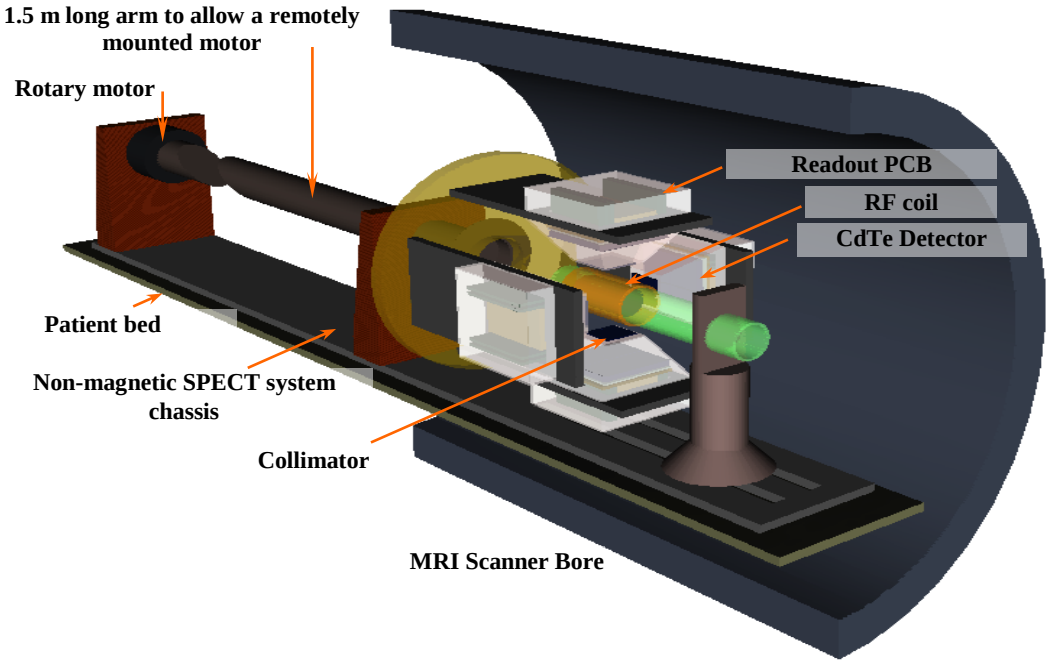

Fig. 2.11 The prototype SPECT system drawing with the existence of MR scanner

The first generation of pinhole collimator used in the prototype is square shape lead collimator with 3×3 tungsten pinhole inserts. The distance between nearest pinholes is around 7 mm, but the actual pinhole position was randomly moved around the grid point to avoid oversampling at certain discrete spatial frequencies. The body of the aperture is made of lead sheet of 8 mm thickness. It has nine through holes, each with a pinhole-insert inside. All pinholes in the aperture are pointing towards a focal spot that is 3.5cm from the central plane of the aperture. The pinhole inserts are made of pure tungsten. They are 6 mm tall and have an acceptance angle of 60 degrees on both sides. The diameters of the pinholes are ranging from 200 to 400μm diameter. The central axial section of the pinholes has a channel of 100μm length. The fact that the pinhole inserts are 2 mm shorter than the thickness of the lead sheet and all pinholes are pointing to a focal spot give rise to a complicated pinhole geometry that needs to be mathematically modelled for an accurate geometrical calibration and reconstruction. The distance between the detector surface and the rotation axis is designed to be around 75~78 mm. The distance from the rotation axis to pinhole aperture is about 35mm (SPECT system magnification ~1.2).

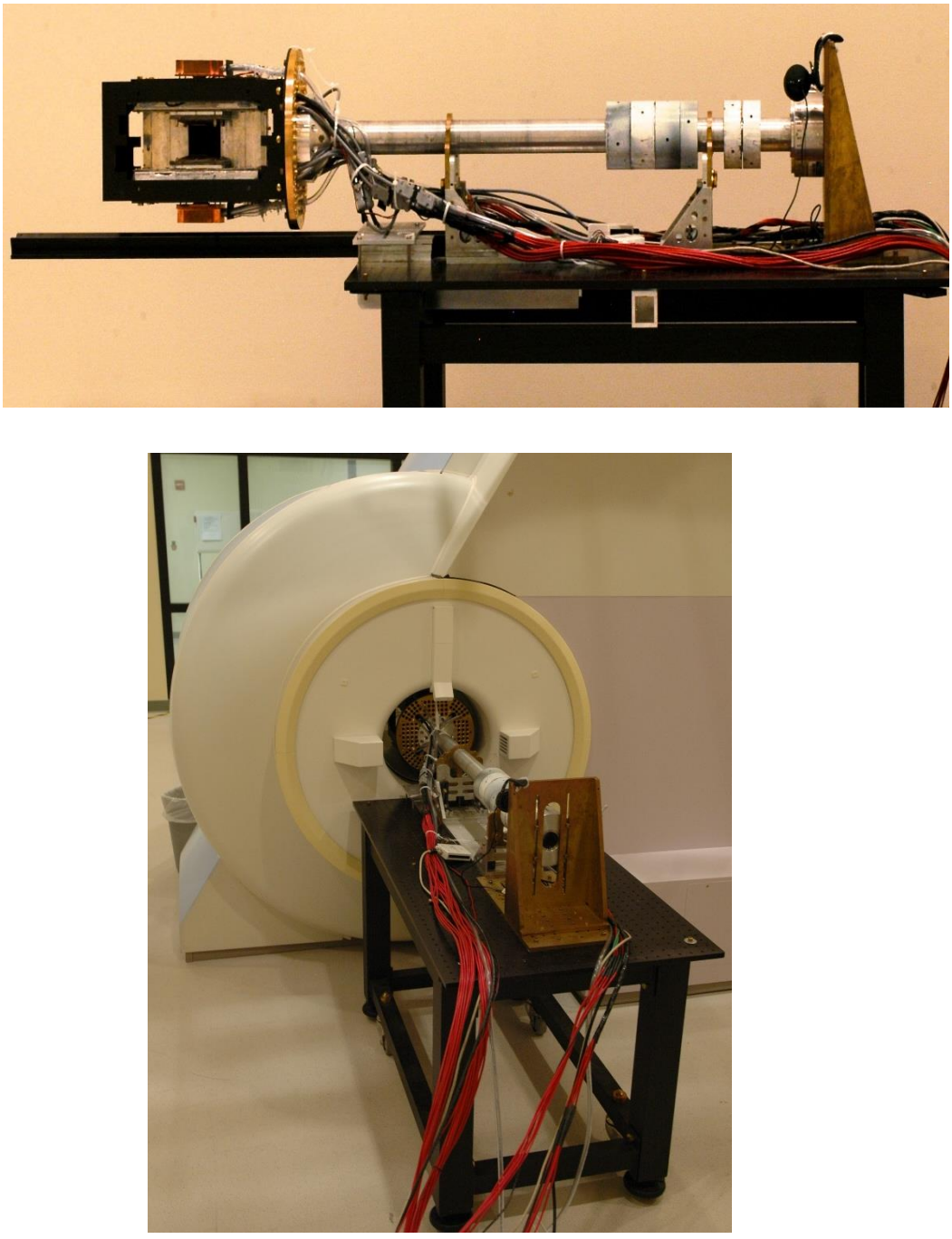

Fig. 2.12. The prototype of an MR compatible SPECT system (top: portable SPECT system on a MR safe cart; bottom: System operating inside a Siemens 3T scanner)

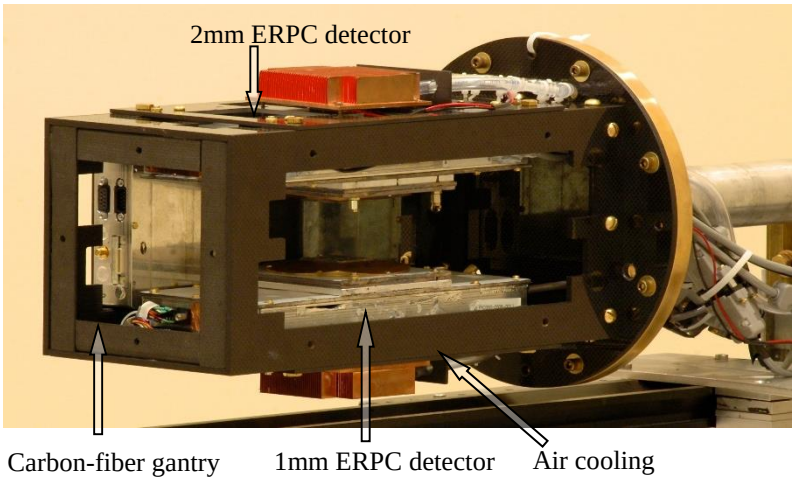

Fig. 2.13. Four-head SPECT system based on ERPC CdTe detectors, the gantry is made of carbon-fiber materials to achieve better geometry stability (only three detectors are shown here)

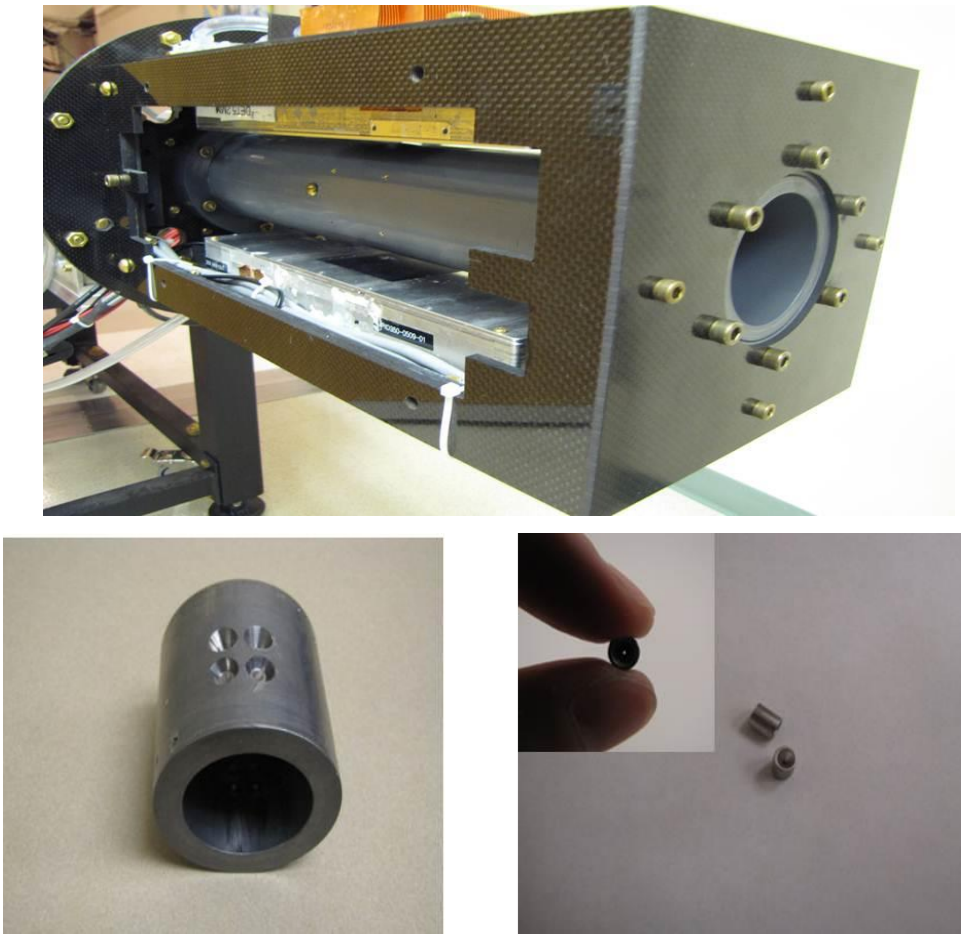

Fig. 2.14. Prototype system using new cylinder aperture with Pt inserts design

Besides the square lead aperture with tungsten inserts, a die-cast platinum pinhole inserts and cast cylinder lead aperture are also fabricated to evaluate the system performance. This led to the decrease in weight of the SPECT system, which benefits the system stability and rotation smoothness. It also provided better gamma-ray shielding for the detectors. The lead aperture tube and the platinum based pinhole insert are shown in Fig. 2.14. The thickness of the lead aperture is 9mm, which provides sufficient shielding for the detectors. The new designed 300μm pinhole (Pt/In alloy) also has better performance than tungsten pinholes due to larger stopping power. The object to aperture distance is designed to be around 24mm, and the distance between aperture and detector is around 36mm (can be adjusted if necessary). This configuration ensures that the SPECT system enjoys high spatial resolving capability while not suffering too low sensitivity. A solid PVC tube is constructed to fix the cylinder aperture to the carbon-fiber gantry. The performance of this modified prototype system serves as importance reference for future stationary whole ring SPECT system design, which will be discussed in next chapter.

2.4 Geometry Calibration of the Prototype SPECT System

An accurate geometrical calibration is of great importance for achieving SPECT image with high spatial resolution. We developed a comprehensive system model to precisely calibrate the geometrical parameters for the SPECT system. In this particular method, a Co-57 point source with 250μm diameter spherical active area is supported on a linear translation stage that can move the source along the horizontal axis. At each axial position, the detection system can be rotated at arbitrary steps to record the corresponding projections. The accumulation process is controlled by Labview-based user interface. Parameters such as rotation steps, accumulation time for each step can be set in the user interface.

A Levenberg-Marquardt algorithm based calibration method is developed to accurately depict the system geometry information. The basic idea is to minimize the difference between the experimental and programming simulated projections from the SPECT system. The key factor to achieve precise geometry calibration lies on the accurate definition of system response function and precise geometry description. For each camera

head, there are 65 parameters (for 3×3 pinhole) defined to account for the geometry. The rotation axis is defined as a global X axis. Two parameters are used to present the initial position of calibration point source in the Y-Z plane (assume that the initial position of the calibration point source in the X axis is zero). Six parameters are used to provide the central position and surface direction of the detector. We also define three parameters to consider the angle between the rotation axis and the linear translation direction. Besides these 11 parameters mentioned above, each pinhole has another 6 parameters which account for the pinhole space position and direction. Take the square lead aperture for example, at each angle, by processing the projection through the 9 pinholes, we can calculate the centroid of projection through each pinhole and use these centroid information to do geometrical calibration [68].

To better account for detailed physical response of the system, we made further improvement for the geometry calibration method. First, for 140keV gamma-ray, the penetration of the photons in detector could lead to projections of asymmetric shape. The entire projected profile instead of centroid is used in the Weighted Least Squares (WLS) fitting. This helps to account for physical factors, such as the depth-of-interaction effect in detector and the complicated pinhole geometry. Second, in the geometry calibration routine, the trajectory of point source is designed to cover the entire object space. This is implemented by scanning the point source through a larger number of axial and trans-axial positions. This process helps to determine the uniformity of the system response and to assess the accuracy of the predicted system model. The comparison of experimental and calibrated centroid is shown on Fig. 2.15 and an example projection on one particular angel is shown on Fig. 2.16. A comparison between measured and predicted projections through a single pinhole is shown on Fig. 2.17. The average root-mean-squared (RMS) distance between measured and predicted projection center under the calibrated geometry is around 50μm (~0.15 pixel).

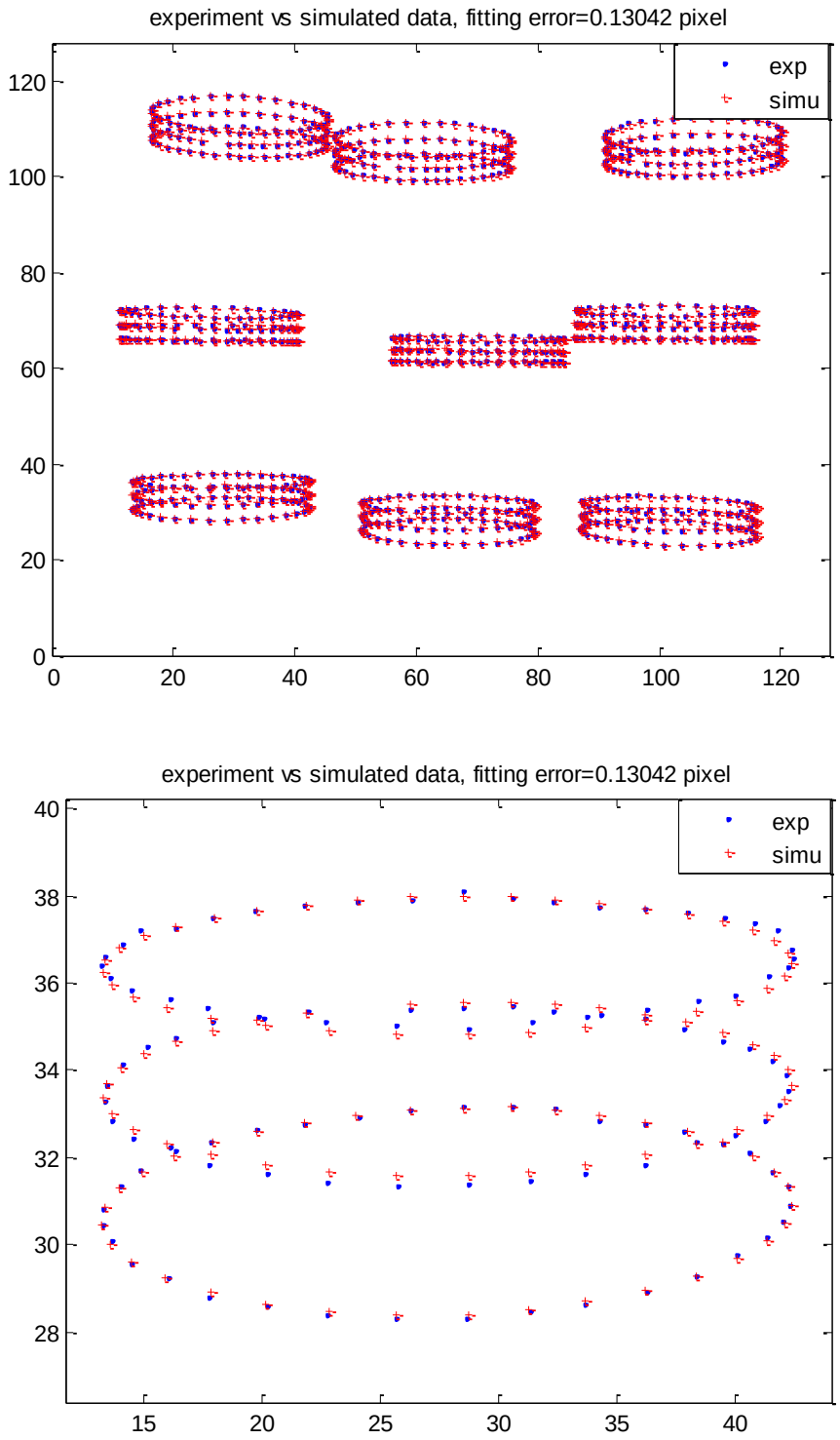

Fig. 2.15. Experimental projection centroid and calibrated projection centroid comparison in one detector, the lower is the zoomed centroid comparison through one pinhole (The 0.1342 pixel is the average experimental and calibrated centroid error)

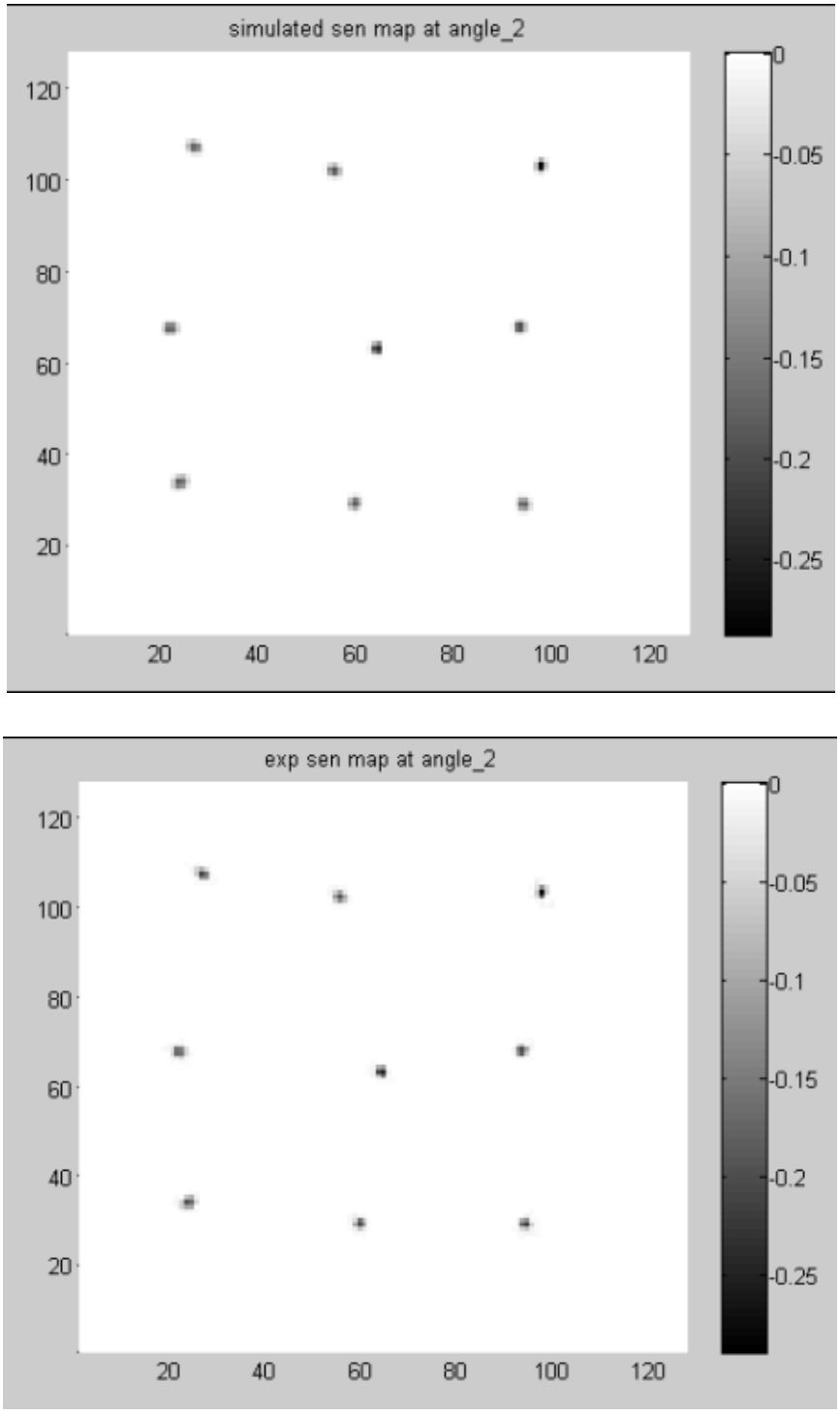

Fig. 2.16. The experimental and calibrated projections at a particular point source position. (For each pinhole projection, the experimental and calibrated probabilities have been normalized)

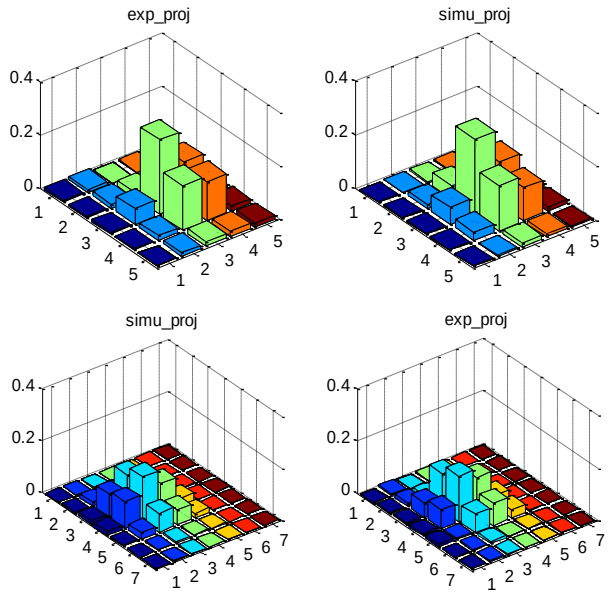

Fig. 2.17. The experimental and calibrated projection profile through single pinhole on detectors after geometrical calibration (the top two are the projections through 200μm pinhole while the lower two are from the 400μm pinhole). The similarity of the experimental and calibrated projections demonstrated the accuracy of the geometry calibration method.

Although the geometrical calibration accuracy for this prototype SPECT looks pretty good, there is a systematic error during the gantry rotation process, which is very difficult to account for. More specifically, as shown in previous system picture, the detection system is sitting on a balanced rotation gantry. During the rotation process, we assume that the rotation axis is kept steady, and we adopt this assumption in the geometry calibration process. However, there is no guarantee that this can be realized, especially in this lab-made system. We have monitored the rotation axis change using an indicator. The measurement proved the rotation systematic error as expected. It is not an easy task to fully incorporate this in the geometry calibration model since this systematic change follows no regular pattern. Upon this point, a stationary system without rotation would have advantage in deriving more accurate geometry information, which directly leading to more precise system response function. Chapter 4 has a detailed discussion on geometry calibration for the stationary SPECT system.

Accurate system response function can be generated for image reconstruction use after geometrical calibration. The probability of each voxel in the object space being detected by specific pixel in the detectors can be mathematically calculated. And all these calculated probabilities form the system response function matrix. The reconstruction method used for this system is penalized Ordered-Subset Expectation-Maximization (OSEM) [69].

For imaging studies inside the MR scanner, a charge collection model inside strong magnetic fields is necessary to compensate for the charge carrier shifting inside the crystal. Previous efforts [70] in our group have indicated that electron shifting due to the Lorenz force can be simply modeled by a parameter ɵ, where the ɵ represents the electron trajectory shift angle inside the crystal due to the Lorenz force. With the MRC-SPECT system, a point source will be put in the center of the field of view to monitor the projection difference outside and inside the magnetic field. The projection difference will be used to produce the electron shifting model in MR, which will be further applied to generate the system response function with the MR scanner existed. Section 2.5 below is a brief description of the MR correction model development.

2.5 MR Correction Model for Charge Collection

When operating the ERPC detector inside the MR scanner, the signal collection process inside the semiconductor bulk will be affected by the Lorenz force. The electron and hole trajectories will shift towards a certain direction. This effect will cause severe distortion to the reconstructed SPECT image inside the MR scanner if no correction is applied. To compensate for this distortion, a comprehensive charge collection model inside strong magnetic field is developed by Tan [70]. The charge collection process is modeled by quantitatively assessing the Lorenz effect on the migration of charge carriers inside the CdTe detector. This leads to an accurate modeling of the detector's energy response to gamma-ray interactions and then helps to refine the MR-SPECT system response function. The Fig 2.18 below is an example of this correction model. The left panel demonstrates the measured and model-based simulated projection of a pencil beam irradiating at the detector operating outside the MR scanner. The projection covers four pixels denoted as P1, P2, P3 and P4. The normalized counts and energy distribution at the four pixels are

shown. In this panel, the pixel P2 has most counts in this specific projection, while pixel P3 has the least. The right panel represents data acquired inside the MR scanner with the same geometry. It can be found that the projection still located at pixel P1, P2, P3 and P4. However, the distribution has changed obviously and the projection is shifting towards the left direction. The normalized counts and energy spectrum match each other quite well under the model developed. This model is adopted in following reconstruction process for SPECT imaging inside strong magnetic field.

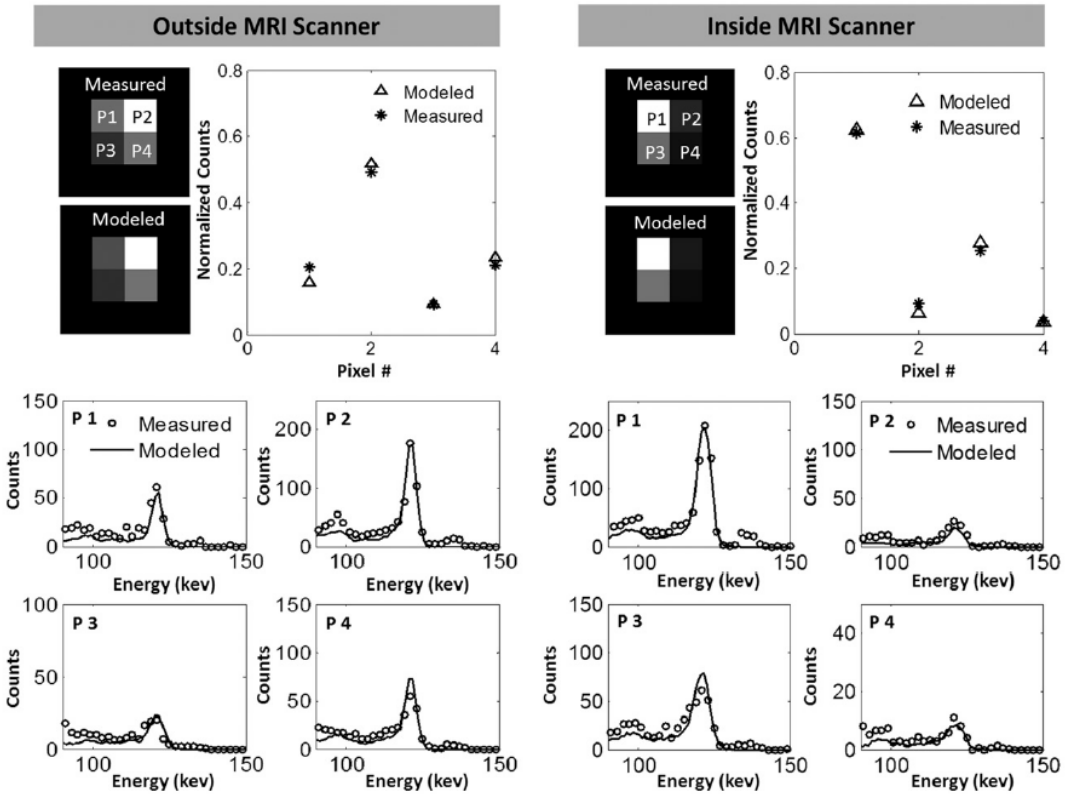

Fig 2. 18. Magnet-caused charge collection shift correction model

2.6 Preliminary Imaging Study

The SPECT imaging performance in strong magnetic field has been investigated. The images of resolution phantom were obtained outside and inside 3T MRI scanner. A lab made Jaszczak phantom is filled with 2.5mCi Tc-99m and projections are taken at 30 angles with 4 minutes data acquisition time at each angle. With the presence of a magnetic

field, there are image distortions and poor spatial resolution compared to the image taken outside MRI scanner, as we predicted. To compensate for this obvious distortion caused by Lorenz force in strong magnetic field, a new system response function is generated to compensate for the MR shift effect and the detailed correction model can be seen in [70]. By using the newly refined system response function integrating the correction for Lorenz force, the reconstructed image was compared to the image outside MRI and the one inside MRI but without any correction in Fig. 2.19. The comparison clearly demonstrates that the SPECT image with charge collection model inside strong magnetic field considered has shown much improvement in image quality and spatial resolution. The 500μm feature can be resolved after applying this correction method.

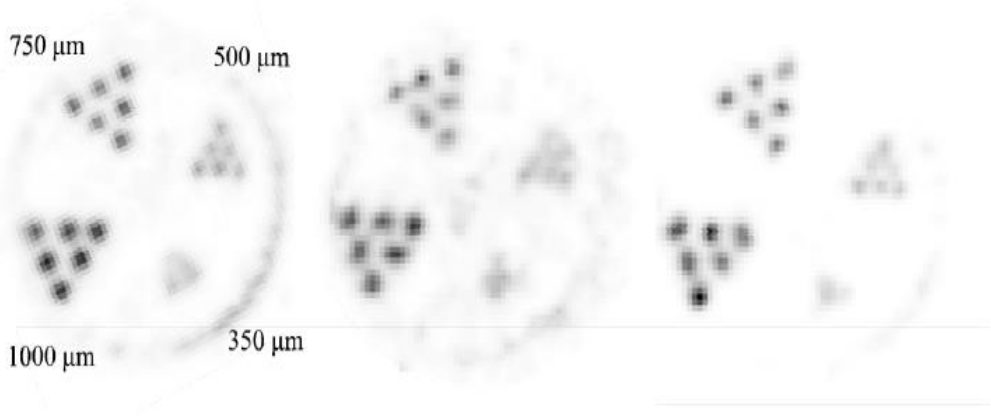

Fig. 2.19. (Left) SPECT Image of a micro-Jaszczak phantom outside the MR scanner; (Middle) SPECT image acquired inside the MR scanner without correction; (Right) SPECT image acquired inside the MR scanner with the first order correction.

CHAPTER 3

A Stationary Single Emission Microscopy Development

In Chapter 2, we have discussed a sub-500μm resolution prototype MR compatible system based on the first generation energy-resolved photon-counting (ERPC) CdTe detectors. The detector offers spatial resolution of 350μm and energy resolution of 3-4keV at 140keV. To achieve high resolution SPECT image inside the MR scanner, a comprehensive charge collection model inside strong magnetic field previously developed is adopted to precisely derive the system response function to achieve high resolution image inside MR.

Based on these previous effort, we constructed an ultrahigh resolution stationary MR compatible SPECT system based on second-generation ERPC detectors. A ten-head detector ring has been assembled to deliver a state-of-art MR compatible SPECT system with sub-500μm spatial resolution and a reasonable sensitivity. The non-rotational structure dramatically reduces the scanning time and makes the imaging study more flexible. Detailed system design and the first imaging result with this system will be presented in this chapter. Below is a picture of this fully running system working as a bench-top SPECT (left) or operating inside an MR scanner (right).

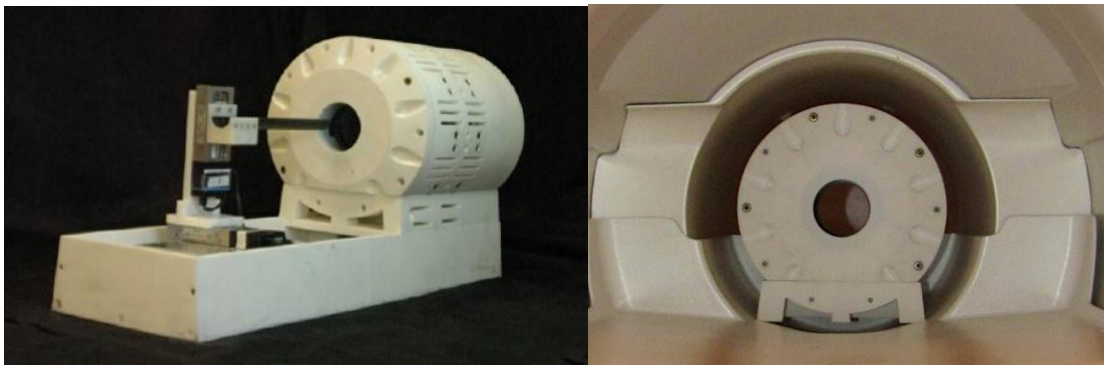

Fig. 3.1. The ultra-high resolution MRC-SPECT system

3.1 Stationary MRC-SPECT System Design

3.1.1 Detector - The Generation II ERPC Detectors

The ultrahigh resolution MR-compatible SPECT system is built around the second-generation small-pixel CdTe detector module that we have recently developed (Figure 3.2). Each module consists of CdTe detectors having an overall size of 22.5 mm × 11.2 mm × 2mm, divided into 64 × 32 pixels of 350μm in size. We have previously reported the performance of the first generation ERPC ASICs in [48]. Comparing to the previous generation, the footprint of this detector version has been changed to form a compact detector ring system. In addition, the ASICs in the Gen-II ERPC detectors allow for a much lower low energy threshold, and incorporates three gain levels for handle different gamma ray energies. The excellent energy resolution, high spatial resolution as well as MR compatibility ensures the Gen-II ERPC detector to provide promising imaging performance. The detector can also be read out with a novel hybrid pixel-waveform readout system that is designed to alleviate several challenges for using small-pixel CdTe detectors in ultrahigh-resolution SPECT imaging applications. As discussed in the previous chapter, the HPWF system utilizes a modified version of a 2048-channel 2-D CMOS ASIC to readout the anode pixel, and a digitizing circuitry to sample the signal waveform induced on the cathode [49]. The cathode waveform acquired with the HPWF circuitry offers excellent spatial resolution, energy resolution and DOI information, even with the presence of excessive charge-sharing/charge-loss between the small anode pixels. The depth of interaction can be derived by electron and hole drifting time. The HPWF CdTe detector is designed and constructed with a minimum amount of ferromagnetic materials, to ensure the MR-compatibility. To disperse the heat generated in the ASIC (each ASIC consumes power of around 0.8W), every detector is attached to an air channel embedded base plate mounting to the supporting frame shown in Fig 3.2. The ASICs are sitting on top of a delicate custom-designed high-purity copper heat sink. The compressed air comes through the embedded air channel and then blows off the heat generated. This helps to reduce the electronic noise of the detector to a relatively low level.

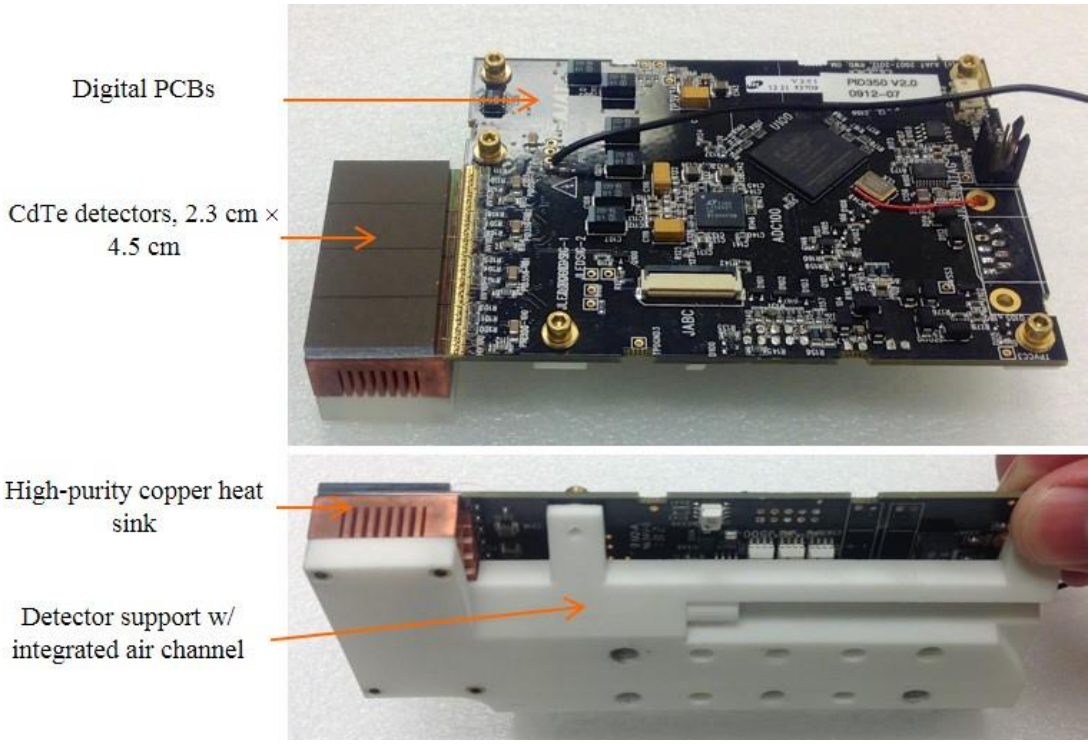

Fig. 3.2. The Gen-II ERPC detector module used for MRC-SPECT

The Gen-II ERPC detector has similar spectroscopic performance as that of the first generation detectors. The energy resolution of the 2mm thickness detector is about 5-6keV at 140keV. Figure 3.3 is a sample spectrum acquired in single pixel irradiated by Co-57. The x-axis is the energy and the y-axis is the counts. The 122keV and 136keV peak are clearly separated. The information of these two peaks can be used to calculate the gain and offset of individual pixels, which is called the energy calibration. The Figure 3.4 below represents the pixel gain value map of all the ten detectors (detector 1-10 from left to right) used in the system we built. It can be seen that the detector system has remarkably uniform performance. The top picture is the gain across the whole system and the bottom two pictures represent the gain map of two individual detectors. The number of the dead pixel of the whole system (81920 pixels in total for ten detectors) is less than 0.1%, which is better than the first generation ERPC detector.

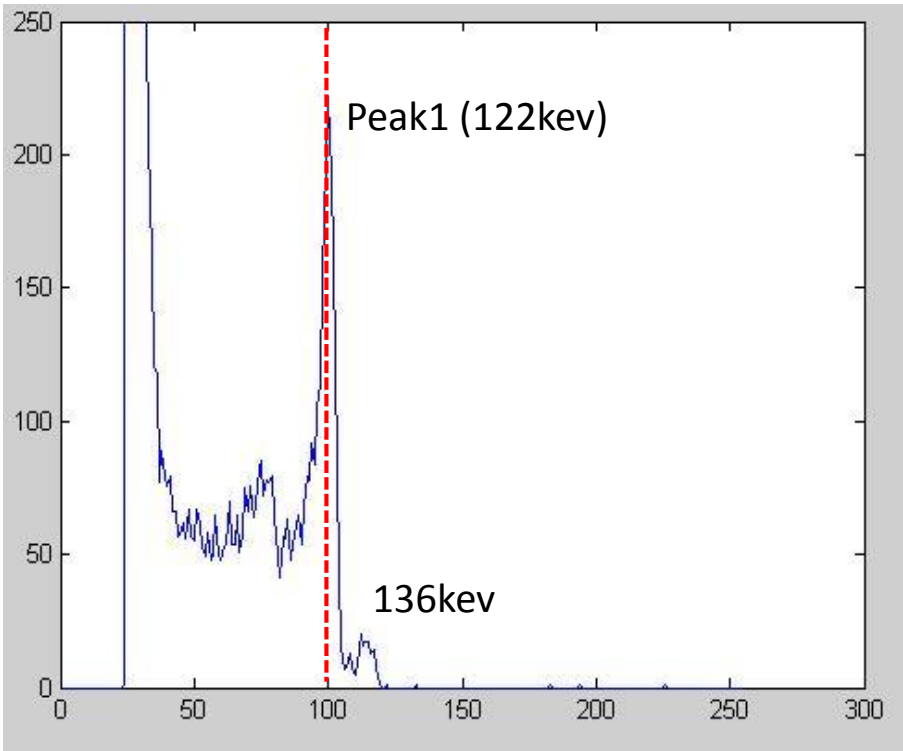

Figure 3.3 Sample spectrum at individual pixels (the picture at the bottom represent spectra randomly picked in 100 pixel of detector 5)

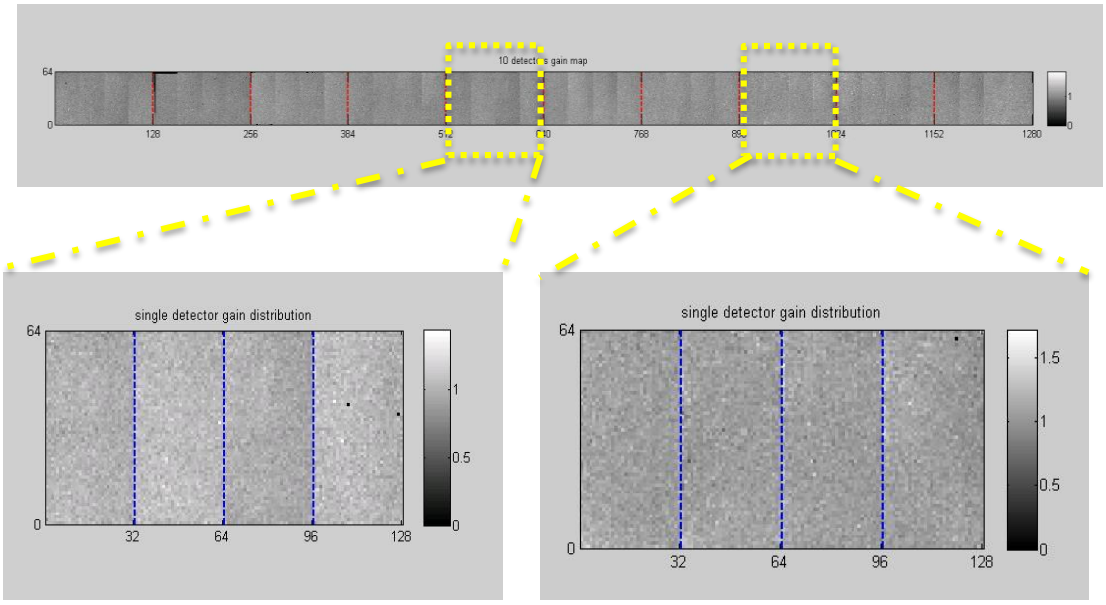

Fig. 3.4 The pixel gain distribution map of all the 10 ERPC detectors

3.1.2 System Design

This ultrahigh resolution MR compatible SPECT system consists of ten second-generation ERPC detectors assembled as a compact ring. The SPECT system is installed on a non-metal gantry constructed with 3-D printing using nylon powder. This technique is highly flexible and allows us to integrate air pipes for detector cooling and channels for electrical wiring into a single-piece construction. Figure 3.5 is the system design drawing which contains the detector rings, system housing, pinhole aperture, system control electronics PCB board, front and rear cover, etc. A single detector ring consists of ten detectors. The distance between the opposite detectors is 15.6cm and the detection area of each detector is 22.5mm × 45mm. Each detector has four 300 or 500μm pinholes and the object to pinhole distance is designed to be around 36mm. The field of view of the ten detector system is about 18-20 mm diameter in trans-axial direction and 20mm in axial direction. The geometry sensitivity is around 0.02% when using 300μm pinholes. And it can achieve up to around 0.07% when using 500μm pinhole aperture. The imaging object can be transmitted into the cylindrical lead aperture tube from the front side under control of precise linear motors. Based on this system, another ten detectors can also be

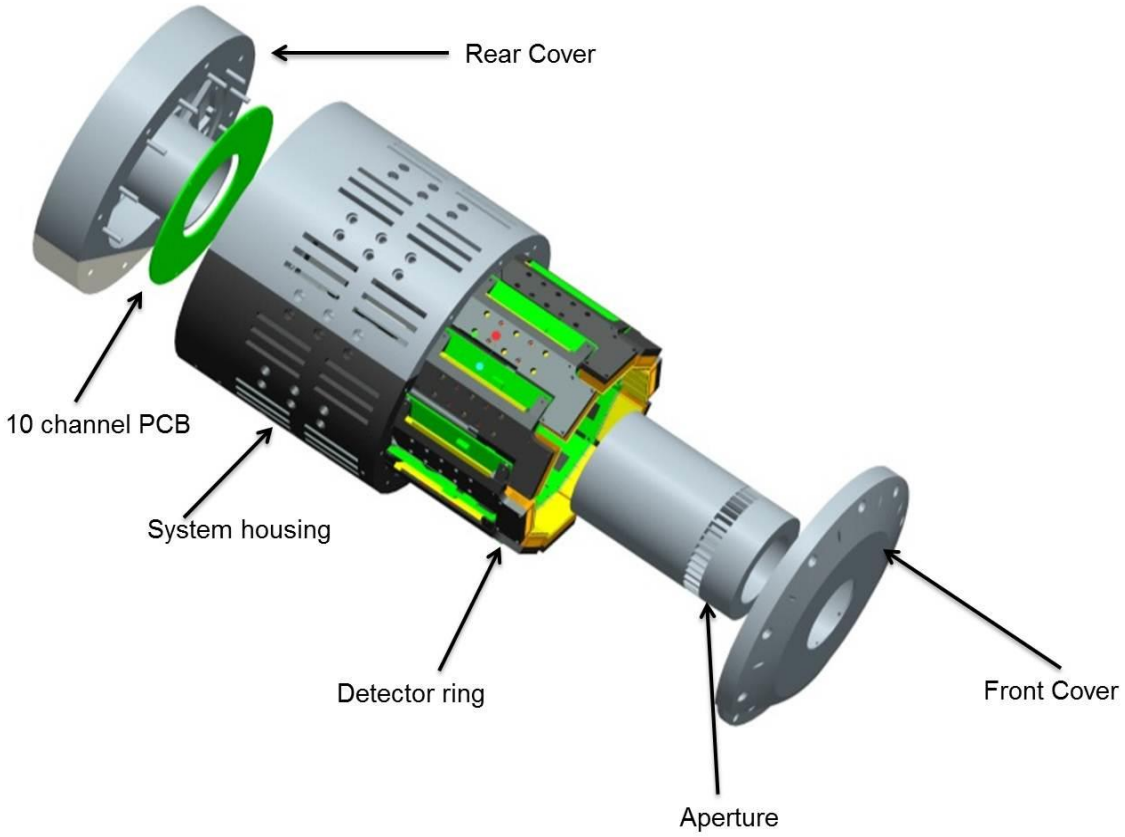

Fig. 3.5. MRC-SPECT system design drawing

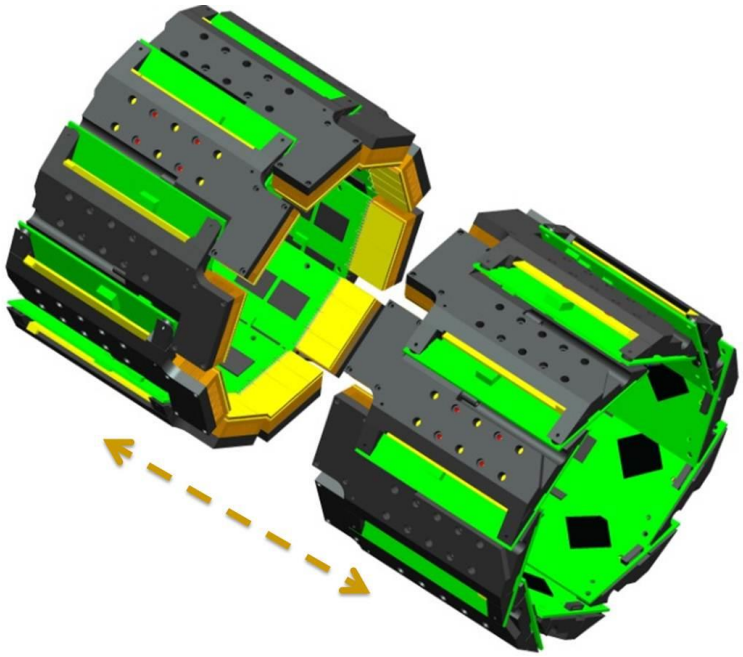

Fig. 3.6. Two 10-detector rings can be put together to deliver a 20-detector system

assembled and a full ring (which means each head has a square detection area of 45mm × 45mm) can be constructed by packing 20 detectors together in future works (Figure 3.6). The 20-detector system will have larger field of view, large sensitivity, and more sufficient angular sampling.

In order to control the operation of the 10 ERPC detector modules, a central control unit is developed as shown in Figure 3.7. The designed 4-layer PCB provides 12 regulated power supply channels and 12 independent data channels for sending the digital data acquired by the detectors to a host PC. In particular, two sets of low voltage (+5V/+3.4V) are used to provide power for the detector readout PCB board analog and digital part. For each individual detector, the steady current for the analog signal (+5V) is around 1.60-1.95A and for the digital signal (+3.4V) is around 0.16~0.19A. So the total current through the PCB board is around 20A. The high voltage bias applied at the detector is 350V. (-350V is applied on the cathode.) The command and data transfer of individual detector is developed under SPI protocol. External Cheetah SPI to USB adapter (developed by Total phase, Inc.) is used within each ERPC detector to communicate with host PC through USB 2.0 port.

There are several important issues that need to be addressed when designing and fabricating the PCB. First, we left necessary redundancy when designing the PCB board, especially based on the high current concern (total current in PCB up to 30A). Second, a specially designed anti cross-talk circuit is embedded on the PCB to prevent undesired signals from disturbing different channels. This is mainly based on extra inductance and capacitance circuit of each channel. Third, in order to protect the detection system from accident damage (for example, high current caused short circuiting), necessary fuses are used in each channel in the PCB. All the cables connecting the detectors and the PCB are well secured to provide reliable power feed. And proper voltages should be set to keep the system working properly. The voltage drop in the cable can not be omitted since the total flow current is pretty high.

Currently, there are two readout modes designed for the MRC-SPECT system. The first one is the “RAM” mode. In this mode, the spectrum of each pixel will be stored during the data acquisition time. The gain and offset of each pixel can be calculated and stored as a

reference map in the energy calibration step. Then they can be used to help generate projections for each image acquisition point. In comparison, the other readout mode is the live-data mode. In this mode, acquired data will be recorded frame by frame. Each frame represents the energy deposition at individual pixels. The live data mode records all the information including comprehensive charge sharing information between adjacent pixels. The speed of reading out the full frame data can achieve up to 20 fps. We can also modify the detector firmware to only read out the pixels we are interested at. For example, in SPECT applications, because of the existence of the collimator, only very few pixels will be hit by the incoming gamma rays and then register events in each frame. By establishing proper threshold for each pixel, we can potentially only select specific pixels and read out the energy deposition and position information of the particular pixels. The live mode readout system is capable of reading out up to 1000 frames per second, which allows for a dynamic data acquisition with relatively accurate time stamp.

Figure 3.7 shows two important accessary components of the system, the rear cover and the system PCB we just discussed above. The power and high voltage supply, communication and data transfer cables, and air cooling facilities will come through the rear cover neatly. The rear cover also serves to protect the cables from too rigid bending. Ten custom-made Lemo-to-USB cables are made to connect from the central PCB data communication ports to the USB ports in host PC. The high voltage (HV), low voltage (LV), and data acquisition (DAQ) connectors are located at the front side of the PCB. Twelve independent channels are evenly distributed at the back side of the PCB, connecting individually to the ten detectors of the system. Thanks to the 3D printing technology, a cavity is designed inside the rear cover, which helps to provide uniform and continuous airflow for ten air channels as shown in Figure 3.7. The whole system can be stationary, operated on a laboratory bench working as an ultrahigh resolution SPECT microscope. It is also portable since the system is very compact, based on which assembling this system inside a pre-existing MR scanner is relatively straightforward. All the detector components, pinhole apertures, as well as other external parts are constructed with a minimum amount of magnetic materials to ensure system MR compatibility.

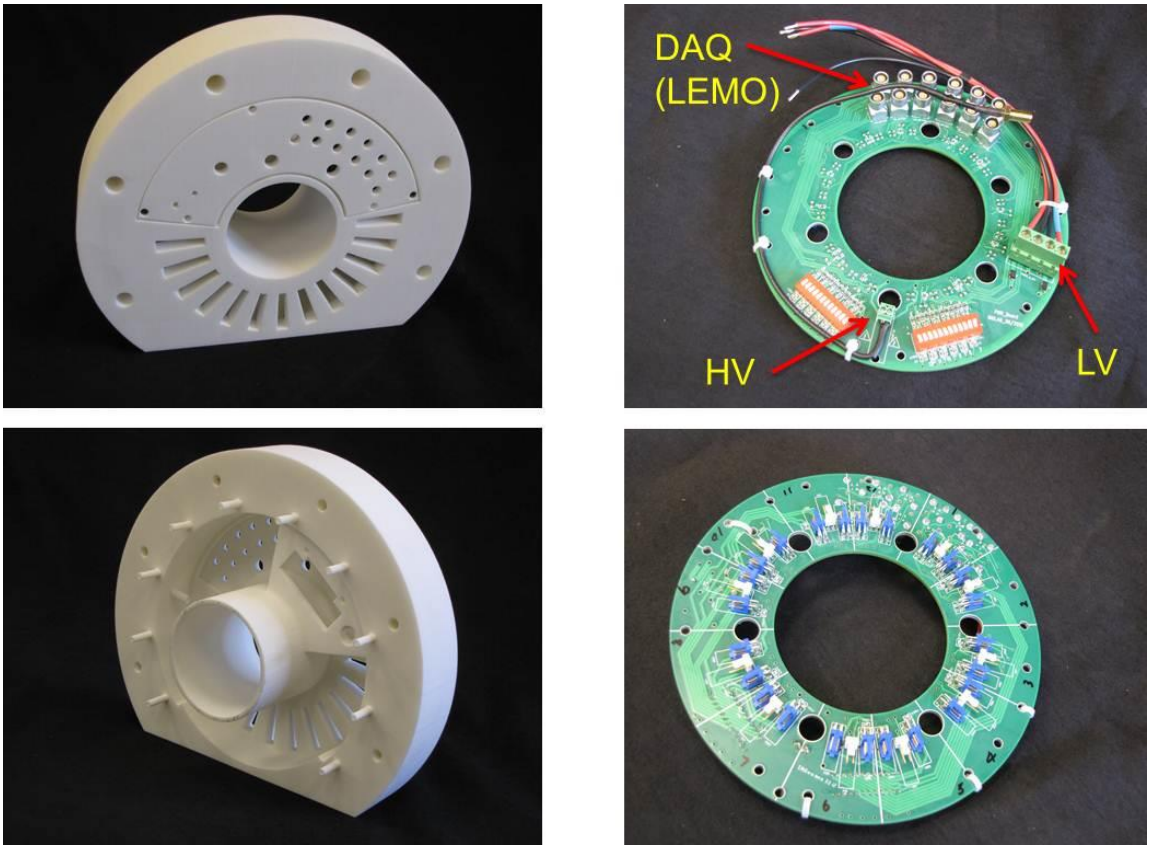

Fig. 3.7. System rear cover and 12 channel electronics PCB board

3.2 Aperture Design and Fabrication

In order to achieve sub-500um imaging resolution, we have constructed two SPECT apertures, with different pinhole sizes of 300μm and 500μm respectively. The inner diameter of the lead tube is 66mm and the tube thickness is 16mm. It has pinhole inserts that are made of cast platinum (90%)-iridium (10%) alloy, which provides the maximum stopping power and are compatible with MR scanners. The opposite detectors are placed 15.6cm apart and the magnification factor of this SPECT system is around 1.2. A total of 40 pinholes will be used in the 10 detector ring system and the sensitivity can achieve up to 0.07%. In particular, four 300 or 500μm diameter pinholes are used for each detector and all pinholes are inserted in the cylindrical lead aperture tube as a ring. The pinhole open angle is 50 degree and the height is 6mm. As shown in the Figure 3.8, the aperture is specifically designed to prevent severe pinhole projections. The design rule is that

projections through each pinhole will be constrained in two neighboring detector hybrids. The Figure 3.8 shows the cross section of the designed collimator. The trapezoid shape lead wall on top of each pinhole is used to restrict projection through each pinhole within two adjacent detector hybrids as shown in Figure 3.9. A sample phantom projection is attached as Figure 3.10. The boundary caused by the lead wall can be roughly seen. The designed field of view of this system is about Ø20mm ×20mm.

In future studies, apertures of smaller or larger inner diameter can also be investigated for different imaging applications. The collimators with larger inner diameter tends to have larger field of view, which can be used to carry out rat imaging studies. A collimator like this (inner diameter 82mm) is currently under fabrication process. On the contrary, collimators with smaller inner diameter can also be evaluated. They have a larger magnification factor and potentially higher spatial resolution can be achieved.

To calculate precise system response function, we have previously developed a mathematical model to mimic the pinhole aperture as multiple layers of thin sheets as described in last chapter. A comprehensive geometry calibration routine has been applied to derive accurate geometry information. In particular, a Co-57 point source is used to scan the object space. The experimental point source projections acquired with ten detectors are used for geometry calibration. To deliver simultaneous MR and SPECT imaging, a birdcage RF coil can be transmitted into the lead aperture tube and the source object will be place inside the RF coil.

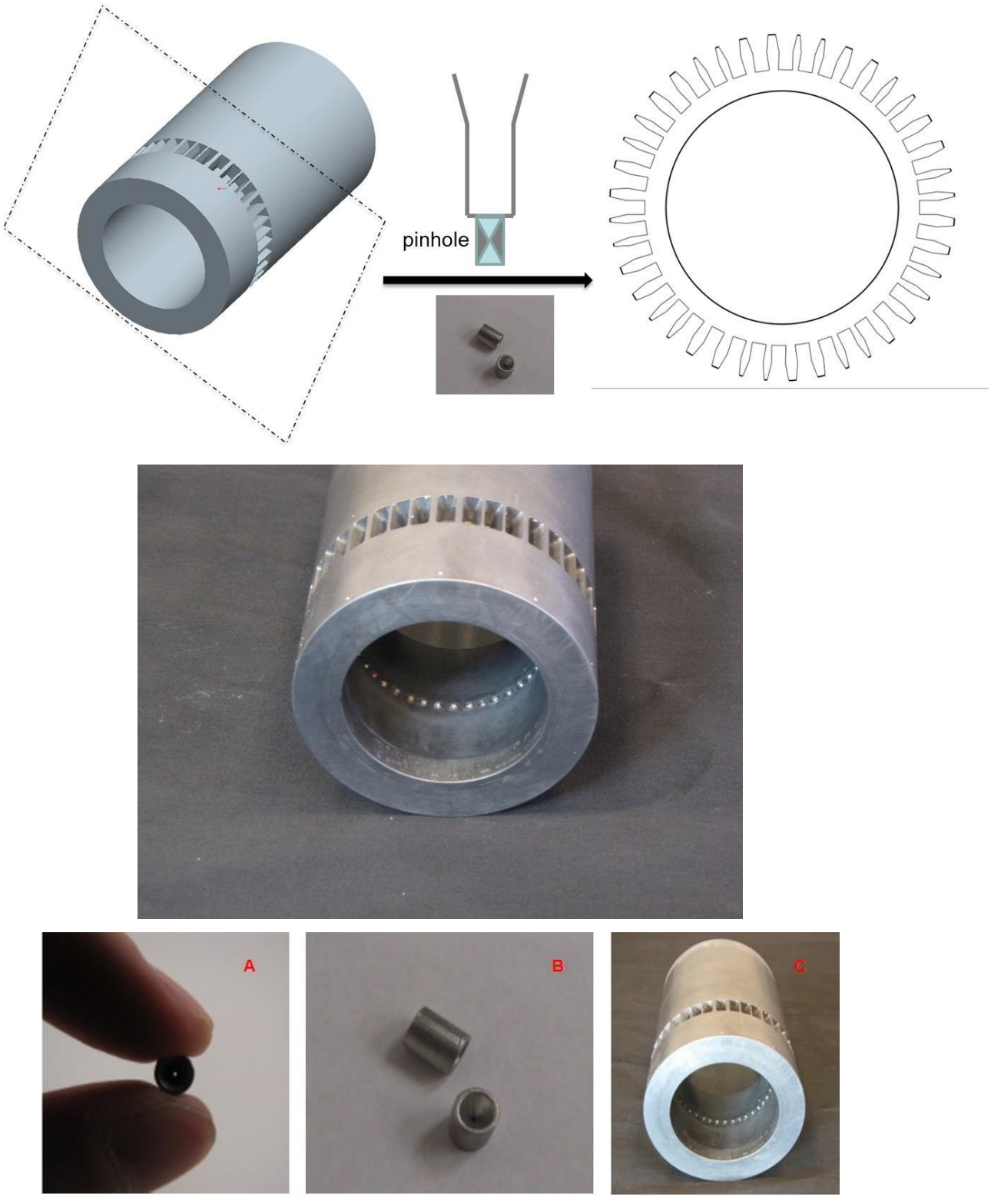

Fig. 3.8. Pinhole aperture for MRC-SPECT (up: cross section of the lead collimator; middle and low: The casted Pt pinhole insert and aperture)

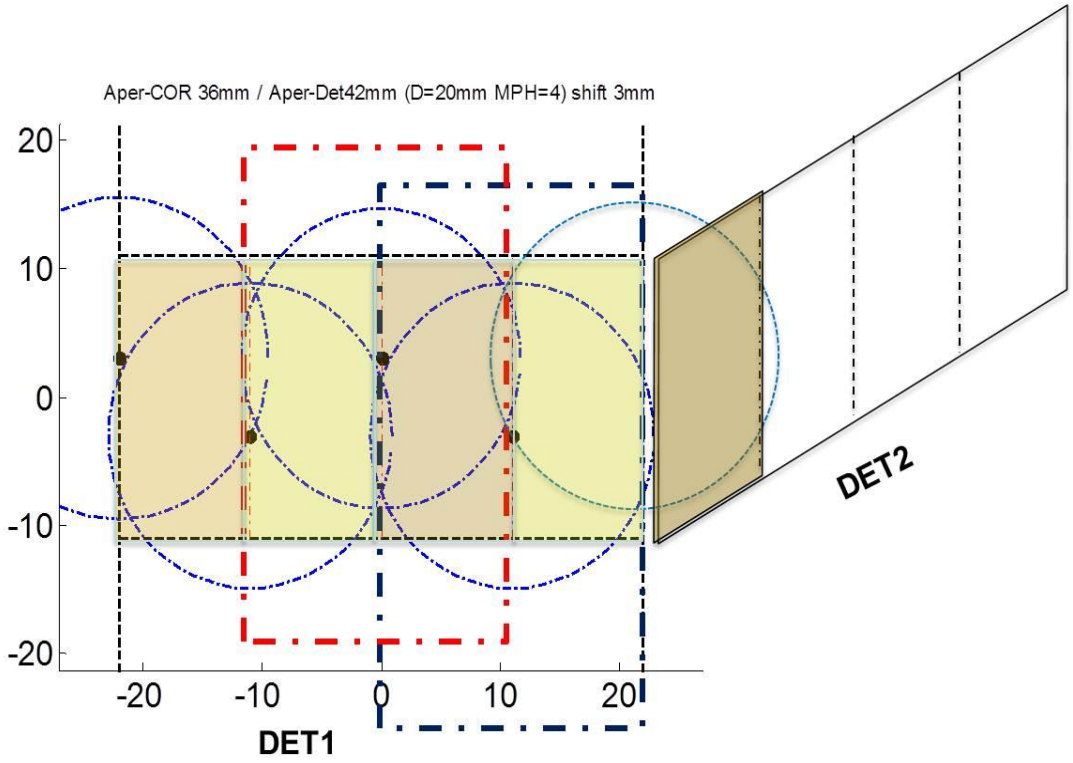

Fig. 3.9. The designed projections in two adjacent detectors, round dash lines represent projection margins of a 20mm diameter spherical object

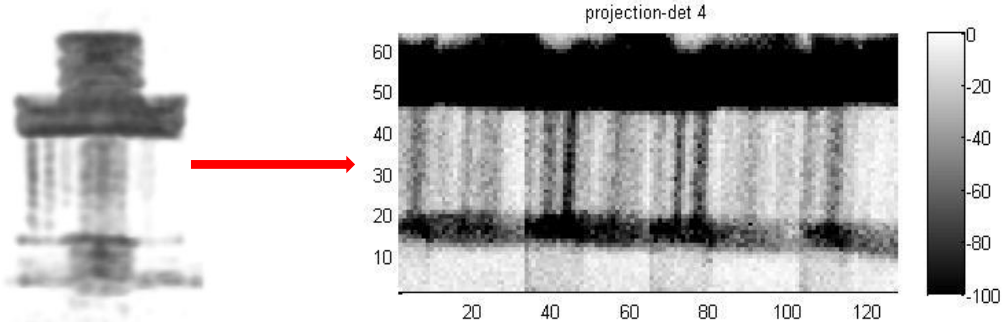

Figure 3.10. A sample phantom projection in one detector, the phantom total size is around Ø16mm ×30mm filled with Tc-99m

3.3 MRC-SPECT System

Figure 3.11 shows the assembled fully-working MRC-SPECT system. Ten detectors are closely packing around the system housing. The generation II ERPC detector has the detection area at the upper-left corner. So there exists a small gap between neighboring detectors, and the detector ring is not a normal decagon. Because of this, the 40 pinholes around the designed aperture are not evenly distributed. The system can be operated on a laboratory bench as an ultrahigh resolution stationary SPECT microscope. This compact system can also be operated inside a pre-existing MR scanner. When operating outside the MR scanner, a carbon-fiber made animal holder is mounted on precise 3-D motors ((Newport MFA-CC)) to transport the imaging object. In contrary, a PVC and plastic made animal holder is used when using the system inside the MR. The system housing outer diameter is 248mm and the MR bore diameter is 350mm (for a Siemens 3T Allegra Scanner). It is worth pointing out that all the ten detectors have remarkable uniformity performance as we already discussed. The dead-pixel number from the gain distribution throughout the ten detectors is below 0.05%. The energy resolution for individual pixels is about 4-6keV. The system parameters are in table 3.1 below.

Geometry parameters	**Parameter Values**
Object-to-aperture distance	~36 mm
Aperture-to-detector distance	~42mm
No.of pinhole/Aperture.	40
Pinhole size	Ø300μm / Ø500μm
Pinhole accept angle	50°
Number of Detectors	10 (up to 20, stationary)
Detector size	4.4cm × 2.2cm
Detector thickness	2mm
Sensitivity	0.025%/0.07%
FOV	~Ø2cm × 2.2cm
Expected image. resolution	<500μm

Table 3.1 MRC-SPECT parameters

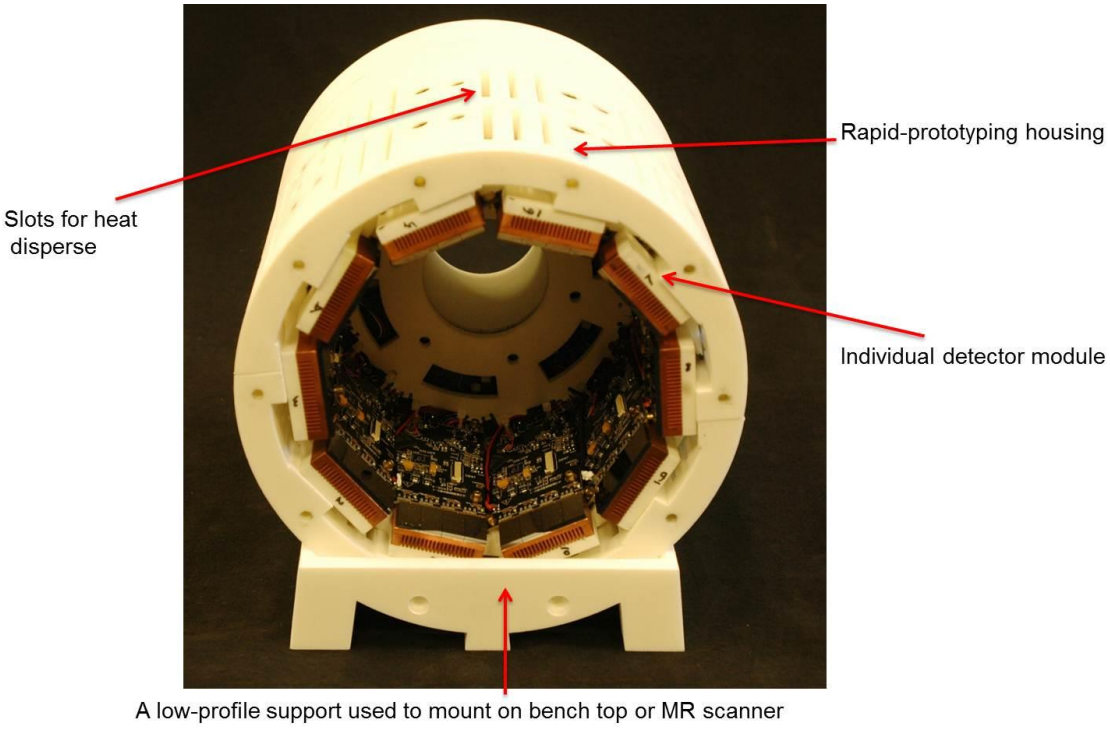

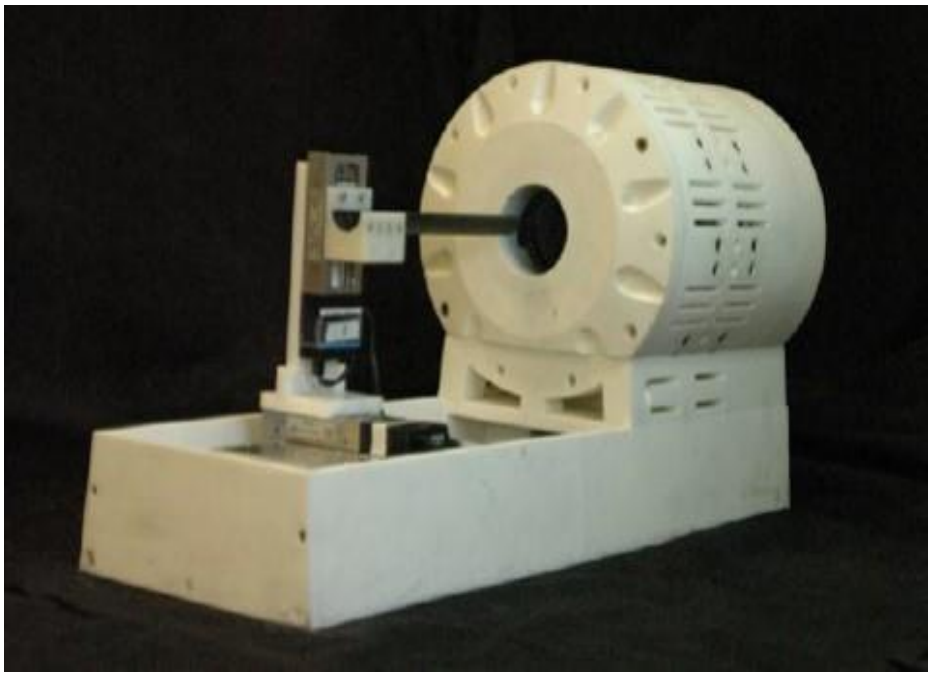

Fig. 3.11. The assembled MR compatible SPECT system (up: the detector ring assembled without aperture; down: ultrahigh resolution SPECT microscope)

3.4 System Control and User Interface

As a relatively complex imaging system, it is important to develop robust and smooth system control software and friendly user interface. The system control, operation, and data processing can be mainly divided to the following three parts.

The first part is the detectors communication. The ERPC detector control is based on SPI protocol. A 4 or 12 bit command will be sent to the detector for various detector operation requests. A comprehensive Labview package was developed to communicate with the multi-head system. Both the RAM mode and live-data mode data acquisition routines was implemented. In the RAM data mode, the spectra of individual pixels of each detector are saved in on-board RAM during the data acquisition. The data saved in RAM will be read out when acquisition is finished. With tremendous effort spent on multi-thread based Labview programming, the readout speed for the ten detectors' data can achieve ~13s for ten detectors simultaneously operation, which hits the intrinsic limitation defined by the detector clock (4MHz). For the live-data mode, the frame-by-frame data will be read out at the rate of ~20fps. The energy deposited in each pixel will be saved and readout. Further photon-counting data processing routine is needed to get the list mode data.

The second part is system hardware control. A 3D accurate stepper motor scan routine is developed for MRC-SPECT system shown in Fig. 3.11. With the 3D scan option, a Co-57 point source can be used to scan the field of view to calibrate the system geometrical information. The motors are also used for accurate animal bed translation.

The last part is the data processing. In the RAM mode, individual pixel spectra are collected for each detector. With the pre-calculated pixel gain and offset and proper energy window centered at the photon-peak, we can get projections for each detector for further geometry calibration or image reconstruction. In the live-data mode, the post-processed list mode data can be achieved by processing the raw frame-by-frame data. The further data processing procedure is similar for the two readout modes.

The currently developed user interface can be divided into three pieces: initialization, image preview, and data acquisition.

System Initialization

In the initialization part, the communication between host computer and the ten detectors is established. The serial number of cheetah SPI-USB host adapter is needed to distinguish connection of individual detectors. As long as the serial numbers provided, the user does not need to assign a specific USB port for a particular detector. In practice, the pre-known serial numbers can be set as default values, then the user does not need to worry about

Fig. 3.12. The initialization step

the multiple detector system connection problem. As shown in Fig. 3.11 below, the "*Port Initialize*" operation establishes all the connections. And "*Detector Initialize*" is used to load proper gain and offset for each detector. All the orange lights will turn green after successful initialization process.

Preview

The second section is the preview step. In this part, the target object can be translated under the control of 3D motors. The preview image can be used to guide the position of

Fig. 3.13. The preview step

the object into the center of field of view. The preview time and specific energy window can also be set based on different applications. Figure 3.12 represents the preview page and the three white spots at each detector represents Co-57 point source projection preview. It can be seen that the point source is obviously located off center in this example.

Data Acquisition

In the data acquisition part, both point source scanning in object space procedure (for system geometry calibration) and phantom/small animal imaging procedure can be carried

out. A general Co-57 point source based 3D scan scheme is used to calibrate the system geometry information. Besides a simple 3D scan routine, the user can also define random positions for either point source scan or phantom/imaging study.

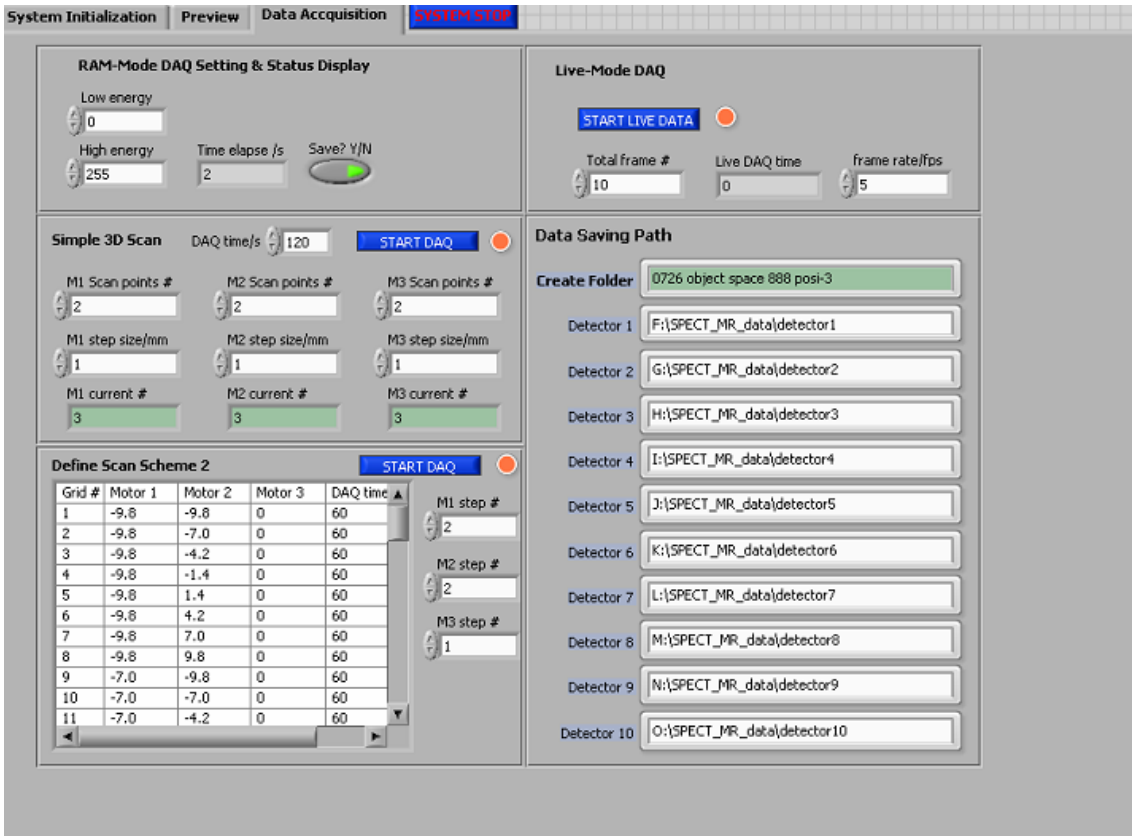

Fig. 3.14. The data acquisition step

CHAPTER 4

MRC-SPECT System Evaluation and Imaging Study

In chapter 3, the development of a stationary MR compatible SPECT system based on ten Generation-II ERPC detectors has been discussed. In this chapter, the detailed system performance, including energy and uniformity calibration, accurate geometry calibration, system response function calculation and corresponding phantom imaging studies will be discussted. Figure 4.1 below (central column) is the working flow chart of this system. The left column is corresponding control and data processing and the right column represents the results come from individual steps.

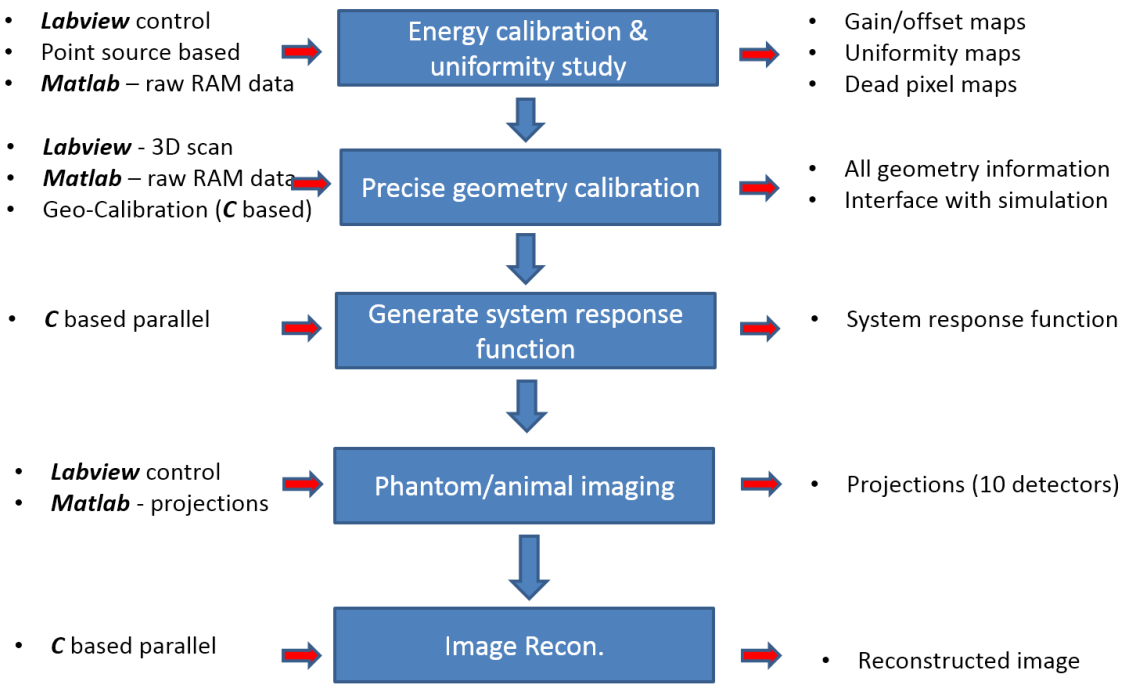

Fig. 4.1. DAQ and data processing flow chart of MRC-SPECT

4.1 Energy and Uniformity Calibration

The MRC-SPECT system has ten detectors and 81920 pixels in total. In Chapter 3, we have demonstrated that the ERPC detector has remarkable uniformity in terms of the gain value of individual pixels. As an imaging system, it is of great importance to verify the detection uniformity across the system. The uniformity difference needs to be compensated on the collected projection data. The Fig. 4.2 is the setup for the energy and uniformity calibration. In this experiment scheme, the lead aperture is temporally removed at first. A Co-57 point source is used to irradiate the ten detectors at the center of the field of view. The raw spectrum of each pixel will be recorded as Fig 4.3 (top). The 122keV and 136keV peak can be used to calculate the gain and offset of individual pixels. The raw spectrum can be re-aligned as Fig 4.1 (bottom) based on the pixel gain and offset value. A proper

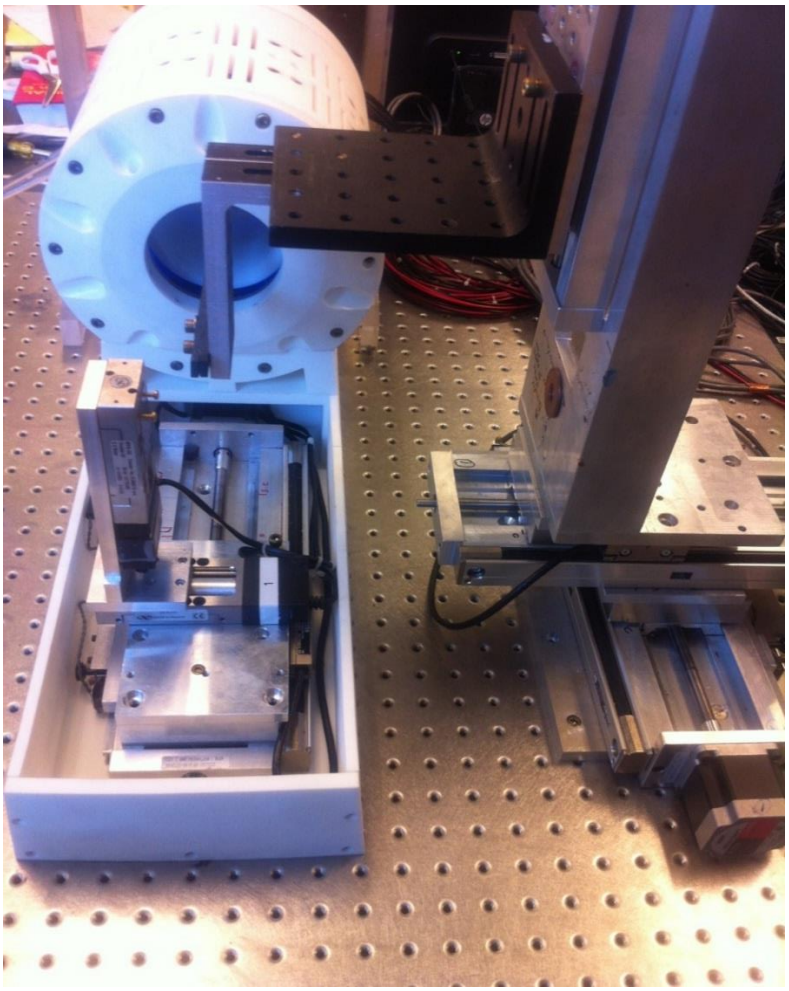

Fig. 4.2. The setup for energy and uniformity calibration

energy window can then be defined to calculate the number of interaction events within the defined energy window (quantum efficiency not considered here). The numbers recorded at all these 81920 pixels (10 detectors) will be used to calculate the detection uniformity across the whole system. In this MRC-SPECT system, the distance between the point source and individual detectors is around 80mm, which is not sufficiently far to ignore the geometry-caused pixel detection variation. So it is necessary to know the exact position of the irradiating point source and the geometry information of this system. In that case, the distance between the point source and individual detector pixels can be calculated to compensate for the geometry-caused pixel detection variation. So the second experiment step is necessary to achieve geometry information: after data acquisition with point source roughly at the center for a period of time (sufficient long for enough counts), the pinhole aperture needed to be assembled to calibrate for the geometry information. The 3D Velmex motors are used to move the point source back and forth between the first and the second step. The point source was kept at the same position during the two steps, which are flood source experiment and the geometry calibration afterwards, respectively. More detail on geometry calibration is discussed in Section 4.2.

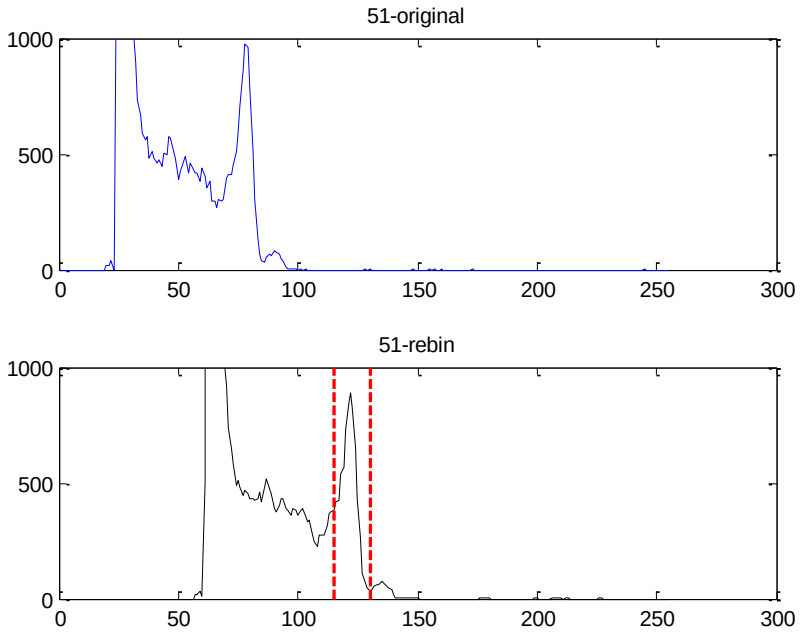

Fig. 4.3. The raw (top) and re-aligned (bottom) spectrum

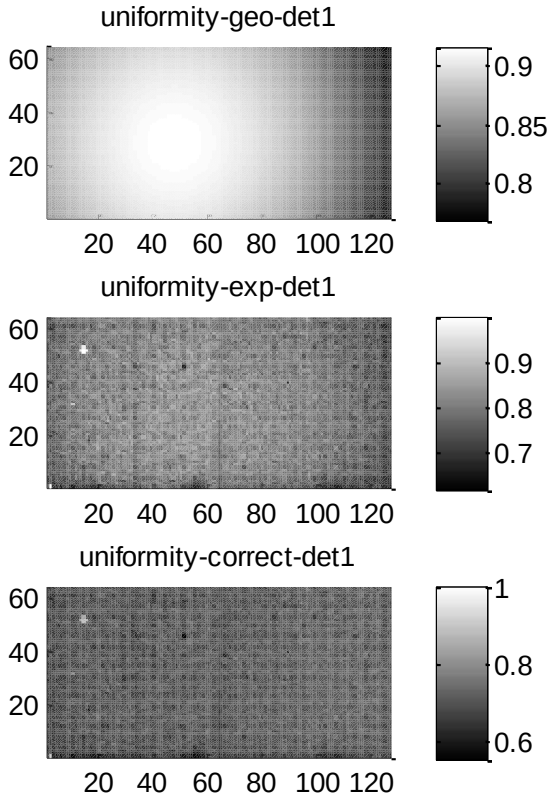

Fig. 4.4. The generated uniformity map

Fig. 4.4 demonstrates the uniformity derivation for a single detector. The figure on the top represents the normalized compensation factor based on geometrical information. It is clearly seen that the pixels at the boundary have less probability to record the isotropic emitted gamma rays than the ones in the center. In the middle and bottom figures, the x and y axis represent the detector pixel number. The normalized grey scale represents the detection uniformity. The middle figure is the normalized raw recorded counts distributed in single detector (in defined energy window). After applying the compensation factor (top) to the normalized raw detected counts (middle), we can get the uniformity map as shown at the bottom of Fig. 4.4.

$$corrected\ uniformity = \frac{raw\ uniformity\ calculated}{geometry\ compensation\ factor}$$

It can be seen that the detector has very good uniformity, which means that different pixels have similar event detection capability.

4.2 Accurate Geometry Calibration for MRC-SPECT

The precise geometry calibration is one of the key factors for high resolution reconstruction. Generally, the task of the geometry calibration is to find the system geometry parameters as precise as possible. The way to do this is to establish a projector model. In this model, all existed system geometry parameters are included. In a geometry calibration scheme, the experimentally acquired "projections" are used to compare with the "projections" generated based on defined system model we just described. The procedure of finding the good match of these two sets of projections leads to the derivation of all the defined parameters in the system model. This system model can be written as the following equation.

$$Proj(model) = f(p1, p2, p3, \dots)$$

Where *f* is the system model to form the projection and *pn* is system geometry parameters. The geometry calibration scheme is to find the best match of experimental and modeled projections, which can be written as:

$$argmin \sum \{Proj(model) - Proj(experimental)\}$$

A comprehensive geometry calibration method has been developed for a prototype dual/four head system as discussed in Chapter 2. In MRC-SPECT, we will apply the similar algorithm and programming structure. However, due to the complexity of the ten head multiple pinhole system, several specific issues need to be addressed carefully in MRC-SPECT geometry calibration, which will be described in the following contents.

Fig. 4.5 represents the basic geometry of the MRC-SPECT system. The ten detectors are packed around the aperture that has 40 pinholes in total. The detailed system construction has been discussed in the previous chapter. In the geometry calibration procedure, the key is to get precise position and orientation information of the detectors and the pinholes. The axial cross section of the system is demonstrated as Fig 4.5 (right). In order to interpret all the geometrical information of whatever components in the system, it is important to define a proper coordinate first. In MRC-SPECT, we define the Z-axis to be perpendicular to the system horizontal surface. The X-axis is defined to be parallel with the horizontal surface (pointing out "along" the system axial direction). The Y-axis can then be defined

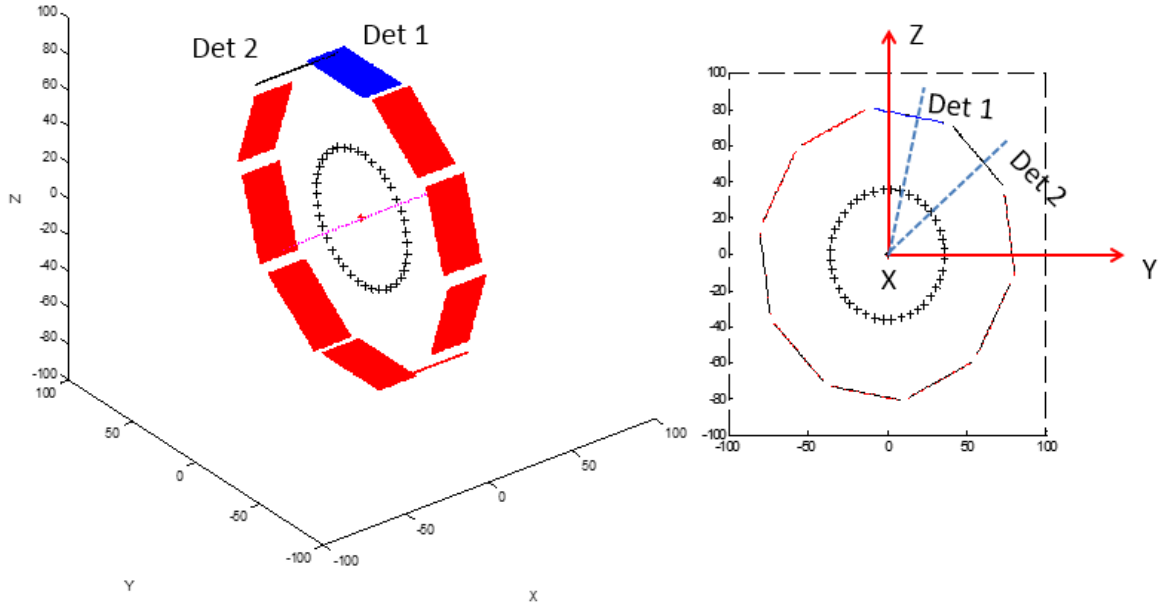

Fig. 4.5. MRC-SPECT system representation

under the right hand rule. Under this coordinate system, we can define the positions and orientations of all these detectors, pinholes, and so on. For example, 6 parameters are used to define each detector position and orientation. Euler angles based on a rotation matrix are introduced to define the orientation. Since each detector consists of four CdTe detector hybrids, the gaps between neighboring hybrids are also taken into account in the system model. Fig. 4.6 lists the parameters defining the system geometrical information. A total of 390 parameters are used and 269 of them are open parameters which need to be fit during the geometry calibration process.

A precise penetration map is generated for the pinhole insert to calculate the accurate system response functions. As Chapter 3 mentioned, the 40 pinholes are not uniformly distributed around the lead cylinder and specific features have been designed to prevent severe overlapping of projections. The trapezoid-shape slots as well as the embedded platinum pinholes were mathematically modeled to generate the penetration map.

The geometry calibration is implemented by scanning a Co-57 point source under the control of accurate linear motors. The projections of ten detectors at each scanning position is recorded to calibrate for the geometrical information.

Parameter definition	index	parameter to fit
Detector geometry definition	1-60	60
ASIC gap definition	61-140	80
Scan point source origin	142-143	2
3D scan orientation	144-149	6
Detector1 rotate angle	150	1
Pinhole geometry definition	151-390	120

Fig. 4.6. A list of system parameters for geometry calibration

The Fig. 4.7 is very helpful in understanding the point source projection process in geometry calibration. For each detector, there are a maximum of five pinholes which can contribute to projections on it. Projections through the center three pinholes will always be located at the detector (blue 'smiley' face), while projections through the other two pinholes (red 'sad' face) will tend to distribute to the two neighboring detectors, depending on the point source position. The scanning point source at different positions will generate distinct projections with different patterns. Fig. 4.8 shows five different projection types. For example, in type 1, only projections through the center three pinholes can be seen in the corresponding detector. In type 2, projections through the center three pinholes and through the left pinhole can both be detected. Different recorded projection types need to be recognized properly in order to carry out the right geometry calibration. Specifically, for each projection, we need to get the information of which pinhole the gamma-ray came through to generate the particular projection.

Fig. 4.9 below is a sample geometry calibration result. In this example, the point source is scanned at 5×5×3 positions. The step size is 3mm. Fig. 4.9 (left) is the comparison of the weighted centroid of the experimental projection and the weighted center of the modeled projection under calibrated system geometry. Similarly, Fig. 4.10 is the comparison

between the exponential projection profile and that get from the calibrated geometry. It can be seen that both of them have a good match, which demonstrate the accuracy of the geometry calibration process.

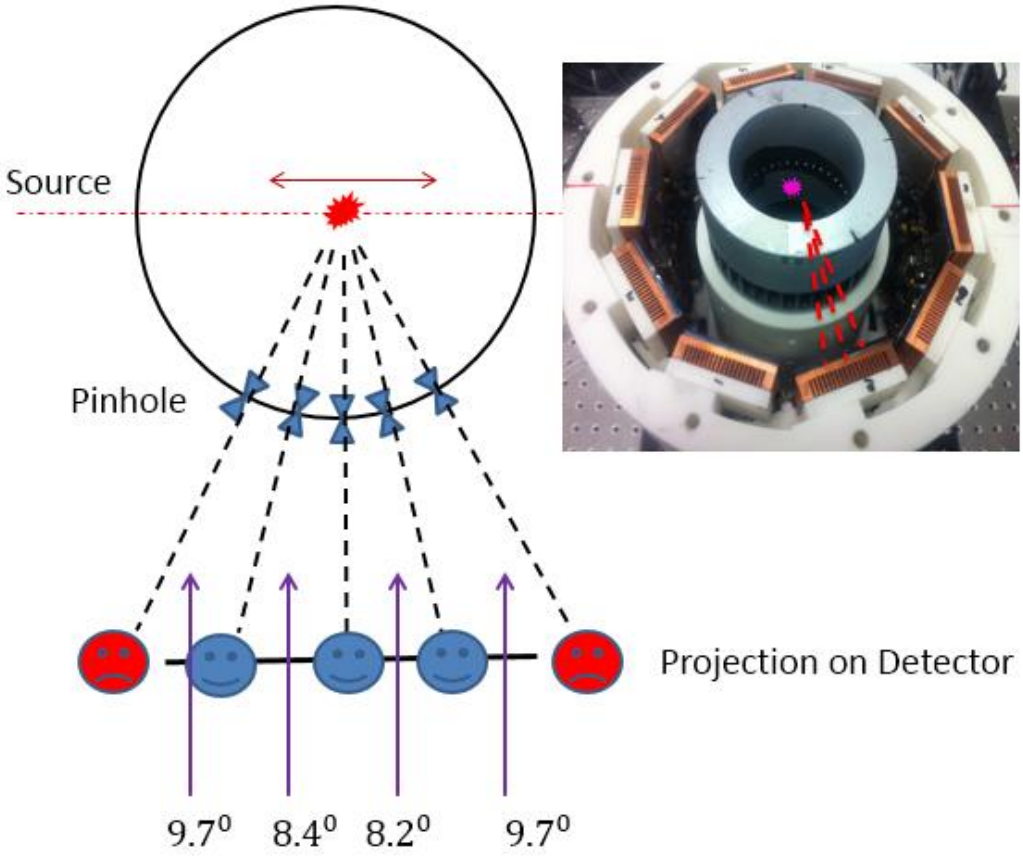

Fig. 4.7. Projection through pinholes at one detector

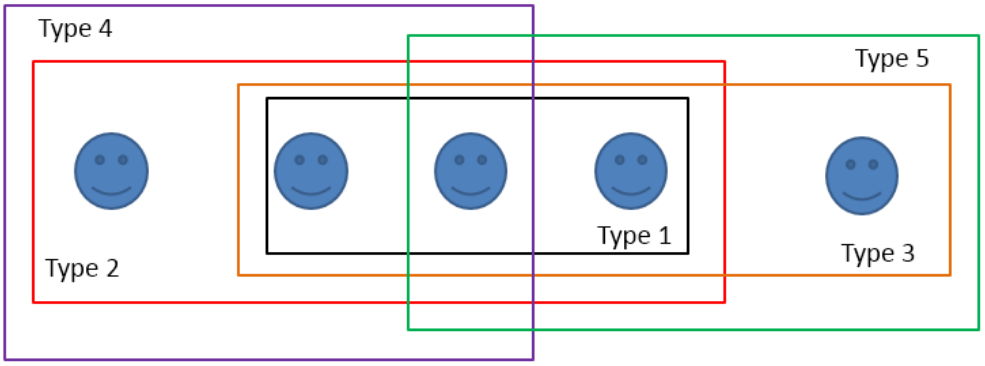

Fig. 4.8. Different projection types at one detector

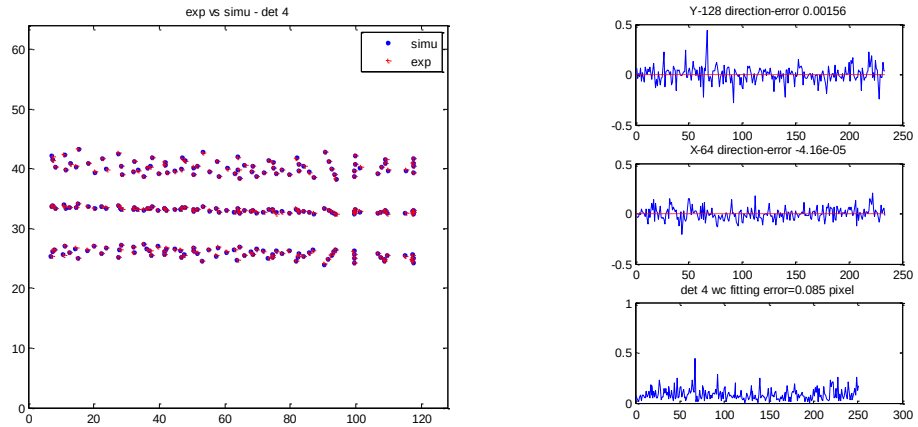

Fig. 4.9. Comparison of weighted center of experimental (left) and calibrated geometry-based simulated projection (right)

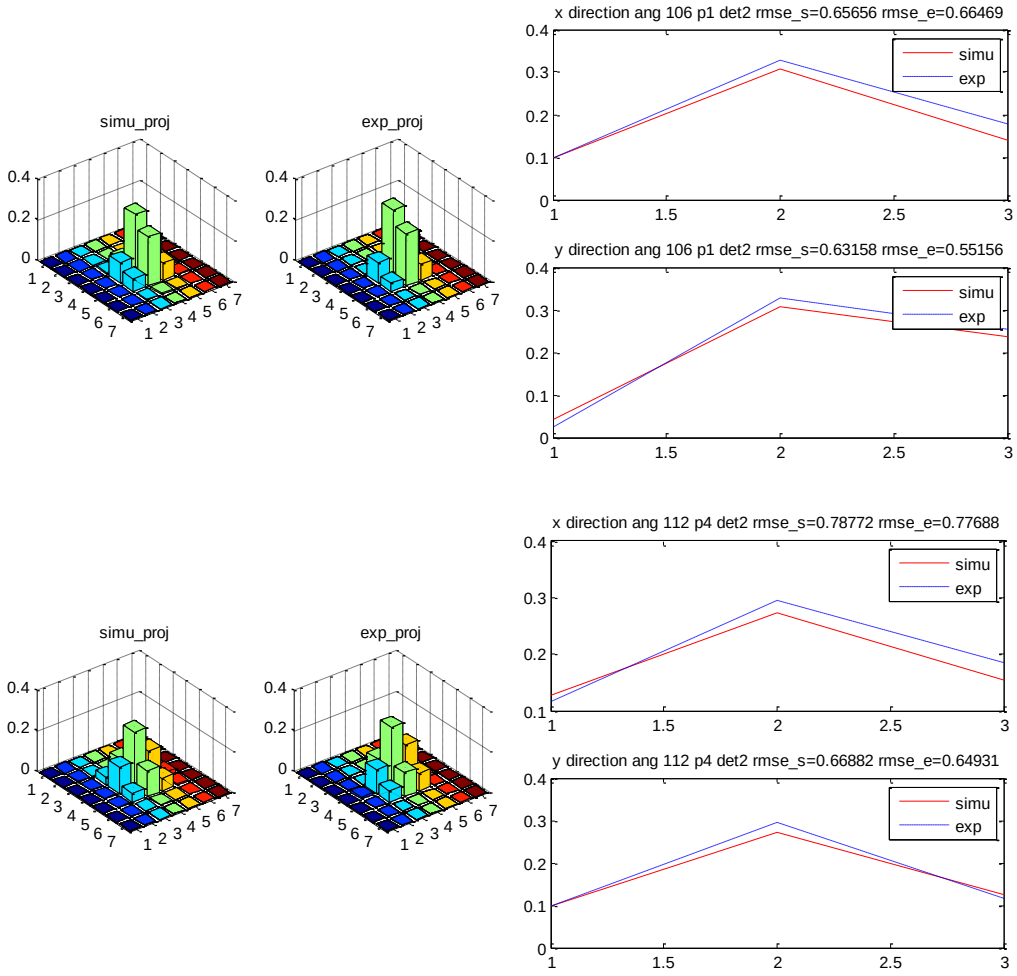

Fig. 4.10. Comparison of projection profile get from experiment and the geometry model

4.3 Precise System Response Function Derivation

System response function matrices present the individual probabilities of voxel *i* at object space being detected by the pixel *j* at detector space, denoted as A_{ij}. The imaging process can be written as $y = A \cdot x + noise$, where the y represents the projection and the x is the source activity distribution in the object space. They relate to each other by the system response function matrix. The system response function can be generated based on the calibrated geometry information. A comprehensive simulation package is used to calculate the system response function matrix, which plays an essential role in the image reconstruction.

To ensure precise system response functions, an experimental full object scan scheme is also introduced. In this scheme, we applied the experimental data to further improve the accuracy of the mathematical calculated system response function matrix. Here is an example case of this procedure. A Co-57 point source is used to scan a 9×9×9 (729) 3-D grid in the object space with a step size of 2.5mm. This scanning process will cover a 20×20×20mm object space. Projections at each scanning position are recorded. An experimentally-acquired system response function matrix (sensitivity) with values at the scanning positions can be achieved. Fig. 4.11 is the comparison between the normalized sensitivity obtained from the model and the experimental scanning projection. The X-axis represents the 729 points distributed at 9 axial steps. Positions with different axial positions are separate by the dashed lines. It is shown that they match each other relatively well in most positions, while obvious discrepancies can be found in some positions, especially in the scanning positions far off the center of field of view. The blue represents experimental data based sensitivity and the red represents the mathematical calculated sensitivity. Both have been normalized at same position. In this MRC-SPECT system, the specific designed aperture features and imperfect pinhole fabrication are two major reason for this phenomenon. The modeling of the trapezoid shape lead wall in the aperture is very tricky.

To compensate for this mismatch, the experimental data at the 3D grids is used to correct the mathematical calculated system response function based on geometry model. In particular, for each voxel in the object space, the neighboring experimental scanning points' projection information is used to correct for the local sensitivity calculation process.

Fig. 4.12 shows that the corrected sensitivity profile (green) matches the experimental data much better than the original directly-calculated sensitivity profile (red). Ideally, this scheme will produce system response functions which contain information more consistent with the experimental conditions.

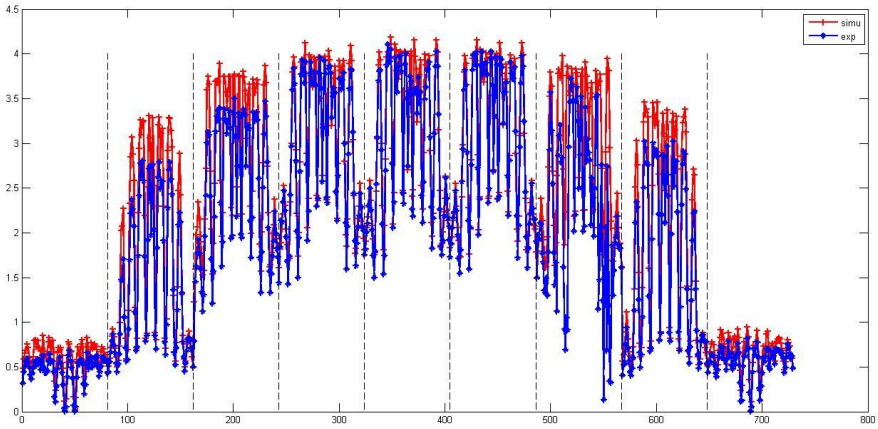

Fig. 4.11. The sensitivity profile comparison at the 3D scanning positions (experimental (blue) vs geometry model based (red) calculation)

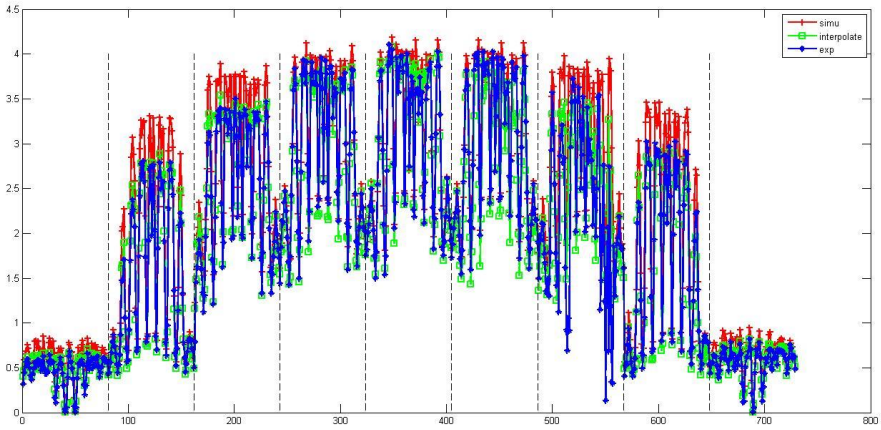

Fig. 4.12. The sensitivity profile comparison at the 3D scanning positions (experimental (blue) vs geometry model based calculation (red) vs correction applied version (green))

4.4 MRC-SPECT Imaging Studies

4.4.1 Imaging Study of Objects within FOV

The intrinsic spatial resolution of the MRC-SPECT system is first evaluated with a generated "point source phantom". Specifically, a 250μm diameter Co-57 point source is precisely controlled by the integrated 3D Newport MFA-CC linear stages. The point source can be accurately moved to the desired position and projections at corresponding positions are acquired. The point source phantom shown in Fig. 4.13 (left) was generated and the distance between neighboring point source (d) can be adjusted by changing the linear stage moving step size. The middle image is based on projections acquired with 500μm pinholes and the 500μm distance between neighboring point sources can be clearly seen. The point source phantom of 350μm spacing can also be clearly resolved with 300μm pinholes. The projections were acquired with 2 minutes at each position and the activity of the point source is around 70μCi.

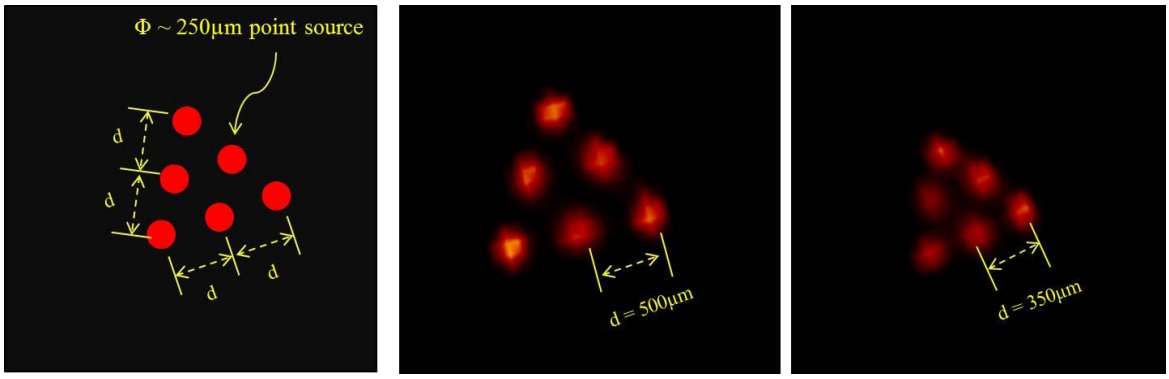

Fig. 4.13. The motor stage generated point source phantom and reconstructed image

A lab-made Jascszak phantom was also used to evaluate the preliminary imaging performance of the MRC-SPECT. The phantom size is about Ø16mm×25mm. There were four sets of hot rods with diameter of 1000μm, 750μm, 500μm, and 350μm. The phantom is filled with ~1μCi Tc-99m and the data acquisition time is 30 minutes. Fig. 4.14 is the projections in the detectors (bottom). It can be seen that there is very strong background at the top of the phantom. The real activity in the hot rods is actually significant smaller than 1μCi. A 20% energy window around 140keV is used to produce the projections. The image reconstruction was implemented with OSEM with Gaussian filter between iterations.

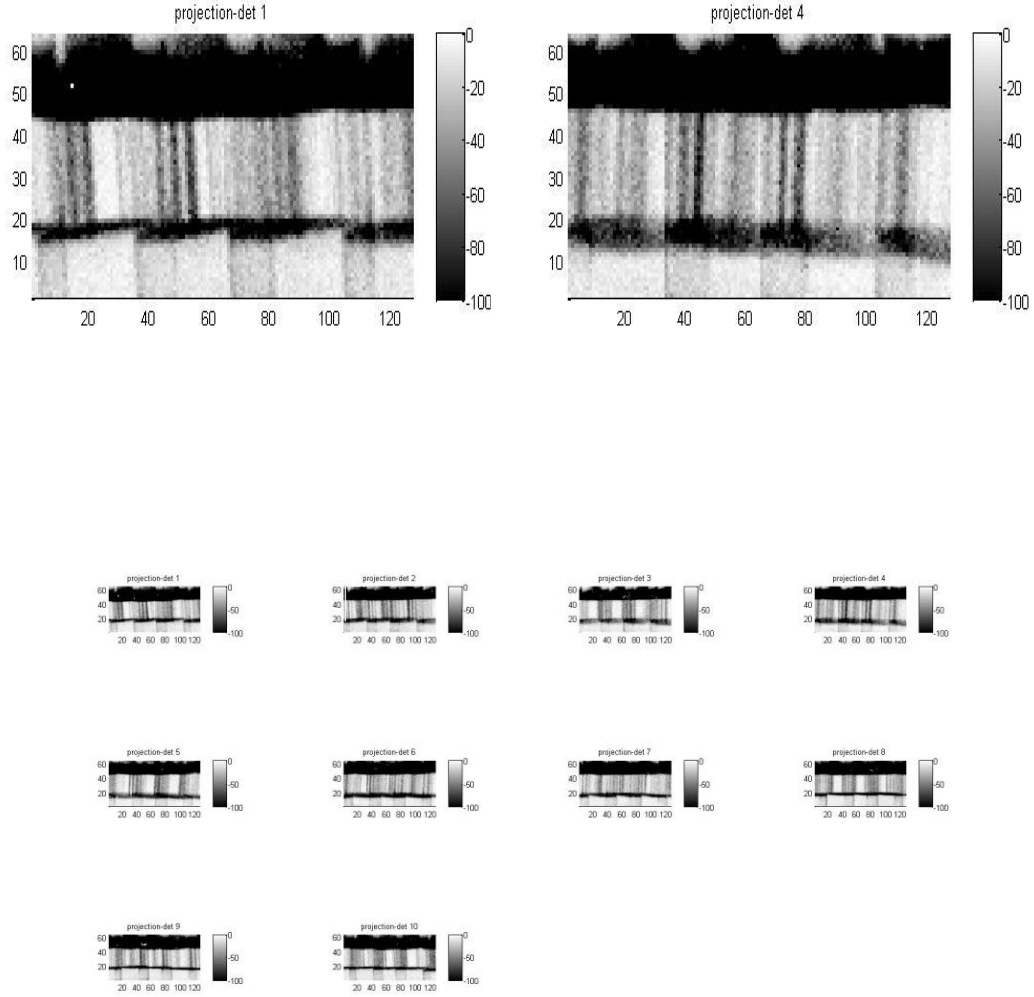

Fig. 4.14. The lab made Jascszak phantom projections in all ten detectors

Fig. 4.15 is the reconstructed phantom image. We can clearly see the 500μm features and the 350μm features can also be almost seen. In this experiment, the length of the phantom is longer than the FOV in axial direction. In order to get full projection data of the object, we linearly translated the phantom to another two positions and did corresponding data acquisition for 10 minutes at each position. The combined information is used to reconstruct the whole phantom image. More detail about this scheme will be discussed in the next section.

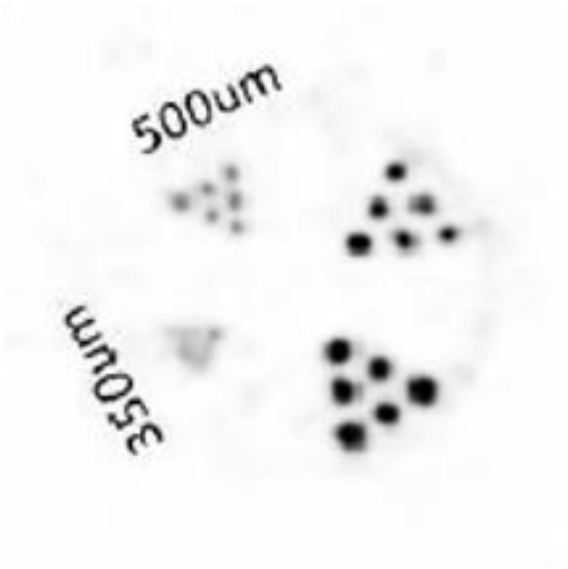

Fig. 4.15. The phantom image get from MRC-SPECT (the hot rods slice)

4.4.2 Imaging Study of Large Objects

The field of view of the current MRC-SPECT system is around Ø18mm×18mm, which is relatively small. For objects smaller than the field of view, the angular sampling for all the object is good enough and the corresponding image reconstruction process is straightforward. However, we will encounter problems when imaging object with larger size than the field of view, mainly due to the inefficient sampling at the object boundaries. The projection data obtained only with the object at the center provides insufficient information for high resolution imaging.

To overcome this problem, a multi-scanning procedure is implemented in this system for operating outside the MR scanner for ultrahigh resolution applications. Fig. 4.16 and 4.17 demonstrate a straightforward example of imaging objects with size larger than the field of view. The yellow area with red dash line boundary is the field of view, and the blue dash line represents the object boundary (Fig. 4.16). It is clear that the object is much larger than FOV and projection from single position must be not enough to provide sufficient information for image reconstruction. By taking projections after moving the object away from the center of FOV to different positions (Fig. 4.17), the combined data sets can be used to better reconstruct the object. In the Figure 4.17, the object is moved to four different positions followed by corresponding data acquisition.

Depending on the size of object size, different multi-scanning schemes can be designed to provide enough information for the large object scanning. We have carried out a large Derenzo phantom study to verify this scheme. In this study, 2mCi Tc-99m is injected to the phantom. The diameter of the Derenzo phantom is around 28mm and projections of phantom at multiple positions are acquired to do the image reconstruction. Projections are taken at a total of 16 different positions for two hours. Fig. 4.19 and Fig 4.20 demonstrates two different multi-scan scheme. The phantom image is reconstructed as shown in Fig. 4.18. There are obvious artifacts, most likely caused by severe truncation and insufficient angular sampling. But it is still very clear that the 16-position based projection data produces a much better image. With a more detailed and accurate system response function derivation, we are expecting better image reconstruction.

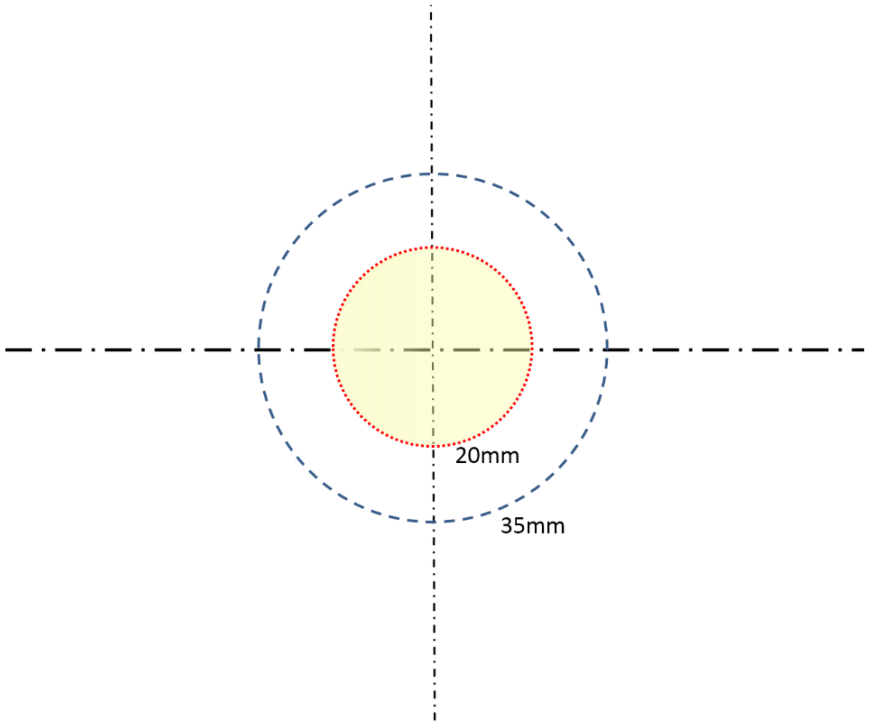

Fig. 4.16. Scheme to image object with size larger than FOV (single-scan)

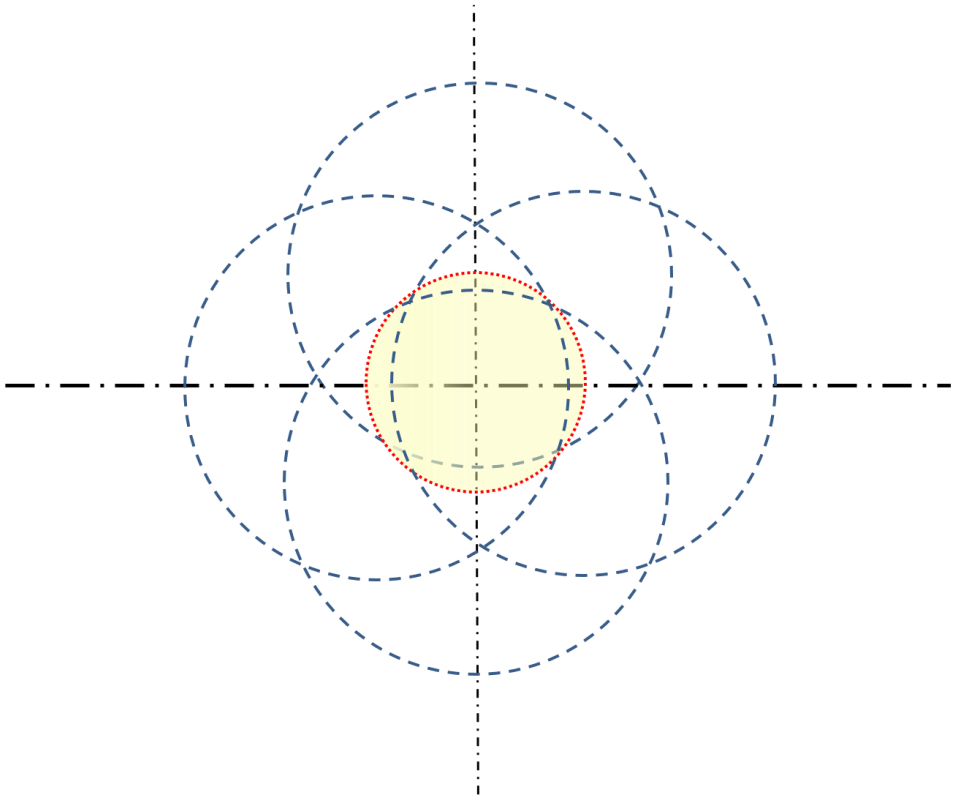

Fig. 4.17 Scheme to image object with size larger than FOV (multi-scan)

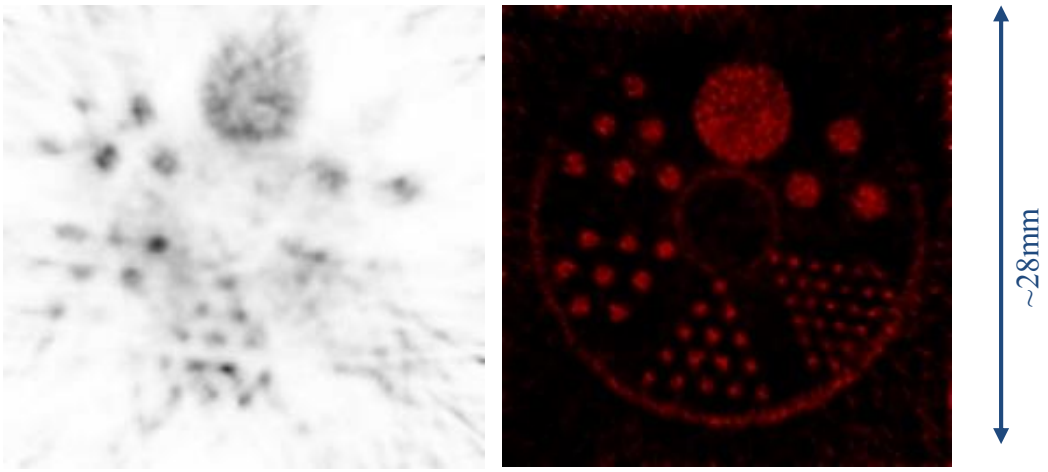

Fig. 4.18 Reconstructed “big” phantom image. Left: scan position at central four positions, (Fig. 4.18) Right: Projection at a total of 16 scan positions are used for reconstruction, (Fig. 4.19)

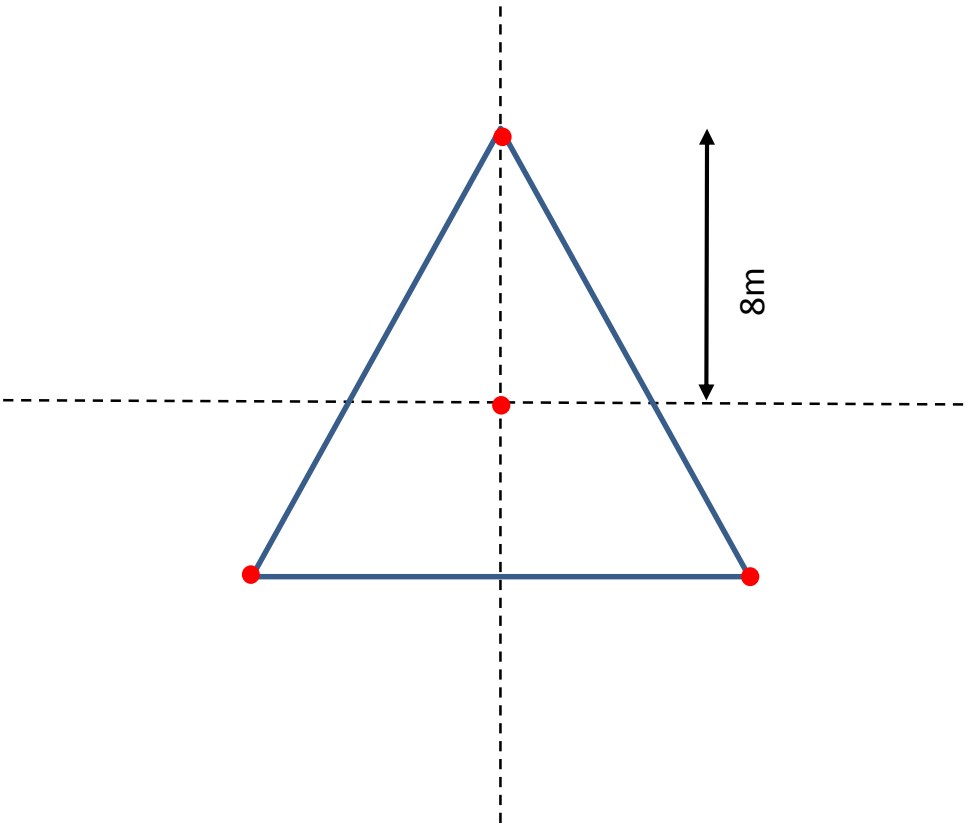

Fig. 4.19 “Big” phantom center 4 positions scan scheme

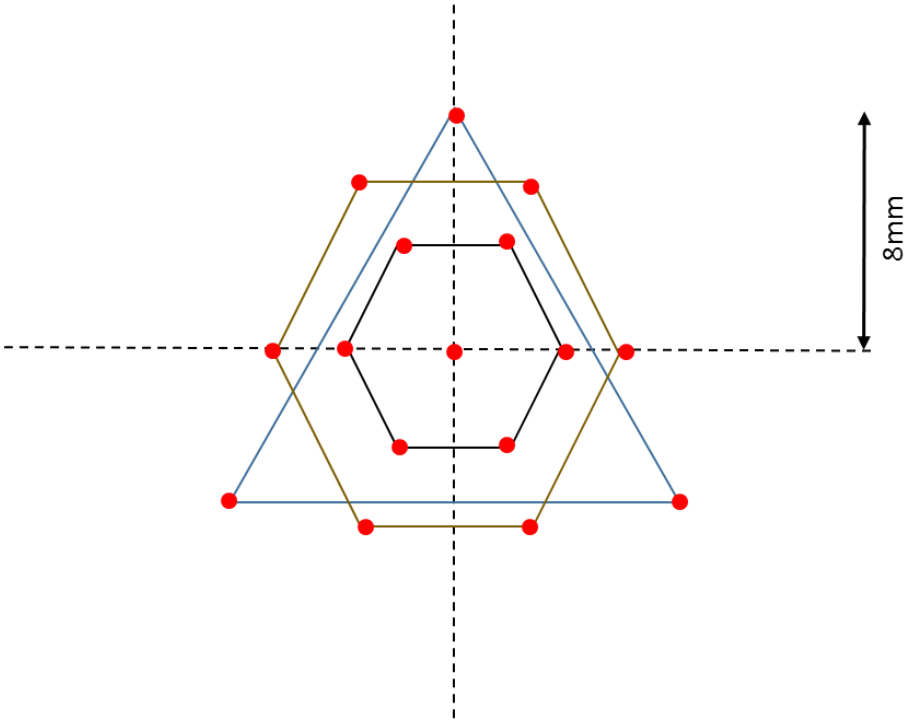

Fig. 4.20 “Big” phantom 16 positions scan scheme (side length of the two hexagons are 4mm and 6mm, respectively)

CHAPTER 5
Summary and Future Work

5.1 Summary of MRC-SPECT System Development

In this dissertation, the design, construction, and evaluation of a compact stationary MR-compatible SPECT (MRC-SPECT) system with the highest spatial resolution reported to date for MR/SPECT dual-modality imaging is discussed. The MRC-SPECT system is based on the second-generation energy-resolved photon-counting (ERPC) CdTe detectors and several key features associated with this system are summarized here. First, a total of ten ERPC detectors are assembled as a very compact ring, which provides an adequate angular sampling capability and relatively high detection efficiency. The detector module used in this system offers an intrinsic spatial resolution of 350μm and an excellent energy resolution of around 4keV at 140keV. Ten detectors are supported on a gantry made of high strength polyamide structure constructed using 3-D printing. This compact system can work as a "low-cost" desktop ultrahigh resolution SPECT system. It can also be directly operated inside an MR scanner. Second, a die-cast platinum pinhole insert and cast lead apertures are developed for this stationary SPECT system. Specific features are designed for this multi-pinhole SPECT system. Third, a detailed detector performance evaluation, accurate system geometrical calibration and corresponding image reconstruction methods for the MRC-SPECT system were investigated. A comprehensive charge collection model inside strong magnetic field was also adopted to produce high resolution SPECT image inside MR scanner. Preliminary phantom imaging studies were carried out to demonstrate the system performance. In the near future, this MRC-SPECT system will be used for a series of small animal imaging studies in University of Chicago Medical Center and Massachusetts General Hospital in Boston. Further improvement on both the hardware and software can be expected.

5.2 Future Work

5.2.1 System Hardware and Software Improvement

The MRC-SPECT is a fully running system at current stage. To further improve the system performance, proper hardware and software modifications can be executed.

- *Hardware*

For the hardware part, the most important modification and upgrade is the system cooling. The current cooling method is using compressed air to blow off the heat generated in the ASICs. There is no heat dispersal unit in the readout detector PCB. Since all the detectors are packed together within a compact and closed space, the generated heat is not easily circulated with the outside atmosphere. Relatively strong air pressure is required to efficiently take the heat generated away. In addition, the air circulating cooling scheme may potentially have a negative effect on imaging inside MR scanner. In the next version, a more efficient system cooling is necessary and a water cooling system is under consideration. This will help the MRC-SPECT system work in general scientific environment.

Another hardware upgrade can be done is the system-level electronics. All the ten detectors consume around 20A of current. The high current caused voltage drop in the power cable can't be ignored. A power regulation sub-system can be added to the current system level PCB.

The wire-bonding of the current version of detector has no protection. It is very delicate and any touch of the wire-bonding can cause severe damage to the detector. A custom-designed cover can be designed to genteelly protect the wire-bonding area.

- *Software*

There are two software associated parts can be modified in the future work. The first part is the development of a precise system response function. In section 4.3 we have applied an object space scan based experimental data-set to correct for the mathematically-calculated system response function. This scheme turns out to be useful and important, considering the complicated aperture geometry to be precisely modeled. A more detailed study of this derivation is needed for the future work on this system.

Second, a comprehensive and robust data processing package should be developed for this system. The current data processing routine is shown at the beginning of Chapter 4. Necessary packages can be applied to current data processing procedure to make the system more professional and user friendly. Ideally, the user should be able to get decent image result by only a few command buttons.

5.2.2 Other Imaging Applications Based on MRC-SPECT

In Chapter 3, it has been mentioned that the MRC-SPECT system accommodates with two different readout modes, RAM and live-data mode. The live-data mode can record frame by frame data at the rate of about 20fps. The accurate time stamp can be attached to each frame data. Since the frame-by-frame data contains the energy deposition in the individual pixels, the list mode data can be generated by post processing. One advantage of list-mode data is that the charge sharing events can be analyzed, which could potentially increase the system data recording efficiency. Another advantage lies on the timing information, which can be used for potential dynamic imaging applications and PET imaging studies.

In frame-by-frame mode, the acquired data will be used to generate projections with timing information, which will be used for 4D image reconstruction. The radioactive isotope distribution can be described as a temporospatial function f(x,y,z,t) instead of f(x,y,z). To achieve this application, the system needs to have a sufficiently fast data recording capability with timing information and relatively high sensitivity. In this application, online photon counting data processing will be applied to each frame data, based on which list-mode data will be produced. In the list-mode data, the interaction deposition energy, interaction position and interaction timing information will be recorded. Meanwhile, aperture pinholes of 750μm diameter will be used. The system sensitivity can go up to 0.2% in this case.

Besides potential dynamic imaging studies, different pinhole aperture designs can be used for various applications. For example, we can push the aperture pinholes closer to the object, which will result in a higher magnification and therefore better spatial resolution.

The system can work as a real “microscope” which enables the observation of small features.

In the future, series of small animal sequential and simultaneous MR-SPECT imaging studies will be carried out with collaborating facilities at the University of Chicago and the Harvard Medical School to further demonstrate the MRC-SPECT performance.

References

1. C. S. Levin, "Small animal PET and SPECT: Instrumentation, performance, and applications," *Medical Physics*, vol. 32, pp. 2096-2096, Jun 2005.
2. S. R. Cherry, "In vivo molecular and genomic imaging: new challenges for imaging physics," *Physics in Medicine and Biology*, vol. 49, pp. R13-R48, Feb 2004.
3. A. Rahmim, H. Zaidi, "PET versus SPECT: strengths, limitations and challenges" *Nucl Med Communication*, vol. 29, 2008
4. B. Vastenhouw, F. J. Beekman, "Submillimeter Total-Body Murine Imaging with U-spect-I", *Journal of Nucl Med*, vol. 48, no. 3, 2007.
5. F. D. Van Have, B. Vastenhouw, R.M. Ramakers, W. Branderhorst, J.O. Krah, C. Ji, S.G. Staelens, F.J. Beekman, "U-SPECT-II: An ultra-high-resolution device for molecular small-animal imaging" *Journal of Nucl Med*, vol. 50, pp. 599-605, 2009.
6. L. Zhou, K. Vunckx, J. Nuyts, "Multi-pinhole SPECT calibration: Influence of data noise and systematic orbit deviations" *IEEE Transactions on Medical Imaging*, vol. 27, no. 6, Oct 2011.
7. B. E. Hammer, N. L. Christensen, B. G. Heil," Use of a magnetic field to increase the spatial resolution of positron emission tomography", *Medical Physics*, vol. 21, no. 12, 1994.
8. R. R. Raylman, B. E. Hammer, N. L. Christensen, "Combined MRI-PET scanner: a Monte-Carlo evaluation of the improvements in PET resolution due to the effects of a static homogeneous magnetic field" *IEEE Transactions on Nuclear Science*, vol. 43, pp 1917-1920, 1994.
9. A. Wirrwar, H. Vosberg, H. Herzog, H. Halling, S. Weber, H-W. Muller-Gartner, "4.5 tesla magnetic filed reduces range of high-energy positrons – potential implications for positron emission tomography" *IEEE Transactions on Nuclear Science*, vol. 44, pp 184-189, 1997.
10. N. L. Christensen, B.E. Hammer, B.G. Heil, K. Fetterly, "Positron emission tomography within a magnetic field using photomultiplier tubes and lightguides" *Physics in Medicine and Biology*, vol. 40, no. 4, 1995

11. Qi, J., Leahy, R.M. “Iterative reconstruction techniques in emission computed tomography” *Physics in Medicine and Biology*, vol .51, no. 01, 2006
12. Reader, A.J., Ally, S., Bakatselos, F., Manavaki, R., Walledge, R.J., Jeavons, A.P., Julyan, P.J., Sha Zhao, Hastings, D.L., Zweit, J., "One-pass list-mode EM algorithm for high-resolution 3-D PET image reconstruction into large arrays," *IEEE Transactions on Nuclear Science*, vol.49, no.3, Jun 2002
13. Rafecas, M., Guido Boning, Pichler, B.J., Lorenz, E., Schwaiger, M., Ziegler, S.I., "Effect of noise in the probability matrix used for statistical reconstruction of PET data" *IEEE Transactions on Nuclear Science*, vol.51, no.1, Feb. 2004
14. Rahmim, A., Cheng, Ju-Chieh (Kevin), Sossi, V., “Improved noise propagation in statistical image reconstruction with resolution modeling" *Nuclear Science Symposium Conference Record, 2005 IEEE* , vol.5, no., Oct. 2005
15. Iwata, K., Greaves, R.G., Surko, C.M., “γ-ray spectra from positron annihilation on atoms and molecules” *Physical Review A - Atomic, Molecular, and Optical Physics*, vol. 55, no. 5, pp. 3586-3604, 1997
16. Shibuya, K., Yoshida, E., Nishikido, F., Suzuki, T., Tsuda, T., Inadama, N., Yamaya, T., Murayama, H., “Annihilation photon acollinearity in PET: Volunteer and phantom FDG studies” *Physics in Medicine and Biology,* vol. 52, no. 17, pp. 5249-5261, 2007
17. Sánchez-Crespo, A., Larsson, S.A., “The influence of photon depth of interaction and non-collinear spread of annihilation photons on PET image spatial resolution” *European Journal of Nuclear Medicine and Molecular Imaging*, vol. 33, no. 8, pp. 940-947, 2006
18. Levin C. S., Hoffman E. J., “Calculation of positron range and its effect on the fundamental limit of positron emission tomography system spatial resolution” *Physics in Medicine and Biology,* vol. 44, pp.781-799, 1999
19. Sánchez-Crespo, A., Andreo, P., Larsson, S.A., “Positron flight in human tissues and its influence on PET image spatial resolution” *European Journal of Nuclear Medicine and Molecular Imaging*, vol. 31, no. 1, pp. 44-51, 2004

20. Palmer, M.R., Zhu, X., Parker, J.A., "Modeling and simulation of positron range effects for high resolution PET imaging" *IEEE Transactions on Nuclear Science*, vol. 52, no. 5 I, pp. 1391-1395, 2005
21. Srivastava, S.C., Mease, R.C. "Progress in research on ligands, nuclides and techniques for labeling monoclonal antibodies" *Nuclear Medicine and Biology*, vol. 18, no. 6, 1991
22. Van Den Bossche, B., Van de Wiele, C. "Receptor imaging in oncology by means of nuclear medicine: Current status" *Journal of Clinical Oncology*, vol. 22, no. 17, 2004
23. Meikle, S.R., Kench, P., Kassiou, M., Banati, R.B. "Small animal SPECT and its place in the matrix of molecular imaging technologies" *Physics in Medicine and Biology*, vol. 50, no. 22, 2005
24. Wang, W.-T., Tsui, B.M.W., Lalush, D.S., Tocharoenchai, C., Frey, E.C., "Optimization of acquisition parameters for simultaneous ^{201}Tl and ^{99m}Tc dual-isotope myocardial imaging" *IEEE Transactions on Nuclear Science*, vol. 52, no. 5 I, pp. 1227-123, 2005
25. Du, Y., Frey, E.C., Wang, W.T., Tsui, B.M.W., "Optimization of Acquisition Energy Windows in Simultaneous ^{99m}Tc/^{123}I Brain SPECT" *IEEE Transactions on Nuclear Science*, vol. 50, no.5 II, pp. 1556-1561, 2003
26. De Jong, H., Beekman, F., Viergever, M., Van Rijk, P., "Simultaneous ^{99m}Tc/^{201}Tl dual-isotope SPET with Monte Carlo-based down-scatter correction" *European Journal of Nuclear Medicine*, vol. 29, no. 8, pp. 1063-1071, 2002
27. Song, X., Frey, E.C., Wang, W.T., Du, Y., Tsui, B.M.W., "Validation and evaluation of model-based crosstalk compensation method in simultaneous ^{99m}Tc stress and ^{201}Tl rest myocardial perfusion SPECT" *IEEE Transactions on Nuclear Science*, vol. 51, no. 1 I, pp. 72-79, 2004
28. Ouyang, J., El Fakhri, G., Moore, S.C., "Fast Monte Carlo based joint iterative reconstruction for simultaneous ^{99m}Tc/^{123}I SPECT imaging" *Medical Physics*, vol. 34, no. 8, pp. 3263-3272, 2007

29. H. H. Barrett, Lars R. Furenlid, Melanie Freed, Jacob Y., Hesterman, Matthew A. Kupinski, Eric Clarkson, and Meredith K. Whitaker, "Adaptive SPECT" *IEEE Transactions on Medical Imaging*, vol. 30, no. 10, June 2008
30. Del Guerra, Belcari, N., "State-of-the-art of PET, SPECT and CT for small animal imaging" *Nucl. Instr. Methods A*, vol. 569, pp. 301-305, 2006.
31. Moses, W.W. "Current trends in scintillator detectors and materials" *Nucl. Instr. Methods A*, vol. 487, pp. 123-128, 2002.
32. R. Accorsi, M. Autiero, L. Celentano, M. Chmeissani, R. Cozzolino, A.S. Curion, P. Frallicciardi, P. Laccetti, R.C. Lanza, A. Lauria, M. Maiorino, M. Marotta, G. Mettivier, M.C. Montesi, P. Riccio, G. Roberti, P. Russo, "MediSPECT: Single photon emission computed tomography system for small field of view small animal imaging based on a CdTe hybrid pixel detector" *Nucl. Instr. Methods A*, vol. 571, pp. 44-47, 2007.
33. Peterson, T.E., Kim, H., Crawford, M.J., Gershman, B.M., Hunter, W.C.J., Barber, H.B., Furenlid, L.R., Wilson, D.W., Woolfenden, J.M., Barrett, H.H., "SemiSPECT: A Small-animal Imaging System Based on Eight CdZnTe Pixel Detectors", *IEEE Nuclear Science Symposium and Medical Imaging Conference*, vol 3, pp 1844-1847, 2002
34. He Z. "Review of the Shockley–Ramo theorem and its application in semiconductor gamma-ray detectors" *Nucl. Instr. Methods A*, vol. 463, pp. 250-267, 2001.
35. C. Woody, D. Schlyer, P. Vaska, D. Tomasi, S. Solis-Najera, W. Rooney, J. F. Pratte, S. Junnarkar, S. Stoll, Z. Master, M. Purschke, S. J. Park, S. Southekal, A. Kriplani, S. Krishnamoorthy, S. Maramraju, P. O'Connor, and V. Radeka, "Preliminary studies of a simultaneous PET/MRI scanner based on the RatCAP small animal tomography" *Nucl. Instr. Methods A*, vol. 583, pp. 119-124, 2007.
36. R. Grazioso, N. Zhang, J. Corbeil, M. Schmand, R. Ladebeck, M. Vester, G. Schnur, W. Renz, and H. Fischer, "APD-based PET detector for simultaneous PET/MR imaging," *Nucl. Instr. Methods A*, vol. 569, pp. 301-305, 2006.
37. B. J. Pichler, M. S. Judenhofer, C. Catana, J. H. Walton, M. Kneilling, R. E. Nutt, S. B. Siegel, C. D. Claussen, and S. R. Cherry, "Performance test of an LSO-APD

detector in a 7-T MRI scanner for simultaneous PET/MRI" *Journal of Nucl Med*, vol. 47, pp. 639-647, 2006.

38. R. R. Raylman, S. Majewski, S. Lemieux, S. S. Velan, B. Kross, V. Popov, M. F. Smith, A. G. Weisenberger, and R. Wojcik, "Initial tests of a prototype MRI-compatible PET imager," *Nucl. Instr. Methods A*, vol. 569, pp. 306-309, 2006.
39. Mackewn, J.E. Keevil, S.F. Hallett, W.A. Halsted, P. Page, R.A. Kelly, M. Williams, S.C.R. Marsden, P.K,"An MR Compatible LSO-PET Scanner for Molecular Imaging Studies", *IEEE Nuclear Science Symp, and Medical Imaging Conf*, vol.5, pp.2986-2989, 2006.
40. D. P. McElroy, V. Saveliev, A. Reznik, and J. A. Rowlands, "Evaluation of silicon photomultipliers: A promising new detector for MR compatible PET," *Nucl. Instr. Methods A*, vol. 571, pp. 106-109, 2007.
41. Y. Shao, S. R. Cherry, K. Farahani, R. Slates, R. W. Silverman, K. Meadors, A. Bowery, S. Siegel, P. K. Marsden, and P. B. Garlick, "Development of a PET detector system compatible with MRI/NMR systems," *IEEE Trans. Nucl. Sci*, vol. 44, pp. 1167-1171, 1997.
42. N. Zhang, R. F. Grazioso, N. K. Doshi, and M. J. Schmand, "RF transformer coupled multiplexing circuits for APD PET detectors," *IEEE Trans.Nucl. Sci.*, vol. 53, pp. 2570-2577, 2006.
43. Wagenaar, D.J., Nalcioglu, O., Muftuler, L.T., Szawlowski, M., Kapusta, M., Pavlov, N., Meier, D., Maehlum, G., Patt, B.E. "Development of MRI-Compatible Nuclear Medicine Imaging Detectors", *Nuclear Science Symp, and Medical Imaging Conf*, vol.3, pp.1825-1828, 2006.
44. Y. Wang, D. Wagenaar, D. Meier, B. E. Patt, B. M. Tsui, "SPECT Image Reconstruction Aspects for a Pre-Clinical SPECT-MRI System", *IEEE Nuclear Science Symp. and Medical Imaging Conf*, 2007
45. D. Schlyer, P. Vaska, D. Tomasi, C. Woody, S. H. Maramraju, J.-F. Pratte, S. Southekal, S. Junnarkar, M. Purschke, S. Krishnamoorthy, A. Kriplani, S. Stoll, "A Simultaneous PET/MRI Scanner Based on the RatCAP",*IEEE Nuclear Science Symp. and Medical Imaging Conf*, 2007
46. E. Breton, P. Choquet, C. Goetz, J. Kintz, P. Erbs, R. Rooke, and A. Constantinesco,

"Dual SPECT/MR imaging in small animal," *Nucl. Instr. Methods A*, vol. 571, pp. 446-448, 2007.

47. C. Goetz, E. Breton, P. Choquet, V. Israel-Jost, and A. Constantinesco, "SPECT low-field MRI system for small-animal imaging," *Journal of Nucl. Med.*, vol. 49, pp. 88-93, 2008.
48. L. J. Meng, J. W. Tan, K., Spartiotis, T. Schulman, "Preliminary evaluation of a novel energy-resolved photon-counting gamma ray detector," *Nucl. Instr. Methods A*, 604(3): 548-554. 2009.
49. L. Cai, L. J. Meng, "Hybrid pixel-waveform CdTe/CZT detector for use in an ultrahigh resolution MRI compatible SPECT system" *Nucl. Instr. Methods A*, in press, 2012.
50. J. Fink, H. Kruger, P. Lodomez, and N. Wermes, "Characterization of charge collection in CdTe and CZT using the transient current technique," *Nucl. Instr. Methods A*, vol. 560, pp. 435-443, May 10 2006.
51. B. L. Doyle, G. Vizkelethy, and D. S. Walsh, "Ion beam induced charge collection (IBICC) studies of cadmium zinc telluride (CZT) radiation detectors," *Nucl. Instr. Methods B*, vol. 161, pp. 457-461, Mar 2000.
52. M. Benoit and L. A. Hamel, "Simulation of charge collection processes in semiconductor CdZnTe gamma-ray detectors," *Nucl. Instr. Methods A*, vol. 606, pp. 508-516, 2009.
53. A. E. Bolotnikov, W. R. Cook, F. A. Harrison, A. S. Wong, S. M. Schindler, and A. C. Eichelberger, "Charge loss between contacts of CdZnTe pixel detectors," Nuclear Instruments and Methods in Physics Research Section A: Accelerators, Spectrometers, Detectors and Associated Equipment, vol. 432, pp. 326-331, 1999.
54. E. Kalemci and J. L. Matteson, "Investigation of charge sharing among electrode strips for a CdZnTe detector," *Nucl. Instr. Methods A*, vol. 478, pp. 527-537, 2002.
55. A. Meuris, O. Limousin, and C. Blondel, "Charge sharing in CdTe pixilated detectors," *Nucl. Instr. Methods A*, vol. 610, pp. 294-297, 2009.
56. F. Zhang, Z. He, and D. Xu, "Analysis of detector response using 3-D position-sensitive CZT gamma-ray spectrometers," *IEEE Transactions on Nuclear Science*, vol. 51, pp. 3098-3104, Dec 2004.

57. W. Li, Z. He, G. F. Knoll, D. K. Wehe, and C. M. Stahle, "Spatial variation of energy resolution in 3-D position sensitive CZT gamma-ray spectrometers," *IEEE Transactions on Nuclear Science*, vol. 46, pp. 187-192, Jun 1999.
58. Z. He, G. F. Knoll, D. K. Wehe, and J. Miyamoto, "Position-sensitive single carrier CdZnTe detectors," *Nucl. Instr. Methods A*, vol. 388, pp. 180-185, Mar 21 1997.
59. D. Pennicard, R. Ballabriga, X. Llopart, M. Campbell, and H. Graafsma, "Simulations of charge summing and threshold dispersion effects in Medipix3," *Nucl. Instr. Methods A*, vol. 636, pp. 74-81, Apr 21 2011.
60. E. N. Gimenez, R. Ballabriga, M. Campbell, I. Horswell, X. Llopart, J. Marchal, K. J. S. Sawhney, N. Tartoni, and D. Turecek, "Characterization of Medipix3 With Synchrotron Radiation," *IEEE Transactions on Nuclear Science*, vol. 58, pp. 323-332, Feb 2011.
61. L. Tlustos, "Spectroscopic X-ray imaging with photon counting pixel detectors," *Nucl. Instr. Methods A*, vol. 623, pp. 823-828, Nov 11 2010.
62. W. Li, Z. He, G. F. Knoll, D. K. Wehe, and J. E. Berry, "Experimental results from an Imarad 8x8 pixellated CZT detector," *Nucl. Instr. Methods A*, vol. 458, pp. 518-526, Feb 1 2001.
63. F. Zhang, Z. He, D. Xu, G. F. Knoll, D. K. Wehe, and J. E. Berry, "Improved resolution for 3-d position sensitive CdZnTe spectrometers," *IEEE Transactions on Nuclear Science*, vol. 51, pp. 2427-2431, Oct 2004.
64. Y. Cui, M. Groza, G. W. Wright, U. N. Roy, A. Burger, L. Li, F. Lu, M. A. Black, and R. B. James, "Characterization of Cd1-xZnxTe crystals grown from a modified vertical Bridgman technique," *Journal of Electronic Materials*, vol. 35, pp. 1267-1274, Jun 2006.
65. L. J. Meng and Z. He, "Exploring the limiting timing resolution for large volume CZT detectors with waveform analysis," *Nucl. Instr. Methods A*, vol. 550, pp. 435-445, Sep 11 2005.
66. L. J. Meng and Z. He, "Estimate interaction timing in a large volume HgI2 detector using cathode pulse waveforms," *Nucl. Instr. Methods A*, vol. 545, pp. 234-251, Jun 11 2005.

67. J. W. Tan, L. Cai., L. J. Meng, "A prototype of the MRI compatible ultra-high resolution SPECT for in vivo mice brain imaging," *IEEE Nucl. Sci. Symp, and Med. Imag. Conf*, 2800-2805, 2009.
68. L. Cai, G. Fu, L. J. Meng, "A very-high resolution SPECT system based on the energy-resolved photon counting CdTe detectors", IEEE Nucl. Sci. Symp. and Med. Imaging Conf. Record, 2010
69. H. M. Hudson and R. S. Larkin, "Accelerated Image-Reconstruction Using Ordered Subsets of Projection Data," *IEEE Trans. Med. Imaging*, vol. 13, pp. 601-609, 1994.
70. J. W. Tan, L. Cai, L. J. Meng, "Experimental study of the response of CZT and CdTe detectors of various thicknesses in strong magnetic field", *Nucl. Instr. Methods A*, vol 652, no 1, pp. 153-157, 2011